REMOTE ACOUSTIC MEASUREMENT OF SUB-AQUEOUS GRAVITY-DRIVEN GRANULAR FLOWS

by

Jenna Hare

Submitted in partial fulfillment of the requirements
for the degree of Doctor of Philosophy

at

Dalhousie University
Halifax, Nova Scotia
April 2021

TABLE OF CONTENTS

LIST OF TABLES

LIST OF FIGURES

ABSTRACT

The central goal of this thesis is to characterize the velocity structure and concentration within gravity-driven sub-aqueous granular flows using high-resolution acoustic remote sensing technologies. The experiments were carried out with both glass beads and sand. The results have implications for studies of granular flows in general and of bedload dynamics in coastal ocean and fluvial environments in particular.

The geoacoustic properties of water-saturated sediments, which determine how the incident sound interacts with the granular medium, are investigated through measurements of sound speed and attenuation within the medium and the reflection coefficient at the sediment-water interface. The measurements are made in the scattering regime: i.e., $0.5 < ka < 1.2$, where k is the acoustic wave number in water and a is the median grain radius. The results, as well as those reported in the literature, confirm the $(ka)^4$ dependence of attenuation and negative dispersion predicted by the multiple scattering theory of *Schwartz and Plona* (1984). Scaling the data by a factor depending on porosity and grain density is shown to substantially reduce the spread among the available sound speed estimates. The measured roughness of the sediment-water interface is Gaussian and the measured reflection coefficients are consistent with the *Eckart* (1953) prediction for a rough surface with Gaussian-distributed roughness. A single-scattering model of reflection from the sediment-water interface is developed and found to reproduce the statistics and spatial variations in the reflected amplitude, including the decorrelation lengths associated with the speckle pattern in the reflected pressure field.

Sub-aqueous gravity-driven granular flows of O(1) cm thickness are investigated at mm-scale vertical resolution using a MHz frequency coherent Doppler sonar. The measurements are made for flow over both fixed roughness and erodible beds. Good agreement is obtained between the observed velocity profile and that predicted from an analytic low Reynolds number viscous fluid model. The model fits to the measured velocity profiles, combined with the *Bagnold* (1954) relation, yield estimates of effective viscosity and porosity within the moving layer that are respectively 400 (1100) times larger than that of water and 16% (7%) larger than the stationary glass beads (sand).

List of Abbreviations and Symbols Used

Abbreviation	Description
EDFM	effective density fluid model
EMA	effective medium approximation
BIMGS	modified gap stiffness model version of the Biot model (*Kimura*, 2011)
BIMGS+SP	modified gap stiffness model version of the Biot model combined with multiple scattering
BL	bottom loss
MFDop	wide-band pulse-coherent Doppler profiler
PDF	probability density distribution functions
PIV	particle imaging velocimetry
PTV	particle tracking velocimetry
PVC	polyvinyl chloride
rms	root-mean-square
SEM	scanning electron microscope
SNR	signal to noise ratio
SP	*Schwartz and Plona* (1984) EMA multiple scattering model
xdr	transducer

Notation	Description
O(·)	order of magnitude
$\overline{(\cdot)}$	average over N trials (Chap. 5)
$\tilde{(\cdot)}$	instrument coordinates (Chap. 5)

Roman symbol	Description	Units
a	grain radius	m
a_t	effective transducer radius	m

Roman symbol	Description	Units
A	amplitude of the detected return (Chaps. 2, 3, 5 and Appendix C)	V
A	rms value of $V_I(t)$ (Chap. 4) or $V_A(t)$ (Appendix D)	V
A_0	constant (Chap. 2 and Appendix D)	V
A_m	time-averaged $A(t)$ over times when the sediment was moving (Appendix D)	V
A_{ref}	backscatter amplitude for the aluminum plate (Chap. 4)	V
A_s	time-averaged $A(t)$ over times when the sediment was stationary (Appendix D)	V
Ba	Bagnold number (Eq. 5.4)	
c	phase speed in water-saturated sediments	m s^{-1}
c_0	reference velocity	m s^{-1}
c_g	group speed in water-saturated sediments	m s^{-1}
c_{gw}	sound speed in a glycerol-water mixture (Appendix C)	m s^{-1}
c^*_{LW}	long wavelength limit of sound speed (Eq. 2.6)	m s^{-1}
c_w	water sound speed	m s^{-1}
c_{wc}	the water sound speed based on the measured water temperature (Chap. 2)	m s^{-1}
C	ensemble pulse-pair correlations (Chap. 5)	
d	grain diameter	m
d_{50}	median grain diameter	m
D	transducer directivity	
f	frequency	Hz
F	scattering function (Sec. 2.8)	Hz
F	total force on the transducer face (Eq. 4.13 in Chap. 4)	kg m s^{-2}
g	gravitational acceleration	m s^{-2}
g	roughness parameter (Chap. 4 and Appendix B)	
G	soda lime glass beads (Table 2.3)	
h	sediment thickness (Chaps. 2, 3)	m
h_D	thickness of the moving layer estimated from the MF-Dop backscatter amplitude (Chap. 5)	m

Roman symbol	Description	Units
h_g	gate height	m
h_p	thickness of sediment above pinducer (Appendix D)	m
h_{sv}	thickness of the moving layer estimated from the side-view camera measurements (Chap. 5)	m
H	cylinder height (Chap. 2)	m
I	intensity	$\mathrm{kg}^2\ \mathrm{m}^{-2}\ \mathrm{s}^{-4}$
I	inertial number (Chap. 5)	
I_v	viscous number (Eq. 5.25)	
k	acoustic wave number in water	m^{-1}
k_{gw}	acoustic wave number in a glycerol-water mixture (Appendix C)	m^{-1}
K_*	effective bulk modulus	$\mathrm{kg\ m}^{-1}\ \mathrm{s}^{-2}$
K_s	bulk modulus of sediment grains	$\mathrm{kg\ m}^{-1}\ \mathrm{s}^{-2}$
K_w	bulk modulus of water	$\mathrm{kg\ m}^{-1}\ \mathrm{s}^{-2}$
L_η	surface correlation length (Chap. 4 and Appendix B)	m
m	fraction of glycerol in a glycerol-water mixture (Appendix C)	
m_s	measured mass of dry sediment (Chap. 2)	kg
m_w	water mass (Chap. 2)	kg
M_1	mass of sediment collected from the well (Chap. 2)	kg
M_2	mass of sediment collected in the tray (Chap. 2)	kg
n	porosity	
$\hat{n}$	adjusted porosity (Chap. 3)	
N	number of repeat trials (Chap. 5)	
N_c	number of cylinders used for each grain size and frequency (Chap. 2)	
N_p	number of particles in the transducer footprint (Chap. 4)	
N_s	noise level	V
N_t	number of repeat trials (Chap. 2)	
p	pressure	$\mathrm{kg\ m}^{-1}\ \mathrm{s}^{-2}$
p_*	reference pressure	$\mathrm{kg\ m}^{-1}\ \mathrm{s}^{-2}$

Roman symbol	Description	Units
p_b	reflected signal at the transducer (Eq. 4.12)	kg m^{-1} s^{-2}
p_i	incident pressure distribution	kg m^{-1} s^{-2}
$\hat{p}_j$	backscattered pressure from jth particle (Eq. 4.11)	kg m^{-1} s^{-2}
p_s	backscattered pressure from a surface	kg m^{-1} s^{-2}
P	percentage of runs that were retained Chap. 2)	
P	total complex pressure amplitude	kg m^{-1} s^{-2}
P_g	effective normal stress (Eq. 5.24)	kg m^{-1} s^{-2}
r	range (Chap. 2)	m
r	distance from the surface to the transducer (Chap. 4)	m
r_*	reference distance	m
r_0	range from the MFDop centre transducer to beam axes intersection point (Fig. 5.1b)	m
r_c	local radius of curvature of the surface (Eq. 4.8)	m
r_D	range to the fixed roughness bed from the MFDop centre transducer (Fig. 5.1)	m
r_V	range to the fixed roughness bed from the Vectrino centre transducer (Fig. 5.1)	m
R	coherent reflection coefficient at a rough boundary	
$\mathbf{R}$	coefficient of determination	
R_0	coherent reflection coefficient at a smooth boundary	
R_1	acoustic path from the transducer to the sediment-water interface (Chap. 2)	m
R_1	vertical distance from MFDop centre transducer to the sediment-water interface (Chap. 5)	m
R_2	acoustic path from the transducer to the cylinder edge (Chap. 2)	m
R_2	distance from the sidelobe to the sediment-water interface (Chap. 5)	m
R_c	start of farfield	m
R_c'	range to the last axial pressure maximum in the nearfield	m

Roman symbol	Description	Units
R_{ref}	reflection coefficient for the aluminum plate (Chap. 4)	V
Re	Reynolds number	
$S1$	219 μm quartz sand (Table 2.3)	
$S2$	406 μm quartz sand (Table 2.3)	
$S3$	497 μm quartz sand (Table 2.3)	
S_c	normalised scattering coefficient (Eq. 4.9)	
St	Stokes number (Eq. 5.27)	
t	time	s
u	x component of velocity	m s^{-1}
u_m	maximum velocity within the moving layer (Chap. 5)	m s^{-1}
V_{xx}	projections of the flow along the bisectors between two transducers	m s^{-1}
V	ensemble-averaged received signal (Chap. 4 and Appendix D)	V
V_b	bulk volume of a water-grain mixture	L
V_D	bulk volume estimated from MFDop measurements	L
V_I	interface return (Chap. 4)	V
V_s	volume of the sediment grains	L
V_T	volumetric flask volume (Chap. 2)	L
w	radial distance along the transducer face (Chap. 4)	m
w	z component of velocity	m s^{-1}
W	radius of the insonified area on the surface (Chap. 4)	m
W	chute width (Chap. 5)	m
x	horizontal coordinate	m
x_d	decorrelation length (Chap. 4)	m
z	vertical coordinate	m
z_0	distance from transducer to sediment-water interface (Chap. 4)	m
z_0	distance from transducer to fixed roughness bottom (Chap. 5)	m
z_∞	range to distant farfield (Chap. 4)	m

Roman symbol	Description	Units
z_m	height of velocity maximum (Chap. 5)	m
Z	acoustic impedance	kg m s^{-1}

Greek symbol	Description	Units
α	linear attenuation coefficient in water-saturated granular media	Np m^{-1}
α_c	chute angle	$\circ$
α_g	linear attenuation coefficient in a glycerol-water mixture (Appendix C)	Np m^{-1}
α_m	attenuation for moving sediment (Appendix D)	Np m^{-1}
α_s	measured attenuation for stationary sediment (Appendix D)	Np m^{-1}
α_w	linear attenuation coefficient in water	Np m^{-1}
β	angle between the beam axis and the target (Chap. 4)	$\circ$
β	rotation angle (Eq. 5.15 in Chap. 5)	$\circ$
β_V	rotation angle for Vectrino measurements (Chap. 5)	$\circ$
β_0	polar angle to the half-power point	$\circ$
β_e	polar angle for which $D^2 = e^{-1}$	$\circ$
β_s	polar angle to the to the peak of the first sidelobe	$\circ$
γ	$= du/dz$, velocity shear rate (Chap. 5)	s^{-1}
Γ_B	Eq. 4.15 in Chap. 4	m^2
γ_B	Eq. 4.17 in Chap. 4	
δh	sediment thickness difference (Chap. 3)	m
$\delta h'$	sediment thickness difference based on the measured ring height differences (Chap. 3)	m
δt	time difference between the returns from the sediment-water interface and the surface of the Delrin disk (Chap. 2)	s
δt	travel time difference (Chap. 3)	s
δz_p	height of the pinducer above the chute bottom (Appendix D)	m
Δz	particle vertical displacement (Chap. 4)	m

Greek symbol	Description	Units
ζ	parameter (Eq. 5.18)	s m^{-2}
η	sediment-water interface	m
η_g	dynamic viscosity of glycerol (Appendix D)	kg m^{-1} s^{-1}
η_{sv}	sediment-water interface based on the side-view camera measurements (Chap. 5)	m
η_V	sediment-water interface based on the Vectrino measurements (Chap. 5 and Appendix D)	m
θ_0	-3 dB beam half-widths	$^\circ$
θ_0	bisector angle when $\theta_{13} = \theta_{23}$ (Chap. 5)	$^\circ$
θ_{13}	bisector angle between transducer 1 and the centre transducer (Fig. 5.1b)	$^\circ$
θ_{23}	bisector angle between transducer 2 and the centre transducer (Fig. 5.1b)	$^\circ$
θ_c	angle between R_1 and R_2 (Chap. 2)	$^\circ$
θ_s	first sidelobe angles	$^\circ$
λ	acoustic wavelength	m
λ	linear grain concentration (Chap. 5)	
Λ	integral length scale	m
μ_e	effective viscosity (Chap. 5)	kg m^{-1} s^{-1}
μ_I	friction coefficient (Chap. 5)	
μ_r	$= \mu_e/\mu_w$, relative viscosity (Chap. 5)	
μ_w	dynamic viscosity of water (Chap. 5)	kg m^{-1} s^{-1}
ξ	tortuosity (Chap. 2)	
ρ	density of water-saturated granular material	kg m^{-3}
ρ_g	density of a glycerol-water mixture (Appendix C)	kg m^{-3}
ρ_*	effective bulk density	kg m^{-3}
$\hat{\rho}$	$= \rho - \rho_w$ (Chap. 5)	kg m^{-3}
ρ_s	grain density	kg m^{-3}
ρ_w	water density	kg m^{-3}
σ_j	backscatter cross-section for the jth particle	m^2
σ_η	root-mean-square bed elevation	m

Greek symbol	Description	Units
τ	shear stress in the x-direction (Chap. 5)	kg m^{-1} s^{-2}
τ_g	grain shear stress in the x-direction (Eq. 5.6 Chap. 5)	kg m^{-1} s^{-2}
τ_p	pulse length	s
ϕ	volume concentration	
ϕ_0	maximum possible static concentration	
ϕ_j	phase difference between the ray path to particle j (Chaps. 4 and 5)	
Ψ	$= \sqrt{n\rho_*/\rho_w}$, scaling parameter	
ω	angular frequency	s^{-1}

ACKNOWLEDGEMENTS

This PhD has been quite a journey filled with many twists and turns, not unlike the quests undertaken by any true hero. Much like a hero's quest, the goal is not just to make it to the end of the story, but to experience and learn from the journey itself. I did not complete this quest alone as I had many people supporting me. And so being at the end of this story, I wish to thank the people who have helped me along the way.

In any quest, there is always a wise guide to advise our hero. In my case, this is my supervisor, Dr. Alex Hay. And so first and foremost, I wish to thank Alex for his support and guidance throughout this journey. Without him this research would not have been possible. We went down many rabbit holes chasing down answers for "completeness" and/or because it was "good for the soul" and yet we always came out the other side with new insights. His dedication to excellence and thoroughness in finding solutions have helped shape me into the scientist I am today.

I am thankful for the support from my committee members (Dr. Anthony Bowen, Dr. David Barclay and Dr. Stephanie Kienast). Their suggestions and questions throughout this journey helped us come back to the main path when we detoured too far. Thanks to Dr. Len Zedel for many fruitful discussions, whether it be at conferences or while on breaks during fieldwork. In addition, I am thankful to Richard Cheel, whose laboratory assistance in designing and running experiments as well as coding-related and data-analysis discussions have been invaluable. I am grateful for Lori Lawton's help for all administrative matters and for the support provided by Dr. Markus Kienast as graduate coordinator. Thanks to Jackie Hurst and Daniel Morrison as well.

I greatly appreciate the support and assistance I have received from all members of the Hay Lab, both past and present. Their insights during lab meetings and suggestions for presentations were all greatly appreciated. In particular, thanks to Dr. Justine McMillan and Dr. Maricarmen Guerra Paris for their friendship, support and office talks which helped keep me sane during this journey. Thanks to Dr. Tristan Guest, Dr. Anneke Ten Doeschate and Dr. Greg Wilson for many useful science-related discussions.

Knowing that many others were undertaking similar journeys helped me stay on track with mine. So thanks to all DOSA members, past and present, who made my graduate

school experience enjoyable and rewarding. Our many social events (especially our epic annual Halloween parties) and multiple Seadogs intramural teams reminded this hero that it was important to take breaks when on a long quest. In particular, thanks to Emmanuelle Cook for being an amazing office-mate and to Meghan Troup, Dr. Erin Black, Krysten Rutherford, Myriam Lacharité and Katie Frame for their friendship and office chats.

And finally, I could not have completed this journey without the love and support of my friends and family. Thanks to my best friend and training partner, Abby Kennedy, for hours of training, discussions dissecting our training, movie nights and many late night-chats. Thanks to my coaches and training partners at Bushido-Kai, who helped me stay sane by encouraging me to hone my martial arts skills. Thanks to Raphaëlle Groulx-Julien, Mariève Bouchard Marmen, Audrey Poulin and Marie-Eve Myrand-Lapierre for their many years of friendship. Thanks to my family, in particular my amazing aunts, for their unconditional love, support and encouragement. A very special thank you to my mom, Suha, for being my number one fan and always believing in me. Thanks to my partner Jeremy, who somehow always knew exactly what I needed when I needed it, whether it was loving words of encouragement, listening to me ramble about science or simply a hug.

And a final thank you to Moca, my furry companion for the last 17 years, who will only cuddle with me when she feels like it but also somehow knows to be there when I really need it.

CHAPTER 1

INTRODUCTION

1.1 Motivation

Granular materials are of interest in many disparate fields including physics, geophysics, food processing, pharmaceuticals, mining, agriculture and construction. The flow of granular materials is a complex, non-linear process, in which it can behave like a solid, liquid or a gas in response to an applied stress (*Jaeger et al.*, 1996). There is still no accepted set of governing equations that fully describe this complex behaviour (*Forterre and Pouliquen*, 2008). In addition, the physics regulating granular flows depend on many factors including particle shape and size as well as the relative density of the particle to the interstitial fluid. For water-saturated granular flows, questions remain including how viscosity depends on particle concentration.

In the ocean, the transport of sub-aqueous granular materials impacts bed morphology, benthic ecology, pollutant transport and coastal infrastructure. Of particular interest is bedload, the part of the total sediment load that travels in mostly continuous contact with the bed. Bedload depends on the nearbed flow and turbulence as well as the seafloor morphology and sediment properties. The feedbacks between these components are still poorly understood, limiting our understanding of bedload processes and ability to reliably predict bedload transport (*Ancey*, 2020a,b).

Bedload transport is difficult to measure, especially in energetic field conditions. Sediment traps have been used; however, they do not give any information on short time and small spatial scales or on the internal structure of concentration and velocity in the bedload layer. Acoustic remote-sensing technologies operating at MHz frequencies and μs pulse lengths could in principle provide the mm-scale range resolution required to resolve

the bedload layer. These systems have been used to obtain nearbed flow measurements in sheet flow conditions, over ripples and dunes, both in the laboratory and in the field. While the results from recent studies using these systems have been promising, the vertical structure of velocity and concentration in the bedload layer remains an open question.

While this thesis is not about bedload, it does address a closely related topic: the flow of a thin, sub-aqueous layer of granular material down an incline. Similar to making bedload measurements, measuring the velocity structure within granular flows at high spatial and temporal resolution is challenging. In the laboratory, velocity profiles within dense granular flows have been obtained using particle tracking velocimetry and particle imaging velocimetry. However, these types of side-on video-imaging techniques can be affected by friction from tank side-walls. Side-on optical measurements without side-wall effects have been made using special fluids and particles with matched refractive indices (see references cited in Chap. 5). This method is not applicable to natural sand in water. Acoustic remote-sensing technologies have been used to make nearbed flow measurements away from tank side-walls in the laboratory. Promising results have been obtained in sheet flow conditions using lightweight plastic particles and over bedforms (see Chap. 5 for a review of the relevant literature). Prior to this thesis and to my knowledge, vertical profiles of velocity within sub-aqueous gravity-driven granular flows using natural sand – or sediment with densities similar to that of sand – have not been obtained using these types of acoustic systems.

When choosing the transmit frequency for making acoustic measurements within a dense mixture of water and solid particles, there is a trade-off between range resolution and the depth of penetration of the acoustic signal. Thus, the attenuation of sound and its dependence on frequency, grain size and porosity also need to be known. Due to the lack of measurements over the full range of volume concentrations for sand-sized particles at MHz frequencies (the relevant literature is reviewed in Chap. 2), there are questions as to which theory best describes the dependence of attenuation and sound speed on acoustic frequency, particle size and type, and porosity.

To fully investigate the acoustic returns from within granular flows, reflection and transmission coefficients at the sediment-water interface are needed since they represent a measure of the acoustic energy that gets transmitted from the water into the sediment. The reflection of high-frequency sound at the sediment-water interface not only depends on

the sound speed within, and the bulk density of, the water-saturated sediment, but also on the roughness of the interface. Both the sound speed and interface roughness depend on the transmit frequency, grain size and sediment porosity. Thus, the reflection coefficient could potentially provide information on porosity at, and immediately below, the sediment-water interface. Few measurements of the reflection coefficient for sand-sized granular materials at normal incidence and at MHz frequencies exist in the literature (see Chap. 4).

1.2 Research Objectives

The overall goal of this thesis is to investigate the use of broadband acoustic Doppler to remotely measure the thickness of, and velocity profiles within, a high concentration moving layer of water-saturated granular material. In order to address this goal, my thesis will focus on the following objectives:

1. Measure attenuation (Chap. 2), group speed (Chap. 2) and phase speed (Chap. 3) in water-saturated granular materials at MHz frequencies as a function of frequency and grain size.

2. Investigate the dependence of group speed (Chap. 2), phase speed (Chap. 3) and attenuation (Appendix D) on particle concentration.

3. Measure the size/frequency-dependence of the reflection coefficient from the sediment-water interface for stationary sediment (Chap. 4)

4. Measure velocity profiles within, and the thickness of, a gravity-driven sub-aqueous granular flow over fixed roughness (Chap. 5) and erodible (Appendix C) beds.

1.3 Approach and Impact

In this thesis, laboratory data on sound attenuation, phase speed and group speed within water-saturated sediments, as well as the reflection coefficient at the sediment-water interface, are presented and compared to predictions from multiple scattering theory. This research increases our understanding of sound propagation and attenuation in, and reflection from, water-saturated granular media at high concentrations.

A laboratory apparatus is developed to study gravity-driven granular flows on an inclined plane. Using a wideband pulse-coherent acoustic instrument, remote measurements of the velocity structure within the moving layer are obtained. The results test our understanding of the grain-scale physics that regulate the mean velocities within gravity-driven granular flows.

While this thesis focuses on gravity-driven granular flows, the results and conclusions presented herein have applications to other fields, in particular bedload transport in aquatic environments. The thesis provides insight into the grain size and frequency dependence of sound propagation in dense granular media as well as the limits of using remote-sensing acoustic techniques on measuring granular flows. These components were measured in a controlled laboratory setting and, thus, pave the way for measuring bedload transport in the field using these types of acoustic technologies.

1.4 Thesis Organisation

The thesis is organised as follows. Chap. 2 presents measurements of attenuation and group speed in water-saturated granular media using a monostatic geometry at frequencies from 1.2 to 2.0 MHz for natural sand and glass beads. The measurements are compared to previously reported estimates using transmission geometries. In Chap. 3, phase speed measurements in the same granular materials are presented and compared to previously reported measurements as well as to the negative dispersion predicted by *Schwartz and Plona* (1984)'s multiple scattering theory. In Chap. 4, measurements of the reflection coefficient of the sediment-water interface at MHz frequencies are compared to previously reported estimates and to *Eckart* (1953)'s prediction for a rough surface with Gaussian-distributed surface elevations. In addition, a single-scattering model of reflection from the surface of the granular medium at wavelengths comparable to the grain diameter is developed. The probability distribution of the reflected amplitude and the decorrelation length predicted by the model are compared to the measurements.

In Chap. 5, acoustic measurements of the velocity structure within a sub-aqueous granular flow down a slope on a fixed roughness bottom are compared to estimates from a video imaging system and to predictions from a low Reynolds number viscous flow model. The effective viscosity and porosity within the moving layer are estimated from

a fit to the velocity profile using *Bagnold* (1954)'s semi-empirical relationship. In Appendix A, velocity profiles within a saline density current obtained using two Doppler profilers operating at different frequencies are presented. The roughness of the sediment-water interface of a moving layer is estimated in Appendix B. In Appendix C, velocity profiles within a moving layer over an erodible bed of like material are presented. The dependence of sound attenuation on particle concentration is investigated in Appendix D with estimates of the attenuation in a moving layer of glass beads over an erodible bed of like material also given. In Chap. 6, key findings are summarised with implications and future work being discussed.

Chaps. 2, 3 and 4 have been published in *The Journal of Acoustical Society of America*. The content of these chapters has not been altered from their published versions. Chap. 5 has been submitted to the *The Journal of Geophysical Research: Earth Surface* and the contents of the appendices are being prepared for publication. As lead author on these papers, I was responsible for performing the laboratory experiments, data analysis, the interpretation of the results, preparing the figures and writing the manuscripts. My co-author, Alex Hay, provided guidance on both the research and the editing of the manuscripts. Laboratory assistance was provided by Richard Cheel (laboratory manager). The experimental designs stemmed from discussions among Alex Hay, Richard Cheel and myself.

CHAPTER 2

ATTENUATION AND GROUP SPEED IN WATER-SATURATED GRANULAR MATERIALS AT MHZ FREQUENCIES

This chapter was first published in *The Journal of Acoustical Society of America*[1]

Abstract

Attenuation and group speed measurements are reported for water-saturated granular materials (natural sand and glass beads) at frequencies of 1.0 to 1.8 MHz. Median grain diameters were 219 to 497 μm, corresponding to $kd \gtrsim 1$: i.e., the scattering regime. The measurements were made for different thicknesses of sediment resting on a reflective surface using a monostatic geometry. The attenuation estimates compare well with previously reported experimental results and to the predictions of multiple scattering theory, confirming in particular the tendency toward f^4 dependence for $kd \gtrsim 1$. Group speed estimates exhibit the negative dispersion predicted by theory and are comparable in magnitude to previously reported measurements made using transmission geometries. It is found that the available data exhibit a O(10)% spread among the sound speed measurements at a given kd value, and that this spread is reduced to 2.2% when the data are scaled by a factor dependent on porosity and grain density, and that essentially all of the reduction can be attributed to differences in porosity.

[1]Reproduced from **Hare, J.**, and A. E. Hay, Attenuation and group speed in water-saturated granular materials at MHz frequencies, *J. Acoust. Soc. Am.*, 143, 2744–2755, 2018, with permission of AIP Publishing.

2.1 Introduction

Over the past two decades, there has been increasing interest in the physics of granular materials (*Jaeger et al*., 1996; *Shinbrot and Muzzio*, 2000; *Mehta et al*., 2009). In response to an applied stress, a granular material can behave like a solid, liquid or gas. The transitions between these states are not always well defined, nor well understood (*Jaeger et al*., 1996), and there is still no accepted set of governing equations that fully describe this complex behaviour (*Forterre and Pouliquen*, 2008). Understanding the physics of these materials at the grain scale is important across a wide range of disparate fields including sediment transport (*Nielsen*, 1992), snow avalanches (*Mehta et al*., 2009) and size segregation in granular mixtures (*Shinbrot and Muzzio*, 2000).

This chapter is concerned with the potential applications of acoustics for studying water-immersed granular flows. An important question is the thickness of, and vertical profile of particle velocity in, a moving layer of granular material. Laboratory measurements of the flowing layer thicknesses have been obtained using particle tracking velocimetry (PTV) (*Jain et al*., 2004) and video (*Pignatel et al*., 2012) in a rotating drum and using particle image velocimetry (PIV) in a tiltable Hele-Shaw cell (*Doppler et al*., 2007). In the field, *Lanckriet et al*. (2013) obtained sediment concentration profiles in sheet flows using a multi-element conductivity probe.

In principle, active acoustic technologies enable investigation of subaqueous granular flow processes remotely, i.e. without disturbing the flow itself, potentially providing measurements of both velocity and concentration profiles through the mobile layer. In the laboratory, these measurements can be made away from tank sidewalls, an improvement over side-on video-imaging techniques. In the field, the instrumentation can be made sufficiently robust to be used in energetic forcing conditions. High resolution coherent Doppler profiling systems have been developed for the study of sediment dynamics in turbulent flows (*Hurther and Lemmin*, 2008; *Hay et al*., 2012), utilizing the bandwidth of acoustic transducers at MHz frequencies to obtain both sub-cm range resolution and to exploit the frequency-dependence of the backscatter amplitude to estimate sediment concentration. Promising results have been obtained with these systems in studies of shear-driven sediment transport in the laboratory (*Hurther and Thorne*, 2011; *Naqshband et al*., 2014; *Revil-Baudard et al*., 2015; *Wilson and Hay*, 2016), and in the field (*Hay*

et al., 2014). However, the algorithms that have been implemented for inverting backscatter amplitude to sediment concentration assume single-scattering, and so are limited to sediment concentrations less than a few percent by volume (e.g. *Hurther et al*. (2011); *Thorne et al*. (2011); *Wilson and Hay* (2015)). These single-scatterer approximations are expected to be inaccurate at 10 to 70% sediment concentrations typical of many gravity-driven granular flows (*Houssais et al*., 2015) and shear-driven plug flows (*Flores and Sleath*, 1998).

The present investigation is motivated by a question closely related to estimating the concentration of dense aqueous suspensions of solid particles from acoustic backscatter amplitude. What is the size/frequency-dependence of the attenuation of MHz frequency sound in water-saturated granular media? The particular granular media of interest are natural mineral grains in the sand-size range and spherical grains with material properties similar to natural sand. For frequencies of 1 to 2 MHz, and particle diameters of O(0.1) to O(1) mm (i.e. the sand size range), the wavenumber-diameter product ranges from O(1) to O(10). As will be seen, the available data for attenuation in this range are inconsistent. Most of the previous measurements were made using a pair of buried transducers. One previous study, that by *Nolle et al*. (1963), used a monostatic geometry, and the apparent inconsistency hinges on their results. To resolve the discrepancy, new measurements of backscatter amplitude and two-way travel time were made to determine the dependence of attenuation and sound speed on acoustic frequency and particle size in water-saturated granular materials at MHz frequencies. Because of the intended application - i.e. remote measurement of granular flow properties - a monostatic geometry was implemented for the new measurements. The materials used are sand and glass beads, with similar grain densities and sound speeds, but very different surface roughness. The results are compared to values previously reported in the literature, and to the predictions of the *Schwartz and Plona* (1984) multiple scattering theory.

This chapter is organized as follows. Previous attenuation and group speed measurements are presented in Sec. 2.2. The experimental set-up and analysis methods are described in Sec. 2.3. The results are presented in Sec. 2.4 and discussed in Sec. 2.5. Conclusions are given in Sec. 2.6.

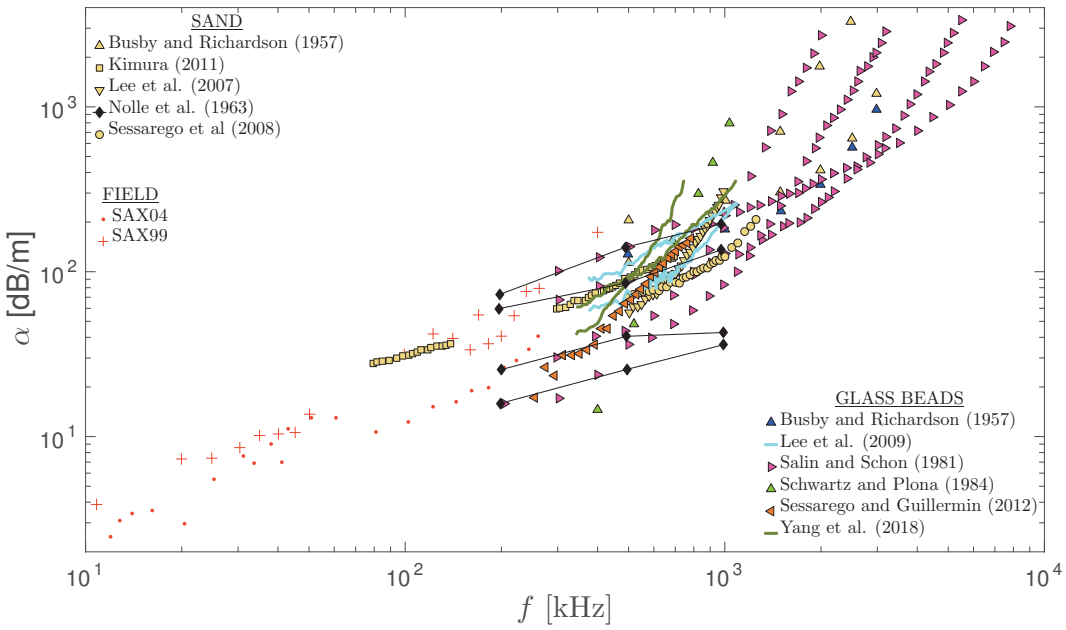

Figure 2.1: Attenuation data from the literature for water-saturated granular materials (sand and glass beads). Laboratory measurements for sand are indicated in yellow, for glass beads in different colours. Field measurements for sand are indicated in red. Data below 10 kHz are not shown.

2.2 Previous Measurements

2.2.1 Attenuation

Attenuation measurements reported in the literature for water-saturated granular materials (sand and glass beads) are plotted in Fig. 2.1. These data were extracted from the relevant figures in the original publications. The one exception is *Nolle et al*. (1963), which, as explained later, were taken from *Chotiros and Isakson* (2004). Results are included from two field experiments, SAX99 and SAX04 (*Williams et al*., 2002; *Hefner et al*., 2009). With the exception of the *Nolle et al*. (1963) results, all of the laboratory measurements were made using a transmit and receive transducer pair buried in the sediment at different separation distances. *Nolle et al*. (1963) used a single transducer method, determining the attenuation from the return signal travelling through different thicknesses of sand resting on a reflective surface. The field data were obtained using different methods, including buried pairs of transducers or an array of buried hydrophones in conjunction with a source transducer in the overlying water.

In Fig. 2.2, these same data (converted to Np/m) are plotted as a function of kd, where

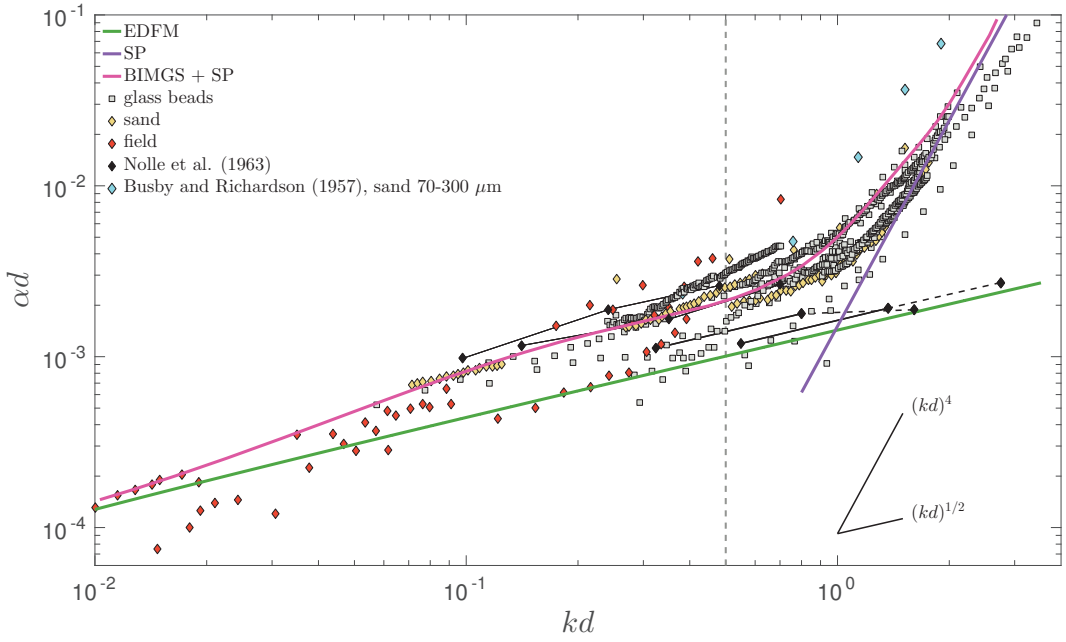

Figure 2.2: Attenuation data from the literature as in Fig. 2.1, but converted to Np/m, non-dimensionalized with particle diameter d, and plotted vs kd rather than frequency. Laboratory measurements for sand are indicated by yellow diamonds, for glass beads by grey squares and for field measurements by red diamonds. The solid lines are the results from different models: EDFM, the Effective Density Fluid Model (*Williams et al.*, 2002); SP, multiple scattering model given by Eq. 2.1 (*Schwartz and Plona*, 1984); BIMGS+SP, Modified Gap Stiffness Model version of the Biot model for 215 μm sand combined with SP (*Kimura*, 2011). Two kd power-law dependencies are indicated. Data below $kd = 0.01$ are not shown.

k is the wavenumber in water and d is the grain diameter. The literature values were converted from frequency space to wavenumber using the reported water sound speed when indicated and 1480 m/s when not. Comparing Figs. 2.1 and 2.2, it is clear that non-dimensionalizing by the particle diameter leads to an overall reduction in spread, particularly for $kd > 0.1$.

Also shown in Fig. 2.2 are the predicted curves from three models: (1) the Effective Density Fluid Model, EDFM, computed using parameters given by *Williams et al*. (2002); (2) the *Schwartz and Plona* (1984) effective medium approximation (EMA) multiple scattering model, SP; and (3) the Modified Gap Stiffness Model version of the Biot model combined with multiple scattering, BIMGS+SP, from *Kimura* (2011, Fig. 11b, 215 μm sand).

For $0.1 < kd \lesssim 0.5$, αd varies between $(kd)^{1/2}$ and $(kd)^1$. In this region, attenuation is dominated by viscous losses and both the EDFM and BIMGS+SP models have roughly the same kd dependence. *Nolle et al*. (1963) found $\alpha d = Ck^{1/2}$, where C is a constant: i.e. different from the $(kd)^{1/2}$ dependence.

For values of $kd \gtrsim 0.5$, most of the data in Fig. 2.2 exhibit an upturn tending toward $(kd)^4$, consistent with the purple curve given by

$$\alpha d = 1.31 \times 10^{-2} (kd)^4 \tag{2.1}$$

which is *Kimura*'s best-fit regression to *Schwartz and Plona*'s multiple scattering predictions for 545 μm diameter glass beads. The values obtained by *Busby and Richardson* (1957) for 70-300 μm diameter sand are roughly a factor of two higher than the other results, likely due to the wide range of grain sizes in their sample. The *Chotiros and Isakson* (2004) values from *Nolle et al*. (1963) do not exhibit a tendency toward the $(kd)^4$ dependence at high kd. This anomaly is discussed further in Sec. 2.5.

2.2.2 Phase speed

The phase speed measurements reported in the literature are plotted in Fig. 2.3. *Kimura* (2014)'s best-fit regression to the multiple scattering prediction for 545 μm glass beads from *Schwartz and Plona* (1984, Fig. 1) is:

$$\frac{c}{c_0} = 1 - 8.54 \times 10^{-3} (kd)^{2.45} \tag{2.2}$$

where c_0 is a reference velocity, equal to 1790 m/s for *Schwartz and Plona*'s data.

Both the theory and the experimental data exhibit negative dispersion at high kd. Phase speed values reported for glass beads are ∼80 m/s higher than those reported for similar-sized sand, which *Kimura* (2011) attributed to the difference in porosity of the two materials (sand: 0.42-0.44; glass beads: 0.37-0.38). At long wavelengths, both the data and the theory tend toward sound speed values between 1700 m/s and 1800 m/s. *Nolle et al.* (1963) similarly found that the sound speed in water-saturated sand was 1740 m/s, again using their single transducer method.

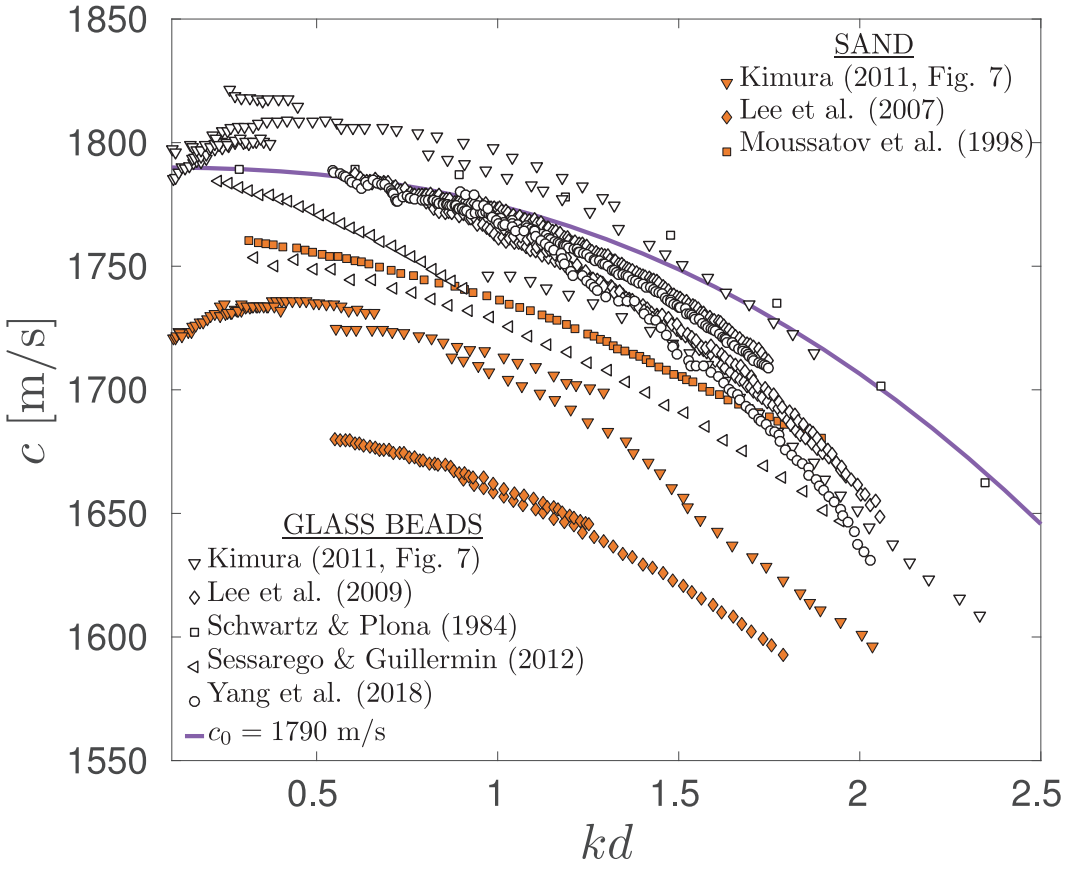

Figure 2.3: Phase speed for saturated water-particle mixtures: glass beads (white) and sand (orange). The solid purple line is *Kimura* (2014)'s best-fit regression to *Schwartz and Plona*'s multiple-scattering model result for 545 μm glass beads (Eq. 2.2). Values below $kd = 0.1$ are not shown.

2.3 Methods

2.3.1 Experimental apparatus

As previously indicated, a monostatic scattering geometry was implemented for the present experiments. A scale diagram of the experimental setup is shown in Fig. 2.4a. A circular transducer constructed from high efficiency piezo-composite material was mounted, facing downward, at the top of a 43 (width) x 90 (length) x 48 (height) cm rectangular glass-walled tank. The transducer was centered on a 9.03 cm diameter, 4.90 cm thick cylindrical Delrin disk resting on the bottom of the tank. Ten nested PVC cylinders of different heights surrounded the Delrin disk (Fig. 2.4b). The inner diameters of the cylinders ranged from 11.5 cm to 23.0 cm. The cylinder heights ranged from 5.29 cm to 7.10 cm, with a mean difference between nearest neighbours of 2.0 ± 0.1 mm. Sediment was poured into the cylinders from containers fully immersed in the water-filled tank. To obtain a flat sediment-water interface, the excess granular material was scraped off by carefully drawing a straight edge longer than the cylinder diameter across the cylinder end face. After the acoustic data was collected for that interface, the outermost cylinder was then removed and the process repeated until the smallest cylinder was reached. Nothing was done to compact the granular material.

Measurements of the backscatter waveform were obtained for each cylinder using a digital oscilloscope sampling at 125 MHz. The 4 μs transmit pulse and analog electronics were similar to those used with the Doppler profiler described in *Hay et al*. (2012). The frequencies used ranged from 1.0 to 1.8 MHz, separated by the 250 kHz equivalent bandwidth, and varied with grain size (see Table 2.1). For the larger grain sizes, the higher attenuation limited the choice of maximum usable frequency.

Using the transducer effective radius of $a_t = 0.011$ m (obtained from the best fit to the analytic prediction for a uniformly-sensitive circular piston transducer of the measured beam patterns at 1.4 to 2.0 MHz (*Wilson and Hay*, 2015)), the -3 dB beam half-widths θ_0 range from 1.1° to 2° and the first sidelobe angles θ_s from 3.5° to 6.3° (Table 2.2). In Fig. 2.4a, the vertical distance from the transducer to the sediment-water interface, R_1, as well as the distance to the cylinder edge, R_2, are indicated by the dashed lines. The angle θ_c between R_1 and R_2 ranged from 10° to 20° depending on the cylinder size. Since θ_c is much greater than θ_0 and θ_s, returns from the cylinder edge are not expected and were not observed.

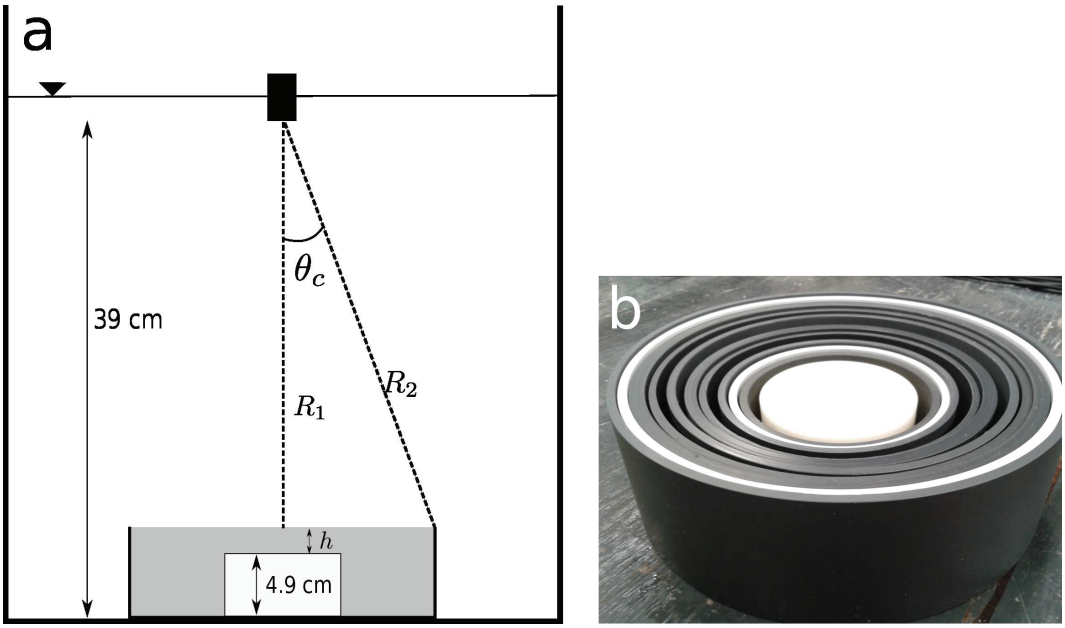

Figure 2.4: (a) Scale diagram of the experimental set-up (end view of the tank) illustrating the largest nested cylinder surrounding a cylindrical Delrin disk (white) on the bottom of a tank filled with water. The acoustic paths from the transducer to the sediment-water interface, R_1, and to the cylinder edge, R_2, are indicated by the dashed lines. (b) Photograph of the nested cylinders and Delrin disk.

Table 2.1: Number of cylinders, N_c, used for each grain size and frequency out of a possible total equal to 10 times the number of trials, N_t. Boiled samples are indicated by the subscript B. Unless indicated otherwise, the number of repeat trials $N_t = 3$ for each frequency.

f [MHz]	S1	$S1_B$	S2	$S2_B$	S3	G	G_B
1.0	-	-	59‡	30	14	30	30
1.2	18†	30	38‡	21	-	30	30
1.5	18†	27	-	-	-	14	16
1.8	-	12†	-	-	-	-	-

† $N_t = 2$

‡ $N_t = 6$

For a circular transducer of radius a_t, the farfield begins at $R_c = \pi a_t^2/\lambda$ and the last axial pressure maximum in the nearfield occurs at $R_c' = a_t^2/\lambda$, where λ is the wavelength (*Zemanek*, 1971; *Clay and Medwin*, 1977). The values are listed in Table 2.2. R_1 ranged from 32 cm to 34.2 cm. Thus, measurements were made in the far field for 1.0 and 1.2 MHz and beyond the last sound pressure maximum for all frequencies, i.e. in the region

Table 2.2: Transducer beam pattern properties computed using a water sound speed of 1480 m/s and $a_t = 0.011$ m (*Wilson and Hay*, 2015), where R_c is the nominal start of the farfield and R_c' is the range to the last axial pressure maximum. The -3 dB beam half-widths θ_0 and the sidelobe angles θ_s are also given.

f [MHz]	R_c' [cm]	R_c [cm]	θ_0 [°]	θ_s [°]
1.0	8.1	26	2	6.3
1.2	9.8	31	1.7	5.3
1.5	12.2	39	1.3	4.2
1.8	14.7	46	1.1	3.5

of the directivity pattern falling off at, or more slowly than, $1/R_1$.

N_t repeat trials for each grain size and frequency were conducted (see Table 2.1). After completing a trial, the sand or beads were collected into their containers underwater and kept in the tank. The stack of cylinders was then reset for the next trial. After completing the N_t trials for a given sample, the tank was drained, cleaned to remove the sample completely, and then refilled with distilled water. The next sample was placed in containers and kept underwater for several days to allow the water and sample to degas before carrying out the repeat trials.

In a second set of experiments, the sediment samples were boiled in distilled water in a 28.4 L aluminium container for 30 min at 100°C. After letting the samples reach room temperature, the grains were transferred from the container to the experiment tank, while being careful not to introduce air. The transfer was achieved by fully immersing a small container underwater in the aluminium container and filling it partially with boiled grains. The small container was slowly lifted out of the aluminium container and then slowly immersed into the measurement tank. These steps were repeated until all of the boiled samples were transferred. Measurements were then made following the procedure outlined above.

2.3.2 Sand and glass bead properties

Three bulk samples of different size quartz sand, designated S1, S2 and S3, and one bulk sample of soda lime glass beads, designated G, were used in the present experiments. The grain size distributions are presented in Fig. 2.5. The median sizes, d_{50}, are listed in Table 2.3. Scanning electron microscope (SEM) images of multiple grains of each material are

Table 2.3: Median grain size d_{50}, porosity n, and grain density, ρ_s.

	d_{50} $[\mu\text{m}]$	n	ρ_s $[kg/\text{m}^3]$
		Sand	
S1	219	0.411 ± 0.006	2642 ± 5
S2	406	0.409 ± 0.002	2652 ± 2
S3	497	0.412 ± 0.008	2648 ± 1
		Glass beads	
G	336	0.397 ± 0.005	2456 ± 25

shown in Fig. 2.6 and of a single glass bead and a single grain of sand (S2) in Fig. 2.7. While many of the glass beads were nearly perfect spheres, others were oblong and many had pits and/or protrusions on their surfaces (Fig. 2.7a). In comparison, the sand grain shapes are highly irregular (Figs. 2.6 and 2.7b).

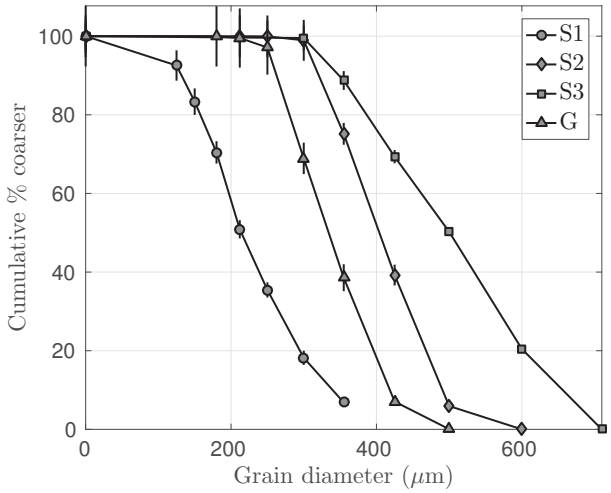

Figure 2.5: Grain size distributions for the glass beads (G) and the three different sands (S) used in the experiments. The error bars indicate the standard deviations from the mean of the results from 3 replicate samples.

Grain density, ρ_s, was measured by adding a measured mass m_s (about 100 g) of dry material to a volumetric flask of volume $V_T = 200$ mL. Distilled water was added – in an amount such that the surface of the granular material was ~ 2 cm below the surface of the water – and the contents were boiled for 15 min in order to remove air bubbles. After allowing the flask to cool, distilled water was topped up to the 200 mL mark. The water temperature was then measured and used in calculating the water density, ρ_w, using

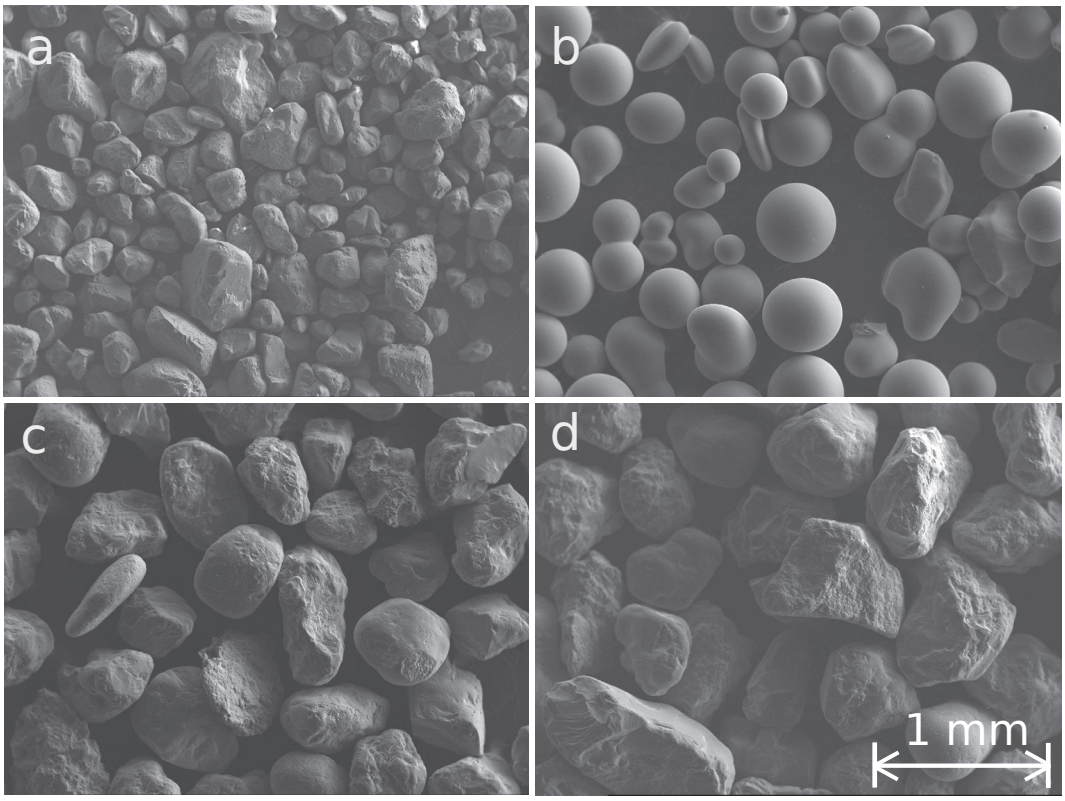

Figure 2.6: Scanning Electron Microscope (SEM) images of sub-samples of the sand grains (S) and glass beads (G): (a) S1; (b) G; (c) S2; (d) S3.

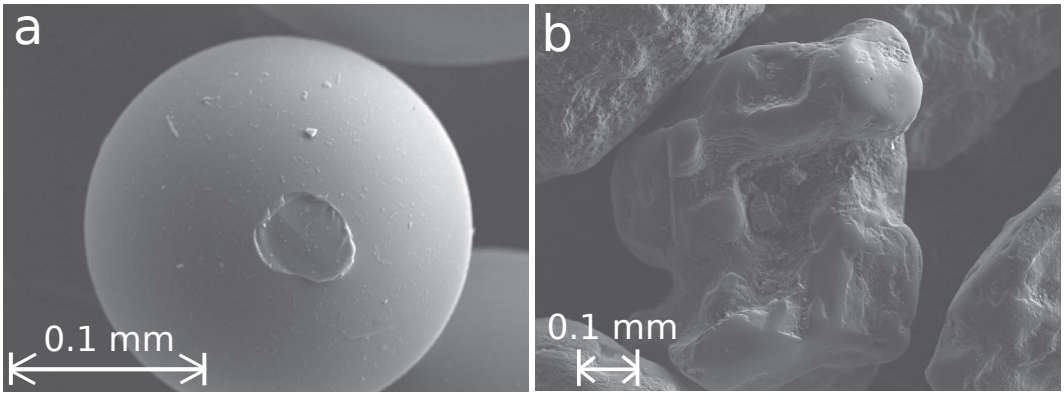

Figure 2.7: Scanning Electron Microscope (SEM) images of single grains: (a) glass bead (G); (b) sand grain (S2). Note the pit in the glass bead and the highly irregular overall shape and complex small scale roughness features on the surface of the sand grain.

the empirical equation of state for freshwater (*Millero and Poisson*, 1981). The water mass, m_w, was determined by subtracting the initial mass of the flask and m_g from the

total mass of the flask and its contents. Density was then determined using $\rho_s = m_s/V_s$, where $V_s = V_T - m_w/\rho_w$. The means and standard deviations, based on three replicate measurements for each material, are listed in Table 2.3.

Porosity was measured by progressively adding a measured mass (about 15 g) of dry material to a 100 mL graduated cylinder containing a known volume of distilled water (about 40 mL). Porosity n is given by

$$n = 1 - V_s/V_b \tag{2.3}$$

where V_s is the volume of the grains and V_b is the bulk volume of the water-grain mixture. Bulk volume was recorded after each addition. The number of additions ranged from 5 to 8. Nothing was done to compact the granular material. Porosity was then calculated from the slope of the least-squares best fit of V_s versus V_b using Eq. 2.3. The means and standard deviations, based on three replicate measurements for each of the four granular materials, are listed in Table 2.3.

To determine whether the porosity obtained via the graduate cylinder method was representative of the porosity of the granular material in the nested cylinders, porosity was also measured on samples which underwent the same mechanical treatment as that used for the nested cylinder trials. This second set of measurements was made for the glass beads and one of the sand sizes (S1) using two cylindrical blocks of PVC (5 cm height, 8 cm diameter). A cylindrical well was machined out of each block with diameters of 7.3 cm and 6.6 cm and depths of 0.97 cm and 1.9 cm. These depths are within the range of thicknesses used for the attenuation and sound speed measurements. The block was placed on a tray which rested on the bottom of the measurement tank filled with water. A measured mass of dry material in a beaker was slowly submerged in the tank, stirred to release air bubbles, and then slowly poured into the well. Similar to the experimental procedure outlined in Sec. 2.3.1, a straight-edge longer than the block diameter was used to scrape off excess granular material which was collected in the tray. The tray and block were then slowly lifted out of the water. The granular material in both the tray and the well were collected, dried and weighed. For both S1 and G, three measurement replicates for each well depth were executed.

The mass of the material contained within the well was estimated in two ways: (a) the measured mass of the material collected from the well, M_1, and (b) the initial mass less

the mass of the material collected in the tray, M_2. M_1 was consistently lower than M_2, but by less than 0.4%, and the standard deviation of the differences between M_1 and M_2 over all six estimates was less than 0.2 %. Note that there was no consistent bias between the two well depths and that the material loss – the ratio between the total mass of the material before and after the porosity measurement – was less than 0.3%. The volume of grains contained within the well, V_s, was determined from the mean of M_1 and M_2 using ρ_s. Using Eq. 2.3 with V_b given by the volume of the well based on its measured depth, the mean porosity based on the three replicates for each well depth was determined. The overall average porosity and standard deviation was 0.418 ± 0.007 for S1 and 0.387 ± 0.006 for G. These estimates are within 2.5% of the porosity measurements listed in Table 2.3.

2.3.3 Analysis methods

For each frequency and cylinder size, the backscatter signals from ten transmit pulses were acquired. These signals were ensemble averaged and the result was low-pass filtered using a fifth-order Butterworth filter with a 5 MHz cut-off. Examples of the low-pass filtered return signal are shown in Fig. 2.8 for two sand layer thicknesses from a single trial. The envelope of the signal was obtained via the Hilbert transform. For each sand thickness (and therefore each cylinder), the signal envelope was cross-correlated with the envelope from the return of the sediment-water interface for the tallest cylinder. The maximum of this cross-correlation gave the estimated position of the sediment-water interface (black circle). The cross-correlation method was not effective for identifying the disk return since its shape changed for different sand thicknesses. Thus, the position of the disk (white circle) was determined by finding the maximum of the envelope closest to the expected arrival time of the signal from the disk. Since the disk was always placed at the same nominal distance from the transducer, the expected arrival time changed very little.

Useful data were not always acquired from all 10 cylinders for all trials. Data from a cylinder was rejected if the disk return saturated the receiver, which typically occurred for the thinner sand layers, or if the disk return was too weak relative to the background reverberation (see results section), which occurred for the thicker sediment layers at higher frequencies. The total number of cylinders, N_c, considered out of a possible total equal to 10 times the number of trials, N_t, are listed in Table 2.1 for each sediment sample and frequency.

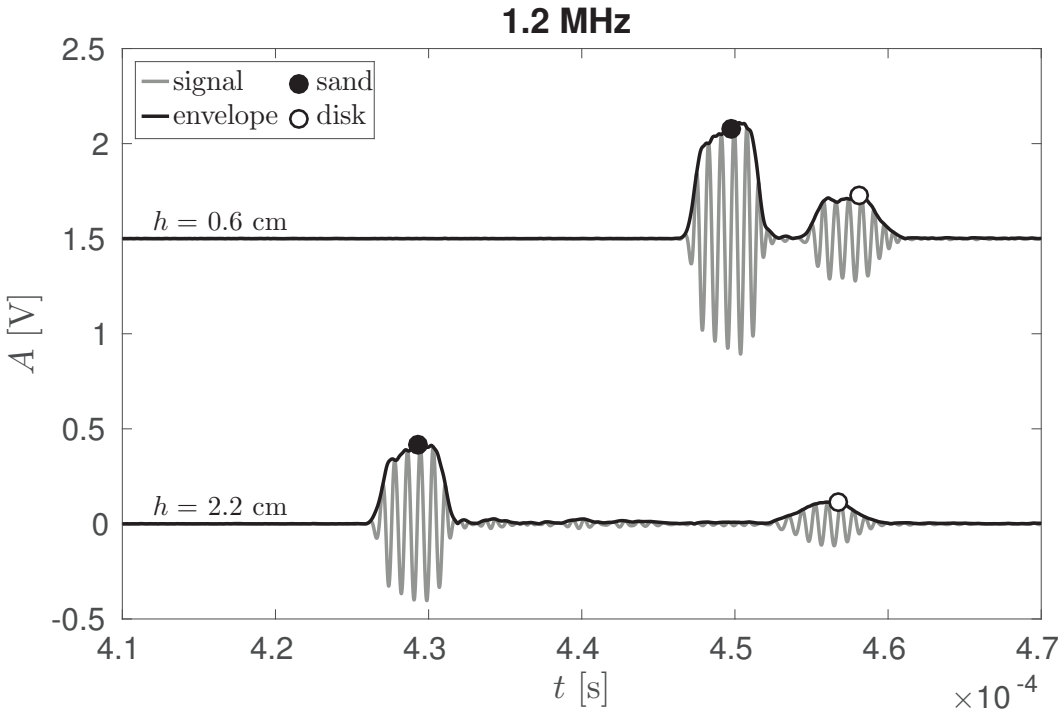

Figure 2.8: Return signal from a single trial at 1.2 MHz (grey) and its envelope (black) for two $S1$ sand thicknesses above the Delrin disk (0.6 cm and 2.2 cm). The estimated arrival times from the sand-water interface and the surface of the Delrin disk are indicated by the black and white dots, respectively.

2.4 Results

2.4.1 Signal-to-noise ratio

Background reverberation in the time interval between the sediment-water interface return and the bottom return was observed in the recorded signal (see example return for 2.2 cm thick sand in Fig. 2.8). To determine the RMS reverberation amplitude, the corresponding time interval was defined to be that between the first minimum in the envelope of the signal after the sediment-water interface arrival and the last minimum before the disk arrival: i.e. in Fig. 2.8, for example, between 432 and 452 μs for the $h = 2.2$ cm return. With σ the standard deviation of the low-passed return signal during this time interval, the signal-to-noise ratio, SNR, is defined as the amplitude of the disk return divided by 2σ. In Fig. 2.9a, SNR is plotted as a function of kd_{50} for three sand thicknesses and all grain sizes. These sand thicknesses were chosen so that the reverberation time interval exceeded 3.5 pulse lengths, yet was small enough that runs from all four grain sizes could be included. Regardless of grain size or sand thickness, the SNR decreases with increasing kd_{50}.

The percentage of runs that were retained, $P = 10N_c/N_t$, is plotted as a function of kd_{50} in Fig. 2.9b and c for unboiled and boiled samples. For $kd_{50} < 2$, P lies between 60% and 100%, and for higher kd_{50}, $36\% < P < 70\%$. The lower retention rate at higher kd_{50} is due to two effects: the higher attenuation and therefore reduced amplitude of the return from the disk; and the higher amplitude reverberation levels. This latter effect is attributed to variations in the sediment fabric on the grain scale, e.g. clustering among the grains.

2.4.2 Attenuation

Assuming plane wave propagation (justified in Sec. 2.8), let the amplitude, A, of the detected return from the disk be represented by

$$A = A_0 e^{-2\alpha h} \tag{2.4}$$

where α is the linear attenuation coefficient for pressure and A_0 is a constant. In Fig. 2.10, the values of $\ln A$ at 1.2 and 1.5 MHz from a single trial, together with the linear least-squares best fit straight lines, are plotted as a function of sediment thickness, h,

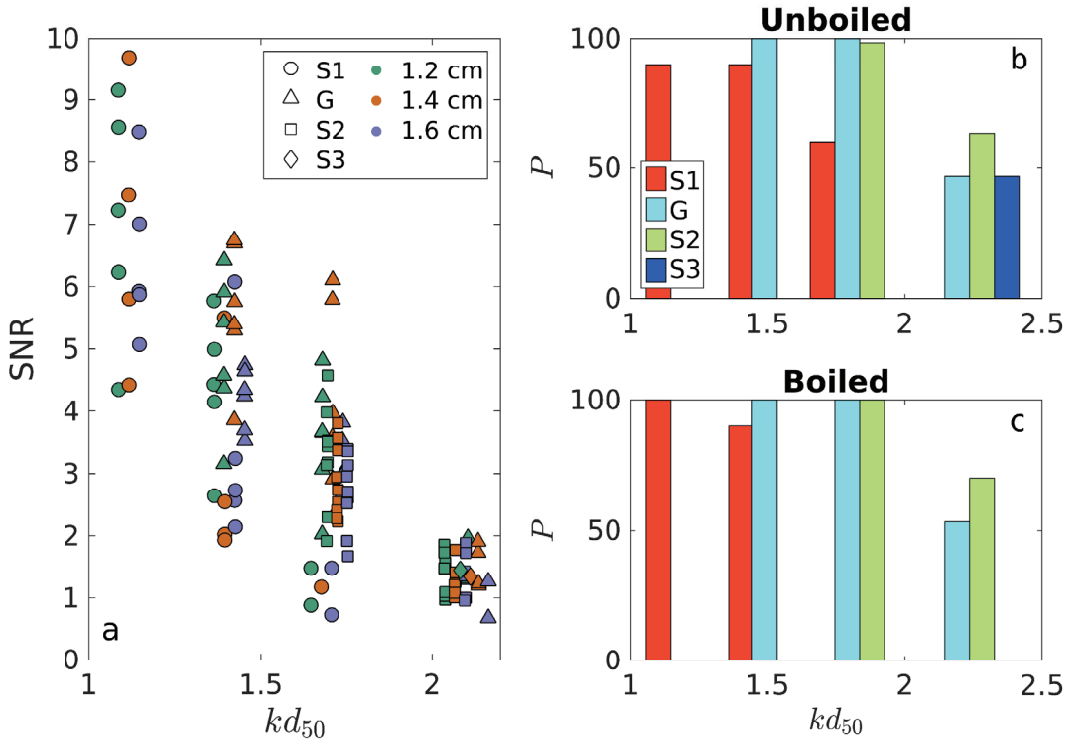

Figure 2.9: (a) Signal to noise ratio for three sand thicknesses (marker color) and the different grain types (marker shape), including measurements for boiled and unboiled samples. Percentage of runs retained for the attenuation and sound speed fits, P, as a function of kd_{50} for (b) unboiled and (c) boiled samples. In all panels, the data have been offset in the horizontal to avoid overlap.

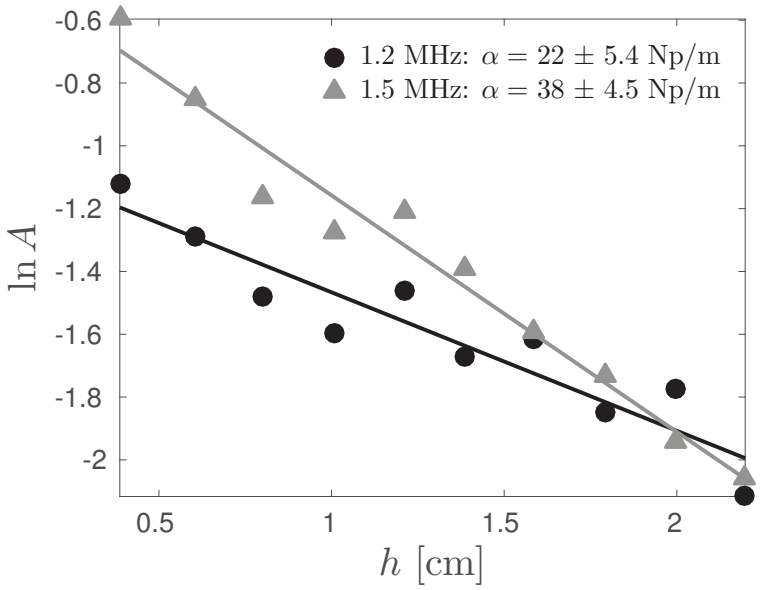

Figure 2.10: Plot of $\ln A$ from a single trial, A being the amplitude of the return from the Delrin disk, as a function of S1 sand thickness for 1.2 MHz and 1.5 MHz. The solid lines are the least-squares best fits. The attenuation coefficients determined from the fits are indicated.

determined from the cylinder height. The attenuation coefficients determined from the slopes and the 95% confidence limits for the fits, $\delta\alpha$, are indicated in Fig. 2.10. For each frequency and grain size, the mean values of α and the average error over N_t trials (i.e. $\sqrt{\Sigma_{i=1}^{N_t}(\delta\alpha_i)^2}/N_t$) are listed in Tables given in Sec. 2.9.1. Also listed is c_{wc}, the water sound speed based on the measured water temperature computed using the Matlab seawater package (*Morgan*, 1994), which is based on equations from *Fofonoff and Millard* (1983).

The attenuation estimates from the present work are plotted in Fig. 2.11 together with the results from the literature, using k based on c_{wc}. Also shown in Fig. 2.11 are the predictions from the multiple-scattering model of *Schwartz and Plona* (1984), given by Eq. 2.1, and the BIMGS+SP model from *Kimura* (2011). The present α estimates are comparable to those that have been reported in the literature using the transmission method, both the values for glass beads and the values for sand. The new results are also consistent with the $(kd)^4$ curve predicted by multiple scattering theory at the higher values of kd and, as kd decreases toward 1, with *Kimura*'s blending of the multiple scattering and viscous loss models.

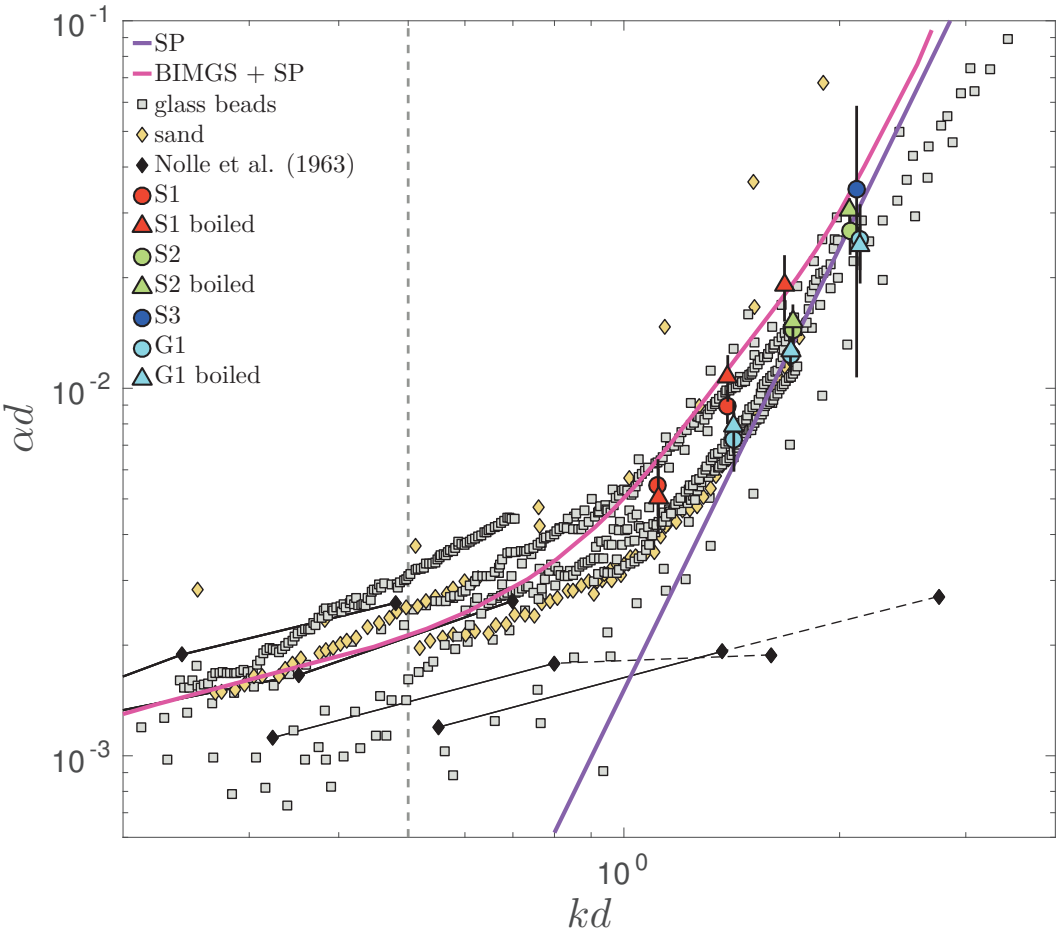

Figure 2.11: Attenuation (in Np/m) vs wavenumber in water, both non-dimensionalized by the grain diameter. The solid lines are two of the model results, as indicated in the legend. The present measurements are indicated by the larger red, green, blue and cyan circles and triangles, where triangles represent boiled grain results. Vertical black lines indicate the error based on the 95% confidence intervals. Otherwise, the symbols are the same as Fig. 2.2.

2.4.3 Group speed

The results for the time difference, δt, between the returns at 1.2 and 1.5 MHz from the sediment-water interface and the disk are plotted as a function of h in Fig. 2.12 for a single trial. Accounting for two-way travel, the slope of a linear least-squares fit of h to δt yields the group speed, c_g, in the water-saturated granular medium. The 95% confidence intervals for the fits are also indicated in Fig. 2.12. Similarly, the measured water sound speed, c_w, was determined from the best-fit slope of $t_0 - t_i = 2(H_i - H_0)/c_w$, where t is the arrival time from the sediment-water interface, H is the cylinder height, the subscript i denotes the i^{th} cylinder and the subscript 0 denotes the shortest cylinder. For each frequency and grain size, the mean values of c_g and c_w are listed in Tables in Sec. 2.9.1, together with their error estimates computed in the same manner as those for attenuation.

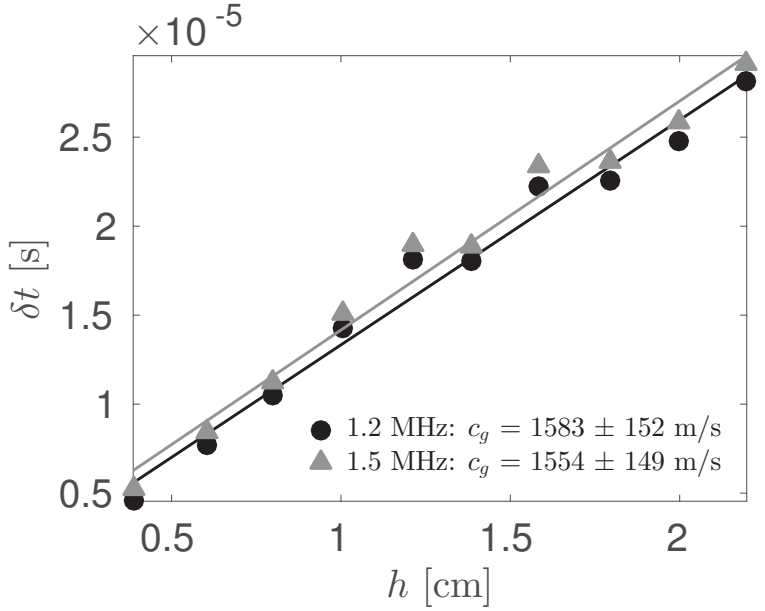

Figure 2.12: The time difference δt between the returns from the sediment-water interface and the surface of the Delrin disk from a single trial as a function of S1 sand thickness h for 1.2 MHz and 1.5 MHz. The solid lines are the least-squares best fits. The group speeds determined from the fits are indicated.

In Fig. 2.13, reported group speeds are plotted as a function of kd. In order to eliminate the effect of temperature, the data have been normalized by the reported water sound speed when indicated and 1480 m/s when not. For those cases in the literature which

reported only phase speeds, the group speed was determined by fitting a third order polynomial to their reported phase speed measurements and then using

$$c_g = \frac{c}{1 - \omega/c\,\partial c/\partial\omega} \tag{2.5}$$

where $\omega = 2\pi f$ and c is the phase speed. Included in Fig. 2.13 are *Thomas and Pace* (1980)'s measurements of *phase speed* at long wavelengths in water-saturated sand. Since their measurements were made for $kd < 0.2$ – i.e. in what should be the non-dispersive limit – they are taken to be equivalent to the group speed. The orange curve representing *Schwartz and Plona*'s multiple scattering prediction was obtained using Eq. 2.5 with c given by Eq. 2.2 and $c_0 = 1790$ m/s for their measured grain size of 545 μm.

The results from the present experiment are indicated in Fig. 2.13. The larger error for the largest grain size (S3) is due to the low number of usable thicknesses (see Table 2.1). All of the data, including the present results, exhibit the expected negative dispersion for $kd \gtrsim 1$. For any given value of kd, however, there is a ca. 10% variation in the group speed. Possible contributions to this variation are pursued in the Discussion.

2.5 Discussion

2.5.1 The *Nolle et al*. (1963) attenuation results

Our attenuation estimates are comparable to those reported in the literature in the $kd > 1$ range using the two-transducer set-up and are consistent with the $(kd)^4$ dependence predicted by multiple scattering theory. In contrast, the *Nolle et al*. (1963) results, obtained with a single transducer method similar to that used here, do not exhibit a tendency toward this $(kd)^4$ dependence, and the values of α at the two highest values of kd are as much as two orders of magnitude lower than the *Schwartz and Plona* (1984) theory and the other measured values including those obtained here. Possible reasons for the discrepancy are discussed below.

Nolle et al. (1963) did not present their attenuation measurements as a function of frequency, but instead plotted attenuation versus the combined parameter $\sqrt{\omega}/d$. Thus, points for a given frequency and grain size are unambiguously identifiable for only the highest and lowest values of $\sqrt{\omega}/d$. However, the results in *Nolle et al*. (1963, Fig. 3) were reported earlier by *Mifsud* (1953) and, as outlined in Sec. 2.9.2, we have used

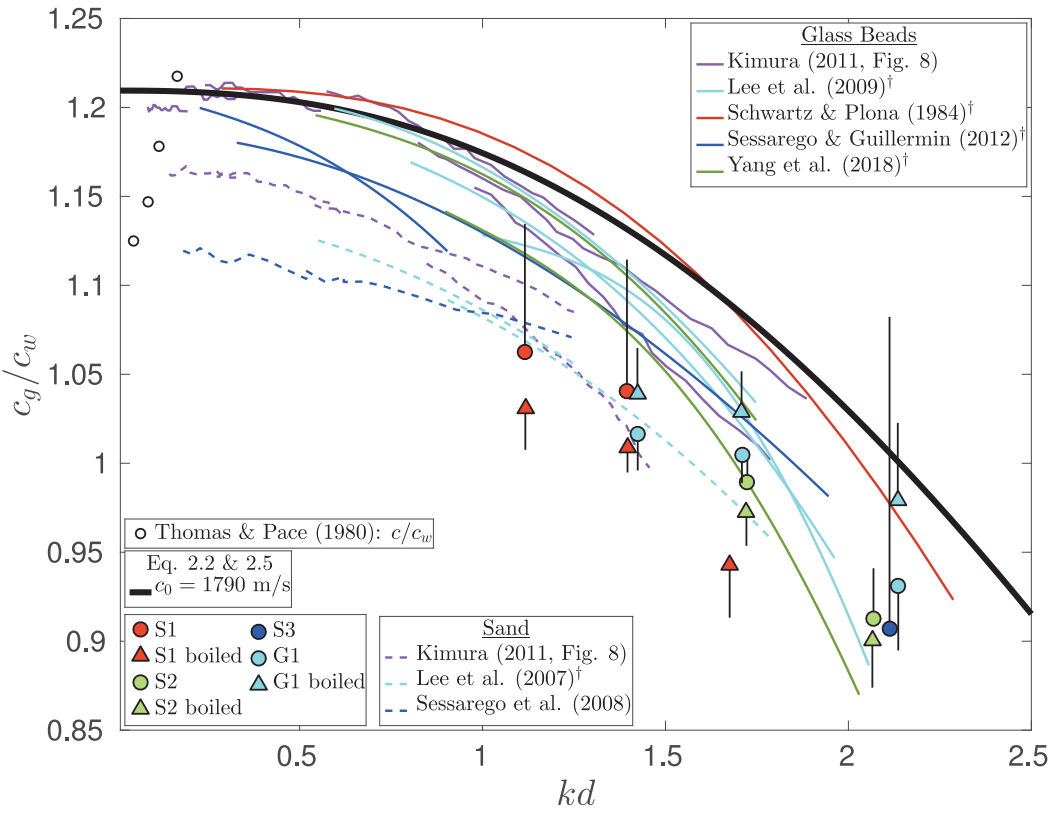

Figure 2.13: Group speed normalized by the phase speed in water (computed for the temperature at which the measurements were made) as a function of kd. Reported measurements for glass beads and sand are indicated in blues and pinks, respectively. The reported measurements indicated by a † were determined by fitting a third order polynomial to the phase speed measurements and then calculating group speed using Eq. 2.5. The estimates from the present work are indicated by the larger red, green, blue and cyan circles and triangles, where triangles represent measurements involving boiled grains. Vertical black lines indicate the error based on the 95% confidence intervals (one-sided to avoid overlap at the same kd). The solid orange line is *Kimura*'s fit to *Schwartz and Plona*'s multiple scattering model (Eq. 2.2). The prediction uses a grain size of 545 μm and Eq. 2.5 to compute group speed.

the information in *Mifsud*'s report to assign grain sizes and acoustic frequencies to the attenuation measurements. The resulting estimates are plotted in Fig. 2.14. Also shown in this figure are the extracted points from the *Chotiros and Isakson* (2004, Fig. 10) interpretation of the *Nolle et al.* (1963) data. The two interpretations are similar for the most part, the important difference being that the points for the two highest values of kd have not been included in the present interpretation. As explained in Sec. 2.9.2, *Nolle et al.*

explicitly state that the numerical values of α for their highest frequency at the two largest grain sizes were not recorded. Their stated reason for not recording these values was that the α values for these runs were much higher than the trend indicated by the results for the lower frequencies and smaller sizes. Importantly, "scattering, rather than viscous losses" were the dominant loss mechanism. As can be seen in Fig. 2.14 dropping the two highest kd points does remove much of the discrepancy between the *Nolle et al.* results and the other data sets, although the two points remaining at $kd > 1$ are still lower than the other data by a factor of three or more. Thus, while even in our reinterpretation the *Nolle et al.* data are not made fully consistent with the tendency toward $(kd)^4$ behaviour for $kd > 1$, a tendency predicted by multiple scattering theory and confirmed by the other available data including the present measurements, it is worth emphasizing that *Nolle et al.* did in fact observe, but did not record, markedly higher values of attenuation at wavelengths comparable to the grain size.

2.5.2 Sound speed

As noted previously, there is considerable – ca. 10% – variation among the sound speed measurements reported in the literature (Figs. 2.3 and 2.13). *Kimura* (2011) has suggested that much of the difference between his measured values of sound speed for glass beads and sand could be attributed to differences in porosity. In the long wavelength limit, the sound speed in a composite medium can be represented by (*Wood*, 1930)

$$c_{LW}^{*} = \sqrt{\frac{K_*}{\rho_*}} \tag{2.6}$$

where K_* and ρ_* are the effective bulk modulus and the effective bulk density.

For a water-grain mixture, the effective bulk modulus is given by (*Wood*, 1930; *Sen and Johnson*, 1983)

$$\frac{1}{K_*} = \frac{1-n}{K_s} + \frac{n}{K_w} \tag{2.7}$$

where K_w and K_s are the bulk moduli of water and grains, respectively. There has been debate in the literature as to the value of the grain bulk modulus to be used for natural sand in water-sand mixtures (*Chotiros*, 1995; *Stoll*, 1998). However, *Richardson et al.* (2002) measured the bulk modulus for Ottawa and quartz sand and obtained values between 3.8 and 4.7 $\times 10^{10}$ Pa, close to the handbook value of 3.6 $\times 10^{10}$ Pa (*Jackson and Richardson*,

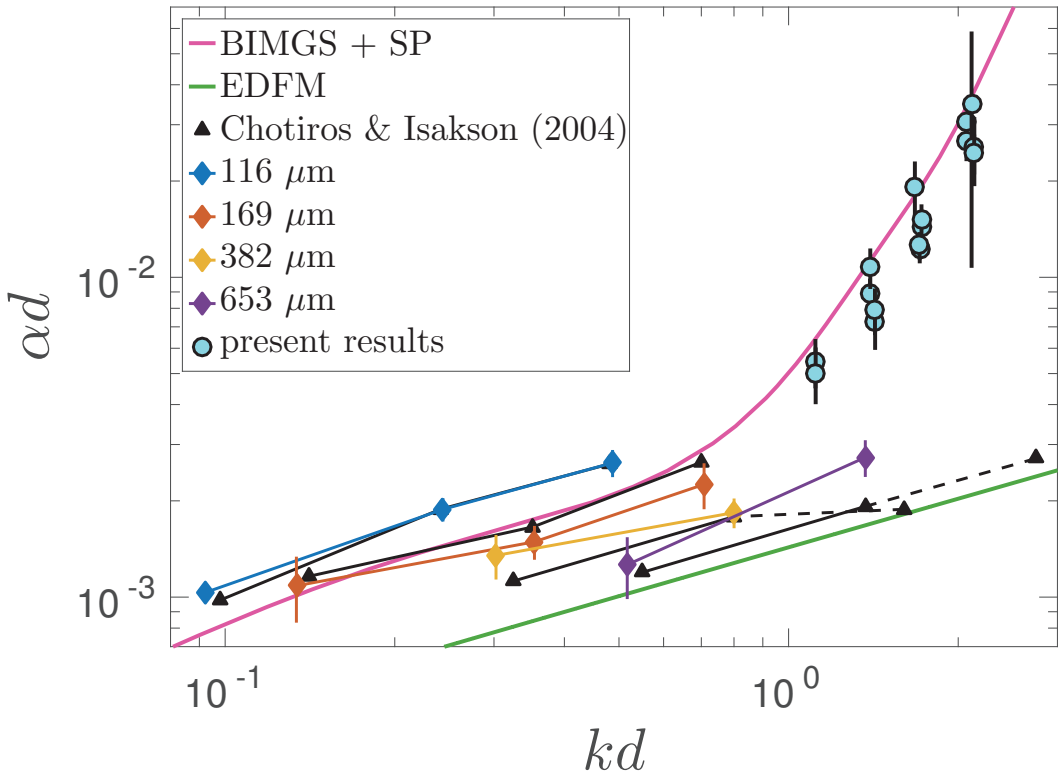

Figure 2.14: Attenuation (in Np/m) vs wavenumber, both non-dimensionalized by grain diameter. Two model results are given: EDFM, the Effective Density Fluid Model (*Williams et al*., 2002); BIMGS+SP, Modified Gap Stiffness Model version of the Biot model for 215 μm sand combined with SP (*Kimura*, 2011). The black triangles are the *Nolle et al*. (1963) data set reported by *Chotiros and Isakson* (2004), with the dashed lines indicating the results at the two largest grain size and the highest frequency. The coloured diamonds are the original *Nolle et al*. (1963) data set extracted from *Mifsud* (1953), see Sec. 2.9.2. The cyan circles are the present results. Vertical black lines indicate the error based on the 95% confidence intervals.

2007). For the calculations here, a value of $K_s = 4.25 \times 10^{10}$ Pa was chosen, the average of *Richardson et al*.'s measured values. Note that since K_w at 20°C is 2.19×10^9 Pa, $K_w/K_s \sim 0.05$: i.e. $K_w/K_s << 1$ for this value of K_s and over the range of values suggested by *Jackson and Richardson* (2007).

The bulk density is normally (i.e. in the Wood's equation sense) written as $\rho_* = (1-n)\rho_s + n\rho_w$. However, sound speeds estimated from *Wood*'s approach are typically in poor agreement with measurements in water-saturated sediments (*Jackson and Richardson*, 2007, p. 267). *Sen and Johnson* (1983) and *Williams* (2001) have shown that the effective density for a dense random packing of loose grains is

$$\rho_* = \rho_w \left[\frac{\xi(1-n)\rho_s + (\xi - 1)n\rho_w}{n(1-n)\rho_s + (\xi - 2n + n^2)\rho_w} \right] \tag{2.8}$$

where ξ is the tortuosity. For $\xi = (3-n)/2$, this equation reduces to (*Sen and Johnson*, 1983)

$$\rho_* = \rho_w \left[\frac{n\rho_w + (3-n)\rho_s}{(3-2n)\rho_w + 2n\rho_s} \right] \tag{2.9}$$

which *Schwartz and Plona* (1984) use in their calculation of sound speed in the long wavelength limit. For $n = 0.4$, the tortuosity ξ is 1.3, close to the best-fit value of 1.35 obtained by *Williams et al*. (2002) when comparing models to field measurements of attenuation and sound speed in sand.

Returning to Fig. 2.3, the sound speed values reported in the literature for water-saturated glass beads in the non-dispersive region at long-wavelengths are 5% higher than those reported for similar-sized sand. As previously indicated, *Kimura* (2011) attributed this difference to the porosities of the two materials. Using Eqs. 2.7 and 2.9 with $K_s = 4.25 \times 10^{10}$ Pa and *Kimura*'s porosity values (0.42 for 215 μm sand and 0.377 for 192 μm glass beads) yields values of 1717 m/s and 1788 m/s, which are comparable to visual estimates of the y-intercepts for *Kimura*'s sand and glass bead data in Fig. 2.3. This agreement raises the question, pursued below, as to how much of the spread in the sound speed measurements at a given kd might be attributable to porosity.

For $K_w/K_s << 1$, Eq. 2.7 reduces to $K_* \sim K_w/n$. Thus, using Eqs. 2.6 and 2.9, the phase speed in the long wavelength limit should, to a first-order approximation, be a function of only porosity, the density of the water, and the grain density of the particles, and independent of the bulk modulus of the particle material, provided that $K_w/K_s << 1$.

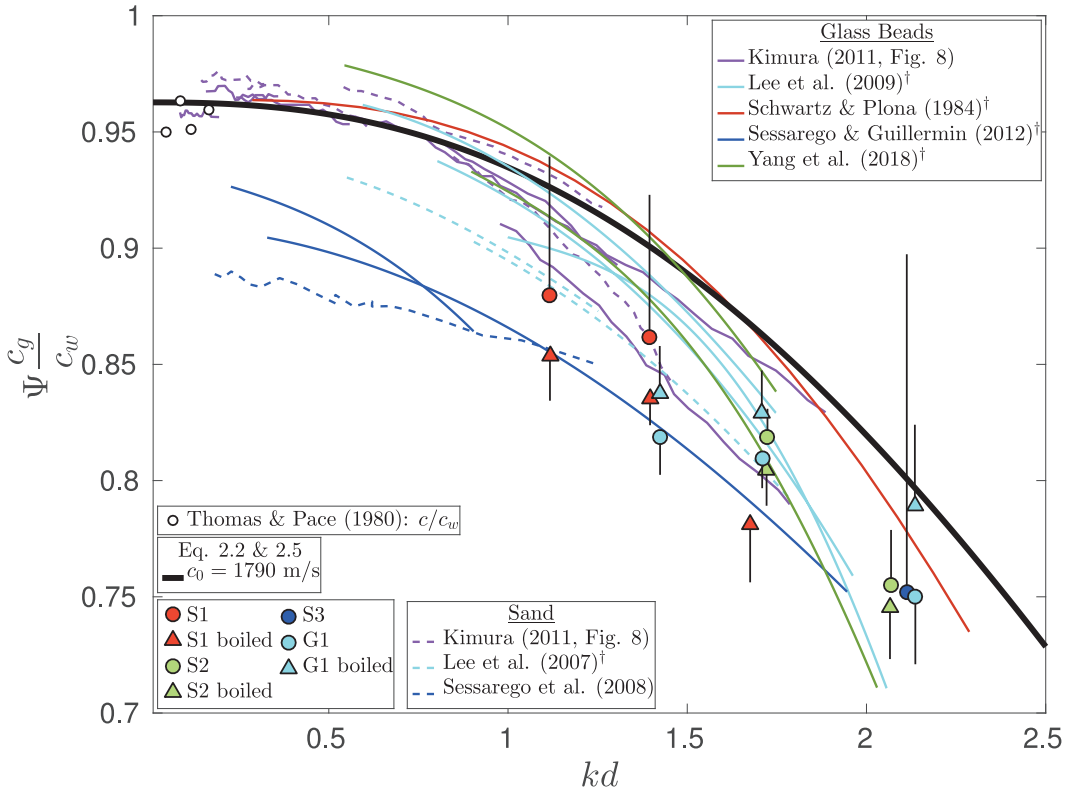

Figure 2.15: Group speed normalized by the phase speed in water and multiplied by $\Psi(n, \rho_s, \rho_w)$ where $\Psi = \sqrt{n\rho_*/\rho_w}$ and ρ_* is given by *Schwartz and Plona*'s expression (Eq. 2.9). See also caption for Fig. 2.13.

Defining $\Psi = \sqrt{n\rho_*/\rho_w}$ with ρ_* given by Eq. 2.9, scaling the observed values of the sound speed ratio by Ψ should largely remove the variations due to porosity. The values of Ψ were determined using the reported porosities, grain and water densities. If no water density was given, a value of 998 kg/m^3 was used. *Sessarego and Guillermin* (2012) did not report a value for ρ_s for their glass beads so it was estimated using their porosity and wet densities. The resulting scaling of the group speeds in Fig. 2.13 is presented in Fig. 2.15 and, as expected, leads to an overall reduction in spread at a given kd.

Focusing first on the data from the literature, the collapse at values of $kd < 0.5$, where the speed is predicted to be non-dispersive, is particularly evident for *Thomas and Pace*'s and *Kimura*'s measurements. Similarly, at higher values of kd, the spread among the different data sets from the literature is much reduced. An exception is the data reported by *Sessarego et al.* (2008b) and *Sessarego and Guillermin* (2012) which plot systematically below the other data sets. Excluding the Sessarego data (discussed further below), the

mean value of the Ψ-scaled speed ratio for $kd < 0.5$ is 0.965, and the 4σ spread is 0.0217, or 2.2% of the mean. If ρ_s is set to a constant value of 2650 kg/m^3, the spread remains 2.2%. For comparison, the spread in the data not scaled by Ψ is 7.5%. Thus, accounting for the variations in porosity alone, and requiring that $K_s >> K_w$, a factor of three reduction in the spread among these data is indicated.

It is well-known that sound speed in water-saturated media is sensitive to the presence of air bubbles. Listed in Table 2.4 are the sediment types (i.e. glass beads or sand), particle sizes and acoustic frequencies used in the studies cited here, together with the bubble removal treatment (when reported). By examining Fig. 2.15 while referring to Table 2.4, it is evident that the data sets which collapse under the Ψ scaling are those from studies in which the water-saturated samples were either boiled or held under vacuum to remove air. There are two data sets which do not collapse – *Sessarego et al*. (2008b) and *Sessarego and Guillermin* (2012). Their data are 5 to 10% – i.e. O(100) m/s – below the other measurements from the literature. Neither boiling nor vacuum treatments were used, and instead bubble presence/absence was partly based on visual observations (see Table 2.4 footnotes). If the bulk modulus, Eq. 2.7, is modified to allow for a volume fraction of air, v_a, the value of v_a required for a 100 m/s reduction in sound speed is only 4×10^{-6}, too small to significantly affect the bulk density. To increase the bulk compressibility of a medium, bubble sizes much less than the acoustic wavelength are required. In the vicinity of $kd = 1$, this implies bubble sizes much less than six times the grain diameter: i.e. O(100) μm or less. Bubbles this size and smaller would be difficult to detect visually at ppm volume concentrations.

With respect to the present data set, some points also fall below the collapsed data in Fig. 2.15, and there is no systematic difference between the measurements for boiled and unboiled samples. While this might indicate that microbubbles were not completely removed, the error bounds on our sound speed estimates do not warrant a definite conclusion. As indicated previously, the main point is that these reflection-based sound speeds are comparable in magnitude to those based on transmission measurements, and exhibit similar negative dispersion, as required for consistency, in the Kramers-Kronig sense, with the f^4 tendency exhibited by the attenuation measurements for $kd \gtrsim 1$.

Table 2.4: Median grain sizes, frequencies and treatment of granular materials reported for the sound speed measurements

Authors [year]	Size [μm]	f [kHz]	Treatment
	Sand		
Kimura (2011)	113, 215, 429, 674	300 - 700	Boiled
Lee et al. (2007)	425	300 - 1000	Boiled
Moussatov et al. (1998)	375	200 - 1200	$*$
Nolle et al. (1963)	100 - 700	400 - 1000	Boiled
Sessarego et al. (2008b)	245	200 - 1200	†
Thomas and Pace (1980)	50, 130, 250, 330, 480	80 - 320	vacuum
	Glass Beads		
Kimura (2011)	67, 125, 192, 451, 642, 781	300 - 700	Boiled
Lee et al. (2009)	375, 625	400 - 1100	Boiled
Schwartz and Plona (1984)	545	300 - 2000	$*$
Sessarego and Guillermin (2012)	272, 520	200 - 800	‡
Yang et al. (2018)	375, 625	350 - 1100	$*$

$*$ treatment not reported

† sand "immersed in fresh water for several months before the experiments and careful degassing operations were performed for several weeks"

‡ repeated pourings of the glass beads under water in the measurement tank until no more bubbles were observed rising from the beads to the water surface.

2.6 Summary and Conclusions

Attenuation and sound speed in water-saturated sand and glass beads were measured for $1.1 < kd_{50} < 2.1$ using a monostatic reflection geometry. The resulting values of attenuation are consistent with previous measurements made using transmission geometries, and with the tendency toward the f^4 dependence predicted by *Schwartz and Plona*'s multiple scattering theory for $kd \gtrsim 1$. The measured group speeds are comparable both in magnitude and negative dispersion to the values reported in the literature and predicted by multiple scattering theory. Scaling the sound speed data by a factor dependent on grain density and porosity reduces the spread in (most of) the measurements by a factor of three – from O(10) to O(1)%, and most of this collapse can be attributed to porosity. The scaling depends on the bulk modulus of the water-saturated sand being O(10) times greater than that of water, consistent with the conclusions drawn by *Jackson and Richardson* (2007) in their review of previous results. The group speeds from two data sets which do not collapse are 5 to 10% low, an amount that – it is suggested – might be attributable to the presence of microbubbles in ppm volume concentrations.

2.7 Acknowledgements

We thank Richard Cheel, Walter Judge and Robert Craig for technical assistance. We also thank Emma Besseau for providing assistance in measuring the grain properties. This work was funded by the Atlantic Innovation Fund, Nortek and by the Natural Sciences and Engineering Research Council of Canada. The literature data and the BIMGS model (*Kimura*, 2011) were extracted from published figures using Web Plot Digitizer (*Rohatgi*, 2015).

2.8 Appendix: Plane Wave Approximation

Using the coordinate system given in Fig. 2.16, the incident pressure distribution from a circular piston transducer at an observation point r is given by

$$p_i = p_* r_* \frac{D(\theta)}{r} e^{-\alpha r} e^{i(kr-\omega t)} \tag{2.10}$$

where r_* is a reference distance, p_* is a reference pressure, α is the linear attenuation coefficient for pressure, $\omega = 2\pi f$ and $D(\theta)$ is the transducer directivity. The backscattered pressure from a surface element $dS = r^2 \sin\theta d\theta d\phi$ is given by

$$dp_s = p_i \frac{D(\theta)}{r} F(\theta) e^{-\alpha r} e^{i(kr+\omega t)} dS \tag{2.11}$$

where $F(\theta)$ is the scattering function for the surface given, for example, by Lambert's law, where $|F|^2 = \mu \cos^2\theta$ and μ is a constant (*Jackson and Richardson*, 2007). Integrating and averaging over time yields

$$\overline{p_s^2} = \pi p_*^2 r_*^2 \int_0^{\theta_0} \frac{F^2 D^4}{r^2} e^{-4\alpha r} \sin\theta d\theta. \tag{2.12}$$

Let $r = R_1\sqrt{1+\tan^2\theta}$, where R_1 is the vertical distance between the transducer and the sediment-water interface. Eq. 2.12 becomes

$$\overline{p_s^2} = \pi p_*^2 r_*^2 \frac{1}{R_1^2} \int_0^{\theta_0} \frac{F^2 D^4}{1+\tan^2\theta} e^{-4\alpha R_1 \sqrt{1+\tan^2\theta}} \sin\theta d\theta. \tag{2.13}$$

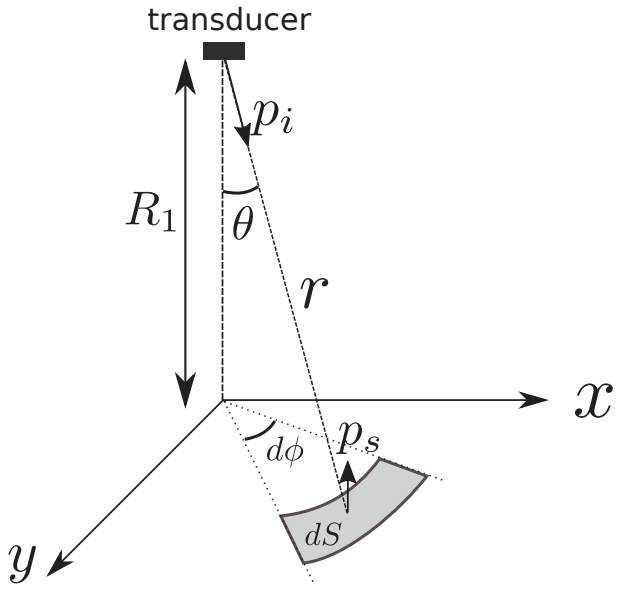

Figure 2.16: Coordinate system used in calculating the backscattered pressure.

Invoking the small angle approximation, justified here by the narrow beam widths

(Table 2.2), Eq. 2.13 reduces to

$$\overline{p_s^2} = \pi p_*^2 r_*^2 \frac{e^{-4\alpha R_1}}{R_1^2} \int_0^{\theta_0} F^2 D^4 \sin\theta d\theta \tag{2.14}$$

where the term $\int_0^{\theta_0} F^2 D^4 \sin\theta d\theta$ will integrate to a constant, provided that F is well-behaved: i.e. that it does not increase dramatically with θ. For 1 MHz ($\theta_0 = 2°$, Table 2.2), this term integrates to 3.310×10^{-4} for $F = 1$ and 3.309×10^{-4} for $|F|^2 = \mu\cos^2\theta$ with $\mu = 1$.

In the present work, R_1 varied from 32 cm to 34.2 cm. The spreading loss corresponding to these two distances is 1.5 Np/m. This value is much smaller than the measured attenuation coefficients that ranged between 20 Np/m to 90 Np/m (see Tables in Sec. 2.9.1), confirming that Eq. 2.4 applies.

2.9 Supplementary Material

2.9.1 Attenuation and sound speed results

Table 2.5: Attenuation and sound speed results for water-saturated sand. Symbols defined in the manuscript. The means and standard deviations are based on values from N_t trials.

Sample	f	N_t	N_c	α		c_g	c_w	c_{wc}
	[MHz]			[Np/m]	[dB/m]	[m/s]	[m/s]	[m/s]
S1	1.2	2	18	25 ± 4.4	216 ± 38	1573 ± 107	1514 ± 132	1480
	1.5	2	18	41 ± 4.4	355 ± 38	1540 ± 110	1516 ± 135	1480
S1 boiled	1.2	3	30	23 ± 4.6	199 ± 40	1526 ± 35	1465 ± 14	1478
	1.5	3	27	49 ± 7.1	426 ± 62	1493 ± 20	1461 ± 18	1478
	1.8	2	12	87 ± 17.9	758 ± 155	1396 ± 44	1469 ± 51	1478
S2	1.0	6	59	36 ± 3.3	308 ± 28	1465 ± 22	1492 ± 21	1480
	1.2	6	38	66 ± 9.1	573 ± 79	1351 ± 42	1484 ± 49	1480
S2 boiled	1.0	3	30	37 ± 4.3	325 ± 37	1440 ± 28	1453 ± 17	1482
	1.2	3	21	75 ± 5.9	653 ± 51	1333 ± 40	1444 ± 41	1482
S3	1.0	3	14	70 ± 48.3	607 ± 419	1343 ± 259	1409 ± 86	1478

2.9.2 Reinterpreting the *Nolle et al*. (1963) data set

Nolle et al. (1963) measured attenuation as a function of frequency (189 kHz, 500 kHz, 1

Table 2.6: Attenuation and sound speed results for water-saturated glass beads. Symbols defined in manuscript. The means and standard deviations are based on values from N_t trials.

Sample	f	N_t	N_c	α		c_g	c_w	c_{wc}
	[MHz]			[Np/m]	[dB/m]	[m/s]	[m/s]	[m/s]
G	1.0	3	30	22 ± 3.9	187 ± 34	1505 ± 30	1455 ± 19	1482
	1.2	3	30	37 ± 3.7	318 ± 32	1487 ± 23	1456 ± 20	1482
	1.5	3	14	76 ± 18.5	659 ± 160	1378 ± 54	1462 ± 52	1482
G boiled	1.0	3	30	24 ± 3.9	204 ± 34	1539 ± 38	1472 ± 32	1483
	1.2	3	30	38 ± 3.7	326 ± 32	1523 ± 34	1472 ± 32	1483
	1.5	3	16	73 ± 10.4	632 ± 90	1450 ± 64	1517 ± 106	1483

MHz) and grain size (116, 169, 382 and 653 μm, peak values from the grain size distributions in their Fig. 1) and plotted α versus $2\sqrt{\omega}/d$ (their Fig. 3) so that individual estimates of α cannot be identified with a given frequency or grain size. However, the data were also originally reported by *Mifsud* (1953), not tabulated unfortunately, but plotted both vs $\sqrt{\omega}/d$ and $\sqrt{\omega\sigma_{dc}}$ where σ_{dc} is the dc flow resistance. The values of σ_{dc} are listed in *Nolle et al*. (1963, Table I) and *Mifsud* (1953, Table 2).

Letting $\chi = \sqrt{\omega}/d$ and $\Gamma = \sqrt{\omega\sigma_{dc}}$, the data extracted from *Mifsud*'s Figs. AS-1654 and Fig. AS-1640 are plotted in Fig. 2.17. The vertical lines in Fig. 2.17a indicate the estimated values of Γ for the three frequencies (line style) and four values of σ_{dc} each of which is associated with a particular grain size (colour). The cluster of points closest to each vertical line was assigned the corresponding values of grain size and frequency indicated in the legend. (Note that the points in the inset of Fig. 2.17a – i.e. those for 653 μm and 500 kHz (purple) and 382 μm and 189 kHz (yellow) – were assigned assuming that the number of points in each group was the same). These values of d and ω were used to compute estimates of χ, designated χ'. The plus signs in Fig. 2.17b represent the values of α at these χ' estimates and can be seen to line up with the original data set (open circles). The average value of α was computed for each value of χ' and these values are plotted in Fig. 14 of the manuscript. It is important to note that no points in Fig. 2.17a cluster around the expected values of $\sqrt{\omega}/d$ for the highest frequency and two largest grain sizes. This is because *Nolle et al*. (1963) state that the observed values of α for these two cases were much higher – which they attributed to scattering rather than viscosity becoming the dominant loss mechanism – and therefore did not record the

numerical values.

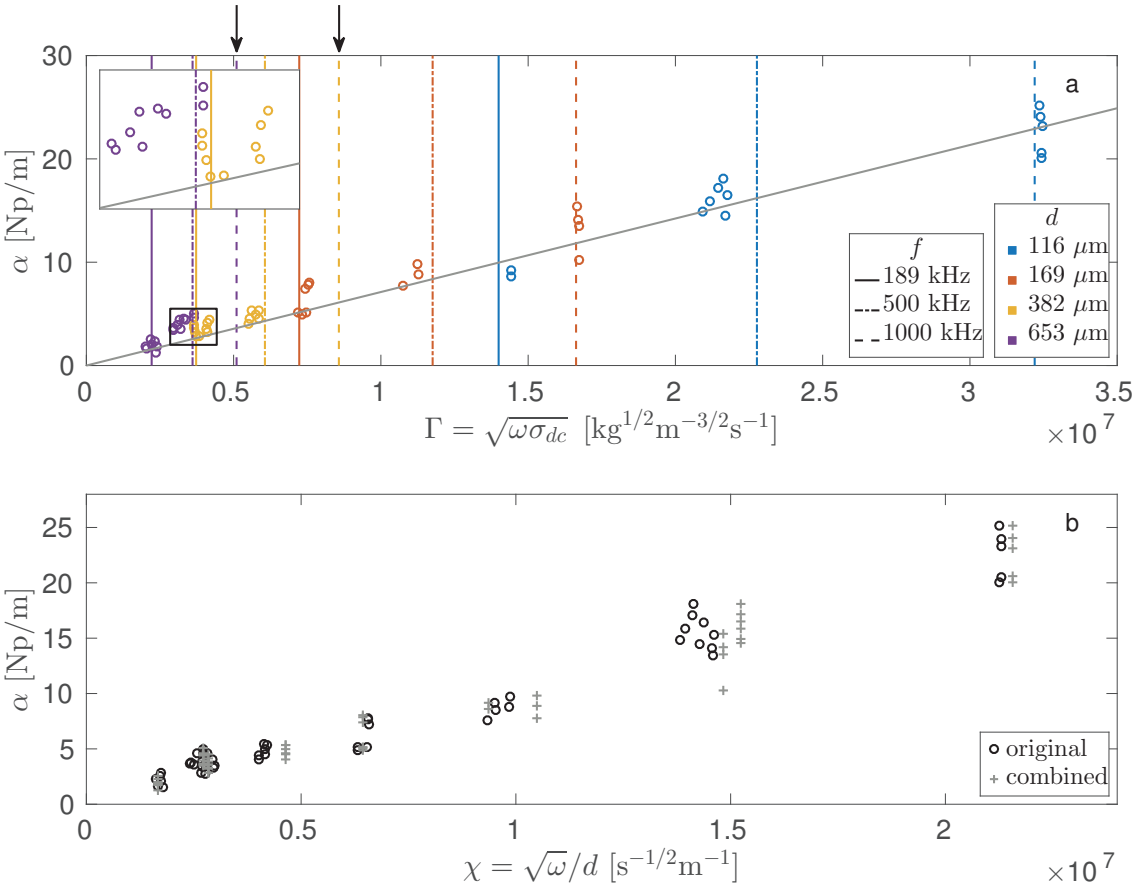

Figure 2.17: (a) Attenuation (in Np/m) as a function of dc flow resistance σ_{dc} and $\omega = 2\pi f$. The data points were extracted from *Mifsud* (1953, Fig. AS-1654). The colour and style of the vertical lines indicates the value of $\sqrt{\omega\sigma_{dc}}$ based on *Mifsud* (1953)'s three frequencies and the dc flow resistance in *Mifsud* (1953, Table 2) given for each grain size. The two black arrows indicate the vertical lines for the two largest grain sizes and the highest frequency. The grey solid line indicates *Mifsud* (1953)'s best fit line, $\alpha = 7.1 \cdot 10^{-7}\sqrt{\omega\sigma_{dc}}$. The inset shows a close-up of the black boxed area. (b) Attenuation as a function of $\sqrt{\omega}/d$. The circles are the original data set extracted from *Mifsud* (1953, Fig. AS-1640). The crosses are plotted at our estimates of χ for each of *Mifsud* (1953)'s three frequencies and four grain sizes.

CHAPTER 3

PHASE SPEED IN WATER-SATURATED SAND AND GLASS BEADS AT MHZ FREQUENCIES

This chapter was first published in *The Journal of Acoustical Society of America*[1]

Abstract

Measurements of the phase velocity of compressional sound waves in water-saturated granular materials are reported for the 1.0 to 2.0 MHz frequency range. The sound speed estimates are based on travel times through granular layer thicknesses ranging from 8 to 17 mm. Three types of granular media were used: 336 μm median diameter glass beads and two natural sands with median diameters of 219 μm and 406 μm. These grain sizes and frequency range correspond to $0.5 < ka < 1.2$, where k is the wavenumber and a the grain radius. To remove trapped air, the samples were boiled under pressure before transfer to the measurement tank. The results are compared to previously reported experimental results and to the *Schwartz and Plona* (1984) multiple scattering prediction, confirming negative dispersion for $ka > 0.5$. Scaling the data by a factor depending on porosity and grain density reduces the spread among the available phase speed estimates by nearly a factor of 2, from 12.5% to 6.9%.

[1]Reproduced from **Hare, J.**, and A. E. Hay, Phase speed in water-saturated sand and glass beads at MHz frequencies, *J. Acoust. Soc. Am.*, 148, 2301–2310, 2020a, with permission of AIP Publishing.

3.1 Introduction

Over the past decades, there has been a growing interest in using underwater acoustic technologies to study the geoacoustic properties of the seafloor (*Jackson and Richardson*, 2007). More specifically, the sound speed in unconsolidated water-saturated sediments is necessary for validating theoretical formulations of compressional wave propagation as well as providing an input for many sediment acoustic models. The dependence of sound speed on the geophysical properties of sand-sized sediment such as grain size, density and porosity has been investigated by many (notably *Hamilton et al*. (1956) and *Williams et al*. (2002)). However, this dependence has mainly been investigated at frequencies for which the wavelength of sound is much larger than the grain size. At these wavelengths, weak positive dispersion has been observed and shown to be consistent with different implementations of Biot theory (*Kimura*, 2011). In contrast, for frequencies at which the acoustic wavelength is comparable to or less than the sediment grain size, negative velocity dispersion has been reported (*Schwartz and Plona*, 1984; *Lee et al*., 2007; *Kimura*, 2011). This negative dispersion at high frequencies is due to multiple scattering as demonstrated by *Schwartz and Plona* (1984), whose multiple scattering model successfully predicted the observed dispersion for water-saturated glass beads.

Most of the available sound speed data have used one of two transducer-sample configurations to measure phase speed: a transmit-receive transducer pair buried in the sediment at different separation distances (*Lee et al*., 2009; *Park et al*., 2009; *Kimura*, 2011) or sediment samples of different thicknesses held between a pair of transducers (*Schwartz and Plona*, 1984; *Page et al*., 1996; *Lee et al*., 2007; *Sessarego et al*., 2008b; *Argo IV et al*., 2011; *Sessarego and Guillermin*, 2012; *Yang et al*., 2018; *Venegas and Wilson*, 2019). *Thomas and Pace* (1980) employed a different configuration: a vertically-aligned pair of transducers with the transmitter in the overlying water and only the receiver buried in the sand. As will be seen, there is considerable spread among the sound speed data at high frequencies in the available literature. This spread has been discussed previously by *Hare and Hay* (2018) in the context of group speed estimates. In *Hare and Hay* (2018), attenuation and group speed were measured within water-saturated granular materials over 1 to 2 MHz using a single transducer reflection-based method. In this paper, compressional wave phase speed is measured using a vertically-aligned pair of transducers similar to the configuration used by *Thomas and Pace* (1980). The natural sand and glass beads

with median grain sizes ranging from 0.22 mm to 0.4 mm used in *Hare and Hay* (2018) are also used here. The results are compared to the predictions of the *Schwartz and Plona* (1984) multiple scattering theory and to values previously reported in the literature. In addition, the scaling factor introduced by *Hare and Hay* (2018) will be shown to considerably reduce the scatter among the phase speed data.

The paper is organized as follows. Theory and previous measurements are given in Sec. 3.2. The experimental set-up and analysis methods are described in Sec. 3.3. Results are presented in Sec. 3.4 and discussed in Sec. 3.5.

3.2 Theory and Previous Measurements

Sen and Johnson (1983) show that, for a dense random packing of loose grains in an inviscid fluid, an effective medium theory based on the multiple scattering theory developed by *Berryman* (1979, 1980) predicts that, at wavelengths long compared to the size of the scatterers, the speed of sound is given by

$$c_{LW}^{*} = \sqrt{K_{*}/\rho_{*}} \tag{3.1}$$

where ρ_{*} is the effective density given by

$$\rho_{*} = \rho_{w}\left[\frac{n\rho_{w} + (3-n)\rho_{s}}{(3-2n)\rho_{w} + 2n\rho_{s}}\right], \tag{3.2}$$

with ρ_{w} and ρ_{s} being the water and grain density, and n the porosity. Eq. 3.2 assumes that the tortuosity, ξ, is given by $(3-n)/2$. The effective bulk modulus, K_{*}, is

$$1/K_{*} = (1-n)/K_{s} + n/K_{w} \tag{3.3}$$

with K_{w} and K_{s} being the bulk moduli of the water and sediment grains, respectively. Note that Eq. 3.1 is in the form of *Wood* (1930)'s equation for a composite medium and that, while Eq. 3.3 is in the standard form for the bulk compressibility, the effective bulk density (Eq. 3.2) takes a very different form (*Schwartz and Plona*, 1984).

Schwartz and Plona (1984) measured phase speed in water-saturated 545 μm diameter glass beads ($n = 0.38$) and obtained good agreement with their multiple scattering prediction using the self-consistent effective medium approximation (EMA). By applying

a best-fit regression to *Schwartz and Plona*'s EMA model, *Kimura* (2014) obtained the following expression for the ka dependence of phase speed

$$\frac{c}{c_0} = 1 - 8.54 \times 10^{-3}(2ka)^{2.45} \tag{3.4}$$

where c_0 is a reference velocity, k is the wavenumber in water and a is the grain radius. For the data of *Schwartz and Plona* (1984), $c_0 = 1790$ m/s, their measured phase speed in the long wavelength limit. *Schwartz and Plona* (1984) showed that their multiple scattering theory for water-saturated granular media tends to Eq. 3.1 in the long wavelength limit with ρ_* given by Eq. 3.2. Note that in this form, ρ_* is independent of frequency and therefore Eq. 3.1 is non-dispersive, whereas *Kimura* (2011) measured phase speeds exhibiting weak positive dispersion for $ka \lesssim 0.1$, consistent with several different implementations of the Biot model.

In Fig. 3.1, previously reported phase speed measurements are plotted as a function of ka. The literature values were converted from frequency to wavenumber using reported water sound speeds when indicated and 1480 m/s when not. Also shown in Fig. 3.1 is the multiple scattering prediction given by Eq. 3.4 for the data of *Schwartz and Plona* using their measured $c^*_{LW} = 1790$ m/s for c_0. Throughout this paper, we have selected c^*_{LW} as the reference velocity used in Eq. 3.4 (see Sec. 3.8 for a discussion of this choice for c_0). Both the theory and the experimental data exhibit negative dispersion for $ka > 0.2$.

3.3 Methods

3.3.1 Sand and glass beads

The sediment samples used in the present experiments are the same quartz sands ($S1$ and $S2$) and soda lime glass beads (G) used in *Hare and Hay* (2018). The details of the procedures used for measuring the sediment parameters are given in *Hare and Hay* (2018). Their measured values of median grain size d_{50}, porosity n and grain density ρ_s are listed in Table 2.3. To remove air trapped within the sediment, the samples were boiled in a pressure vessel. The vessel was then sealed and allowed to cool to room temperature before being transferred to the measurement tank and opened underwater.

As is well known, the sound speed in water-saturated sediment is sensitive to the porosity of the material. The procedures used in the present study for measuring this

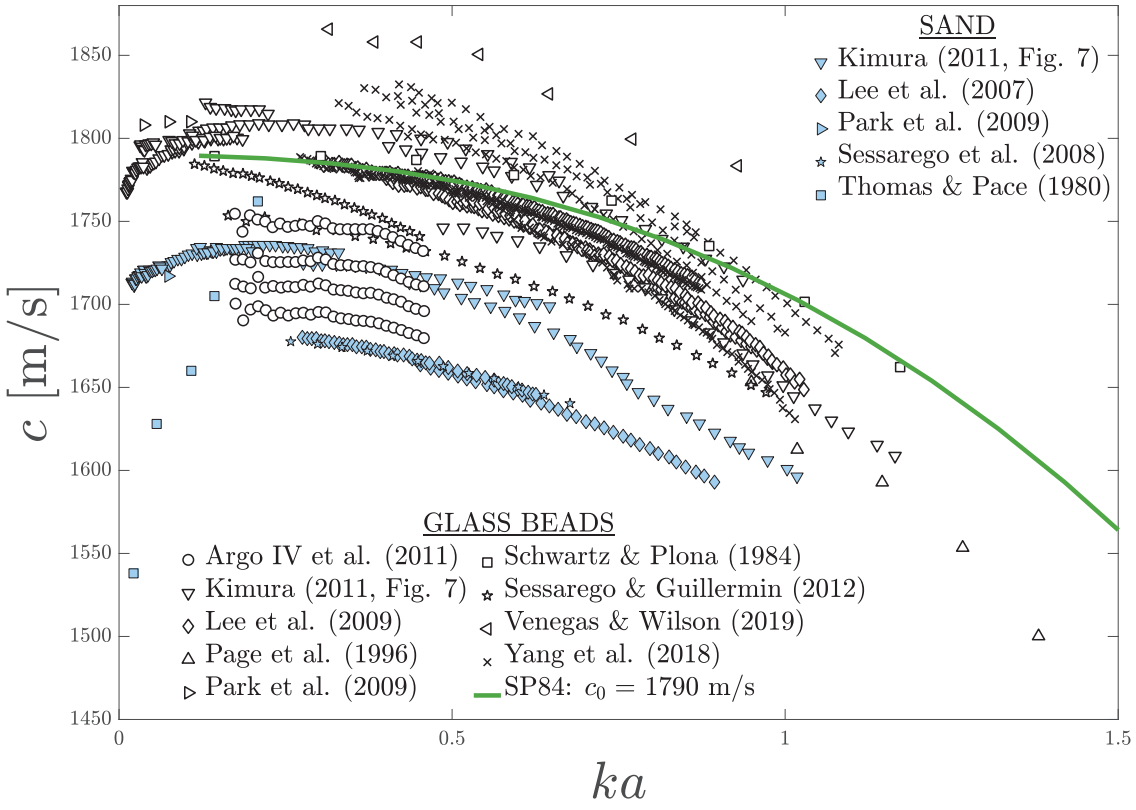

Figure 3.1: Phase speed for saturated water-particle mixtures: glass beads (open) and sand (shaded). The solid line is the best-fit regression of *Kimura* (2014) to the multiple scattering model prediction of *Schwartz and Plona* (1984) for 545 μm glass beads (Eq. 3.4). The ka values for the *Thomas and Pace* (1980) data were computed using 200 kHz, the average over the 80 kHz to 320 kHz frequency band used for their measurements (*Thomas*, 1978, p. 95). Note that the phase speed data reported by *Moussatov et al.* (1998) are not included here because their sand sample had a broad grain size distribution, including clay particles and particles over 1 mm in diameter.

parameter are summarized here. The reader is referred to *Hare and Hay* (2018) for further details. Porosity is given by

$$n = 1 - V_s/V_b \tag{3.5}$$

where V_s is the volume of the grains and V_b is the bulk volume of the water-grain mixture. Three methods were used to determine the values of n. First, a known mass of dry material was progressively added to a known volume of water in a graduate cylinder and the bulk volume was recorded after each addition. Porosity was estimated from a least-squares best fit of V_s to V_b using Eq. 3.5 and then averaged over three repeat trials. These are the values listed in Table 2.3. Second, porosity was estimated using samples which underwent

the same mechanical treatment as that used for the acoustic trials (see Sec. 3.3.2): i.e., by scraping the excess sediment that had been poured underwater into a well machined into the surface of a polyvinyl chloride (PVC) cylinder. Averaged over three repeat trials, the porosity and standard deviation was 0.418 ± 0.007 for $S1$ and 0.387 ± 0.006 for G. These values are within 2.5% of the porosity measurements listed in Table 2.3 with no consistent higher or lower bias. For the third method, the porosity for $S1$ was verified using the same method as that described for the cylindrical blocks, but using a 20.3 (width) x 21.6 (length) x 2.52 (height) cm rectangular PVC tray with a 1 cm deep well. The porosity obtained with this method was 0.419, which is 2% higher than the value listed in Table 2.3.

3.3.2 Experimental set-up

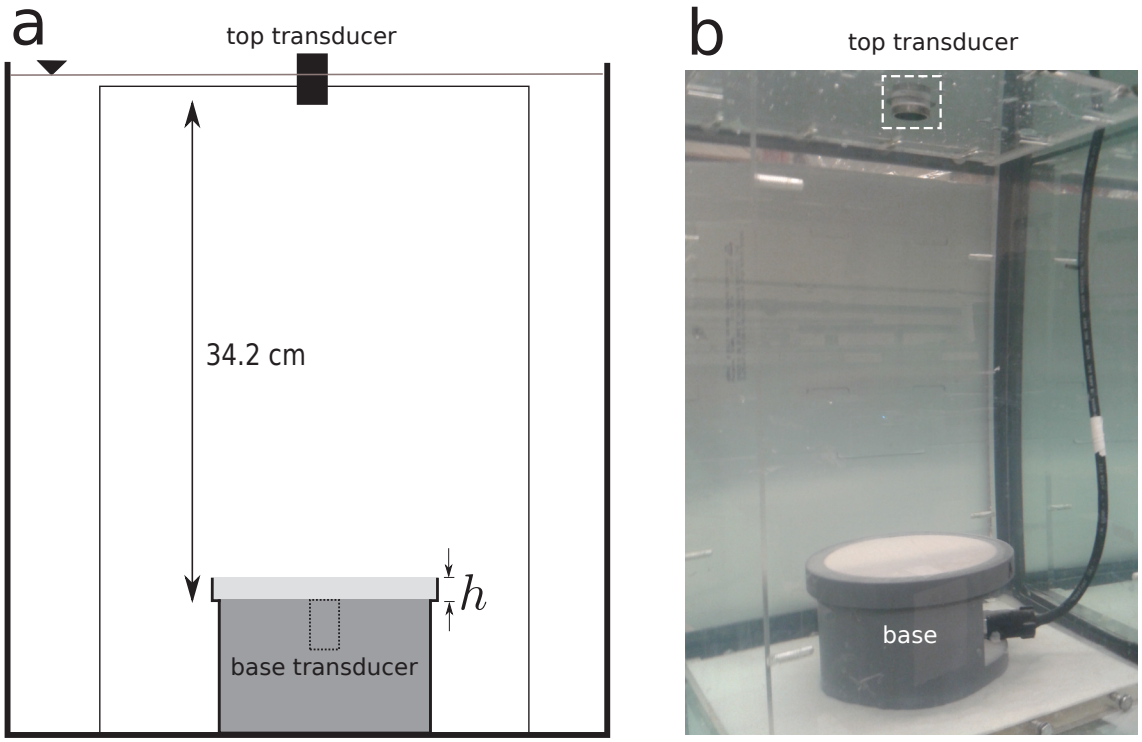

Figure 3.2: Experimental setup: (a) scale diagram (end view of tank), where h is the sediment thickness. (b) photograph.

A scale diagram and photograph of the experimental set-up are shown in Fig. 3.2. A rectangular polycarbonate frame 46 cm high and 30 cm wide was constructed to support the transducer mounts. Two sides of the frame were open to allow for easy access to the sample volume inside. A hole was machined in the top plate, and a circular recess in the bottom plate, with the hole and recess centres aligned. The transmit transducer was

inserted in the top hole, facing down. The receive transducer was mounted in a cylindrical PVC "base" (15.24 cm diameter, 9.63 cm height), which fitted with close tolerance into the recess in the bottom plate, with the transducer face level with the top of the base and facing upward. A lip around the top of the base supported 14.0 cm inner diameter rings of different heights, allowing for the following sediment thicknesses h: 8.0, 12.0, 15.0 and 16.9 mm. The whole assembly was placed in a 43 (width) x 90 (length) x 48 (height) cm rectangular glass-walled tank filled with distilled water. The vertical distance between the transducer and the sediment-water interface varied 32.5 and 33.4 cm.

After seating a given ring on the base, sediment was poured into the ring from containers previously filled while fully immersed in the water-filled tank. To obtain a flat sediment-water interface, the excess granular material was scraped off by carefully drawing a squeegee – longer than the ring diameter – over the ring face. Nothing was done to compact the granular material. After completing the travel time and reflection measurements, the sediment and ring were removed, and the procedure was repeated for the next ring. Three rings were used for $S1$ and four rings for G and $S2$. Three repeat trials were performed for each grain size. The tank was then drained, cleaned and refilled with distilled water, prior to introducing the next sediment sample.

Waveform measurements were obtained using a digital oscilloscope sampling at 125 MHz. The transmit pulse and analogue electronics were the same as those used in *Hare and Hay* (2018). For the travel-time measurements, the pulse duration was 8 μs. Frequencies ranging from 1.0 to 2 MHz were used for the $S1$ sand sample. For the larger grain sizes, the higher attenuation and thus lower signal-to-noise ratio limited the choice of maximum usable frequency. In addition, reflection measurements were made at 1.6 MHz with a 2 μs duration pulse to determine the distance to the sediment-water interface for each sediment-filled ring.

Using the setup described in *Wilson and Hay* (2017), the transducer beam pattern was measured by recording the backscatter from a 16 mm diameter tungsten carbide sphere at a range of 1.5 m and located at different positions perpendicular to the beam axis. The measured beam pattern was fitted to the theoretical beam pattern for a circular piston transducer in the farfield (*Clay and Medwin*, 1977). The effective transducer radius, treated as a fitting parameter, was $a_t = 1.1$ cm, consistent with the 2.2 cm transducer diameter

specified by the manufacturer, Imasonic. The computed transducer beam pattern properties, beam half-widths θ_0 and angles to the first sidelobe maximum θ_s, are listed in Table 3.1. Also given are the ranges to the farfield $R_c = \pi a_t^2/\lambda$ and to the last axial pressure maximum $R_c' = a_t^2/\lambda$, where λ is the wavelength (*Zemanek*, 1971; *Clay and Medwin*, 1977). Measurements were made in the far-field for 1.0 and 1.2 MHz and beyond the last pressure maximum for the higher frequencies.

Table 3.1: Transducer beam pattern properties computed using a water sound speed of 1480 m/s and $a_t = 0.011$ m.

f [MHz]	R_c' [cm]	R_c [cm]	θ_0 [°]	θ_s [°]
1.0	8.1	25.7	2.0	6.3
1.2	9.8	30.8	1.7	5.3
1.4	11.4	36.0	1.4	4.5
1.6	13.1	41.1	1.2	3.9
1.8	14.7	46.2	1.1	3.5
2.0	16.3	51.4	1.0	3.2

3.3.3 Analysis methods

Defining z to be the vertical distance – positive downward – from the transmit transducer, the travel time from the top transducer to the base transducer through a sediment column of thickness h is $t = z/c_w + h/c$, where c_w is the water sound speed, c the phase speed in the water-saturated sediment and z the distance between the transmit transducer and sediment-water interface. For a thickness change δh, the travel time difference is given by

$$\delta t = -\delta h \frac{c - c_w}{c c_w} \tag{3.6}$$

since $\delta z = -\delta h$. Letting $m = -\delta t/\delta h$, it follows that

$$c = \frac{c_w}{1 - m c_w}. \tag{3.7}$$

For each frequency and sand thickness, the received signals from 10 transmit pulses were acquired and ensemble-averaged. Example signals, $A(t)$, recorded by the top and base transducers are shown in Fig. 3.3 for two $S1$ sand thicknesses from a single trial. For $h_2 > h_1$, A_2 leads A_1 and $\delta t < 0$. The lagged cross-correlation function, C_{12},

computed from the ensemble-averaged signals from the base transducer for two sediment thicknesses, was used to determine the travel time difference δt (see example in Fig. 3.4). The time lag was chosen to be the first maximum of C_{12} for positive lags and corresponds to $-\delta t$. Similarly, the sediment thickness difference, δh, was determined from the cross-correlation of the two backscattered signals from the sediment-water interface (identified in grey in Fig. 3.3b). Signals from all possible ring combinations were cross-correlated, i.e. six for $S2$ and G, and three for $S1$.

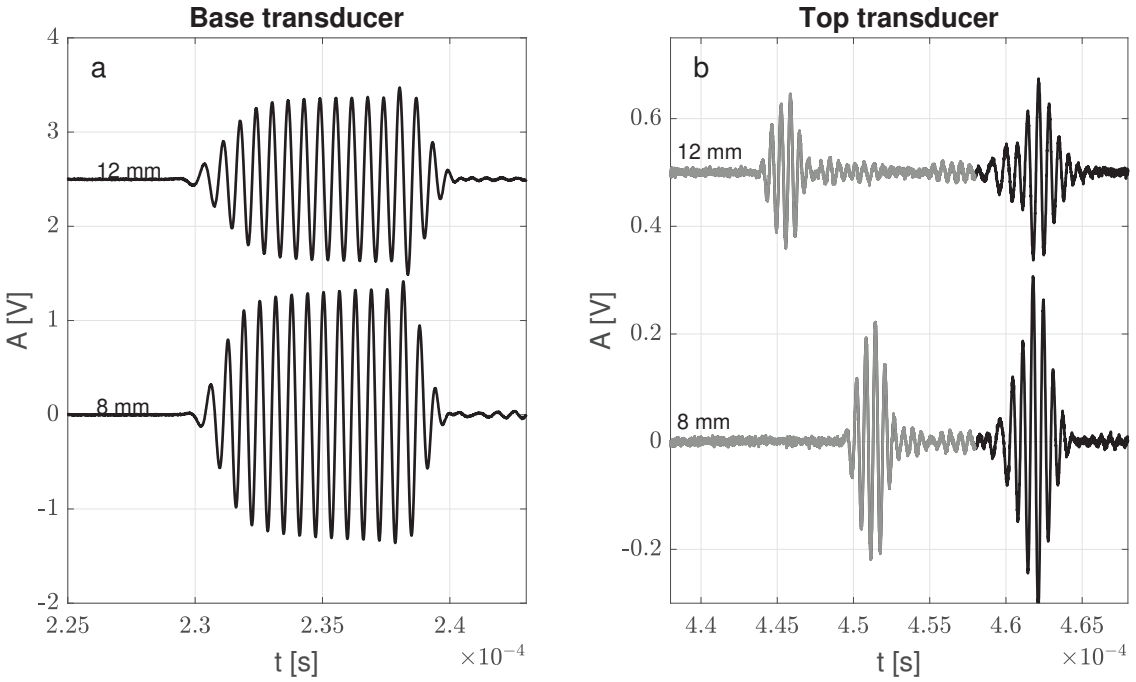

Figure 3.3: Ensemble-averaged signals, $A(t)$, from a single trial at 1.6 MHz for two S1 sand thicknesses (8 and 12 mm) recorded by the (a) base transducer and (b) top transducer, where grey indicates the portions of the reflected signals that were cross-correlated.

In Fig. 3.5, the time delays at 1.0 and 1.6 MHz are plotted as a function of δh for a single glass bead trial. The sound speed in the water-saturated sediment was determined using Eq. 3.7, where m is the slope of a linear least squares fit of $-\delta t$ to δh using the MATLAB function nlinfit. The wider of the two 95% confidence limits for the best fit value of m was used in Eq. 3.7 to compute the sound speed error, δc. For each frequency and grain size, the mean values of sound speed and the standard error for the three repeat trials (i.e. $\sqrt{\sum_{i=1}^{3}(\delta c_i)^2}/3$) were calculated. Similarly, the sound speed was also determined from a fit of $-\delta t$ to the sediment thickness difference based on the measured ring height differences $\delta h'$.

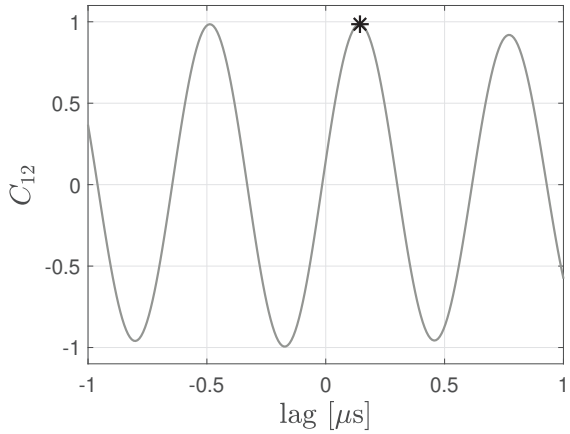

Figure 3.4: Cross-correlation between the two signals given in Fig. 3.3a. The star indicates the first maximum cross-correlation for positive lag.

Using the measured water temperature, water sound speed c_w was computed using the MATLAB seawater package (*Morgan*, 1994), which is based on equations from *Fofonoff and Millard* (1983). In addition, water sound speed was measured by placing a 2.55 cm thick aluminum plate on top of five rings of varying heights in the set-up of Fig. 3.2a. The backscatter data were treated in the same manner as those collected for the sediment-filled rings, that is, signals from the plate resting on top of all possible ring combinations were cross-correlated (i.e ten in this case). The slope of a linear least-squares fit of the measured ring height difference to the time delay between returns yielded the measured water sound speed, c_{wm}, and was within 0.12% of the computed water sound speed, c_w.

3.4 Results

In Fig. 3.6, previously reported phase speeds are plotted as a function of ka. In order to eliminate the effect of temperature, the data have been normalized by the reported water sound speed when indicated and by 1480 m/s (corresponding to 19.2°C) when not. *Kimura* (2014)'s fit to the *Schwartz and Plona* multiple scattering prediction (Eq. 3.4) is plotted for *Schwartz and Plona*'s glass beads with the reference velocity of c_0 set equal to their reported long wavelength phase speed 1790 m/s. The *Schwartz and Plona* curves for the present data were computed using the sediment properties in Table 2.3 using Eq. 3.1 with $K_s = 4.25 \times 10^{10}$ Pa (the average of the measured values of *Richardson et al.* (2002) for Ottawa sand and quartz sand) to compute c_0.

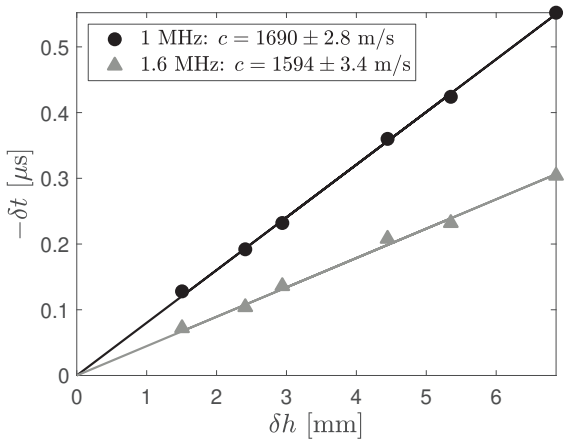

Figure 3.5: Time delay for a single trial as a function of G sediment thickness difference (based on the acoustic measurement) for 1.0 and 1.6 MHz. The solid lines are the least-squares best fits. The phase speeds determined from the fits and 95% confidence limits are indicated.

The results from the present study, normalized by the computed water sound speed, are also shown in Fig. 3.6 for both ways of determining sediment thickness difference. The mean difference between the sediment thickness measurements (δh and $\delta h'$) was 0.8, 0.9 and 1.2 grain diameters for S1, G and S2, respectively. The difference in the phase speed estimates is less than 1%, with the mean over all frequencies and grain sizes being 0.4%. All of the data, including both the present results and measurements from the literature, exhibit the expected negative dispersion for $ka > 0.2$. Concerning our observations, while the model over-predicts the measured sound speeds by about 5%, it correctly predicts that the sound speed in the water-saturated glass beads should be higher than in the two sands, as observed.

3.5 Discussion

As noted by *Kimura* (2011) and *Hare and Hay* (2018), there is considerable variation among the phase speed measurements reported in the literature. Some of this variation has been attributed to differences in porosity (*Kimura*, 2011). *Hare and Hay* (2018) argued that, because the compressibility of water is much greater than that of solid materials like quartz and glass, the phase speed at long wavelengths should depend to first order on only porosity and the densities of the water and the sediment grains, leading to a factor $\Psi = \sqrt{n\rho_*/\rho_w}$ for scaling the non-dimensional sound speed, c/c_w. The spread among

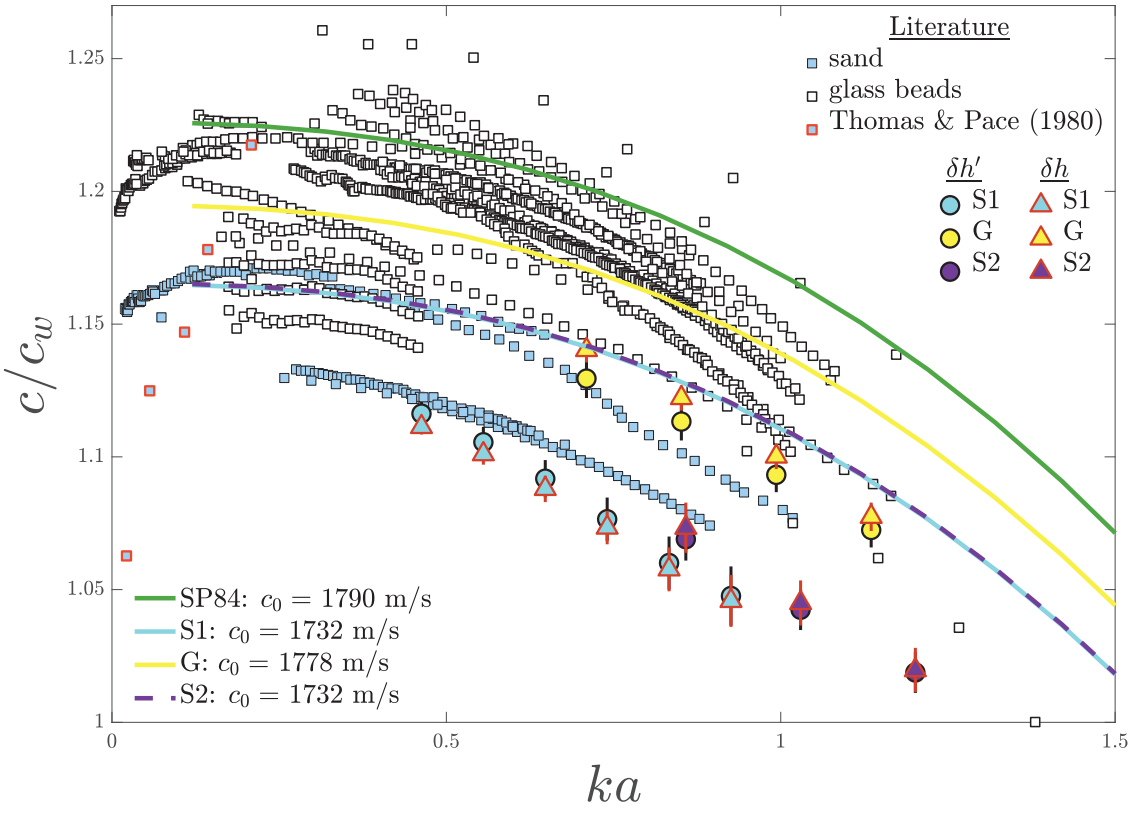

Figure 3.6: Phase speed normalized by the phase speed in water (computed for the temperature at which the measurements were made) as a function of ka. Reported measurements are indicated by squares and the estimates from the present work are given by the circles and triangles. Vertical lines indicate the error based on the 95% confidence intervals. The lines are *Kimura* (2014)'s fit to *Schwartz and Plona* (1984) multiple scattering model (Eq. 3.4) using sediment properties from *Schwartz and Plona* (green) and the present study (cyan, yellow, purple).

the group speeds was considerably reduced after scaling by Ψ (*Hare and Hay*, 2018). In Fig. 3.7, the non-dimensional phase speeds in Fig. 3.6 have been scaled by Ψ. If no water density was given, a value of 998 kg/m^3 was used for the values from the literature. *Page et al*. (1996) did not report a density for their glass beads, so a value of 2500 kg/m^3 was used. For the *Sessarego and Guillermin* (2012) and *Sessarego et al*. (2008b) data, ρ_s was estimated using their porosities and wet densities. Note that their Ψ-scaled sound speed estimates fall below the other literature measurements.

The Ψ-scaling results in an overall collapse of the data, including those from the present study. The present data fall below the multiple scattering predictions, but within the envelope of the literature measurements. The mean difference between our Ψ-scaled

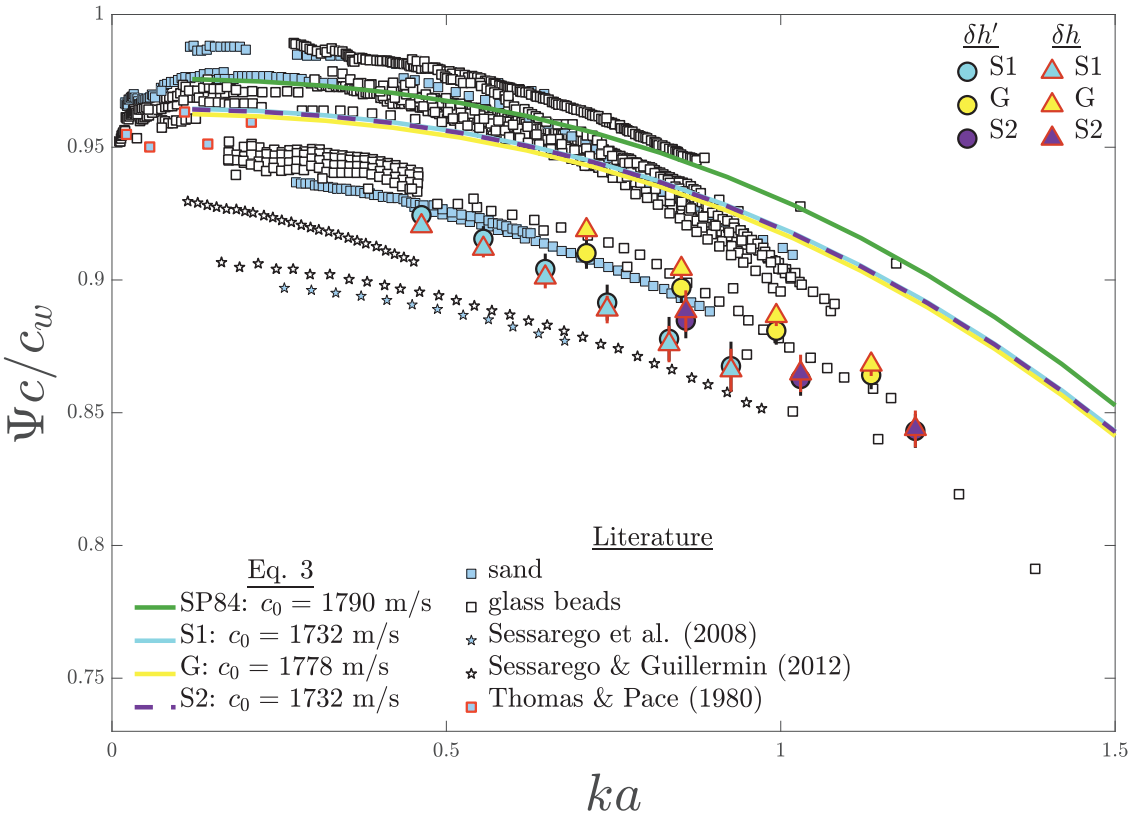

Figure 3.7: Phase speed normalized by the phase speed in water and scaled by Ψ. Data from *Sessarego et al*. (2008b) and *Sessarego and Guillermin* (2012) are indicated. See also caption for Fig. 3.6. Note the significant collapse of the *Thomas and Pace* (1980) data set compared to Fig. 3.6.

measurements and the predictions is 5%. Comparing to Fig. 3.6, the Ψ-scaling clearly leads to a reduction in spread of our measurements and a collapse of the model predictions for our sediments. The Ψ-scaled data reported by *Sessarego et al*. (2008b) and *Sessarego and Guillermin* (2012) fall below the other data sets. Comparing Fig. 3.7 to Fig. 3.1, the Ψ-scaling of their reported data leads to a reduction in spread but to an increased separation between their data and the rest of the literature measurements.

The spread among the sound speed measurements in Figs. 3.6 and 3.7 was computed as the difference between the maximum and minimum values within 0.15 wide ka intervals divided by the interval mean. The resulting values are shown in Fig. 3.8 and indicate that the Ψ-scaling significantly reduces the spread. Averaged over ka, the reduction is by nearly a factor of 2 – from 12.5% to 6.9% – if the *Sessarego et al*. (2008b) and *Sessarego and Guillermin* (2012) data are excluded.

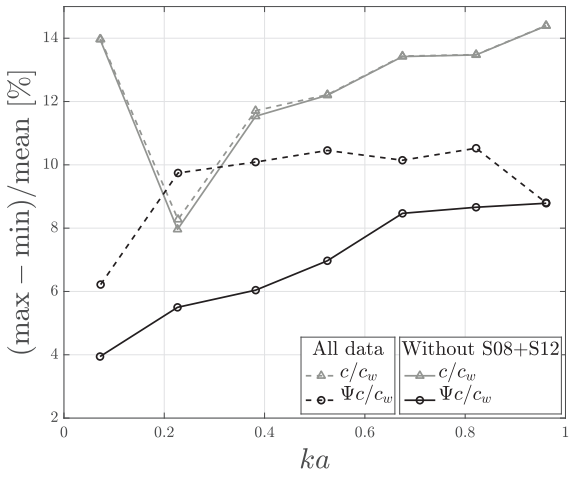

Figure 3.8: Spread among reported data and the present results for phase speed normalised by water sound speed, both with and without scaling by Ψ. Data reported by *Sessarego et al*. (2008b) and *Sessarego and Guillermin* (2012) were excluded for the solid lines.

Thomas and Pace (1980) measured phase speeds in five sand samples with porosities ranging from 0.35 to 0.55. Comparing Fig. 3.7 to Figs. 3.1 and 3.6, the collapse due to the Ψ-scaling is particularly evident for their data set (outlined in red). In fact, the spread – the difference between the maximum and minimum values divided by the mean – among their measurements is reduced from 13.5% to 1.4% by the Ψ-scaling. Given the wide range of porosities and despite the fact that the ka range of the measurements is below $ka = 0.25$ where (weak) positive dispersion is expected, the collapse of this data set is quite remarkable, confirming that most of the spread among the sound speeds can be attributed to differences in porosity and that the Ψ-scaling correctly accounts for n (to first order) at the long wavelengths. We return to the collapse of this data set below when discussing sediment compaction and the remaining spread among the Ψ-scaled speeds.

Scaling by Ψ is based on the assumptions that $K_s \gg K_w$, and that the tortuosity implemented in Eq. 3.2 is applicable to the types of granular media of interest here. To investigate the dependence on K_s, c^*_{LW} was computed using values between 3.8×10^{10} Pa to 4.7×10^{10} Pa for the bulk moduli of Ottawa sand and quartz sand reported by *Richardson et al*. (2002). Over this range of K_s, c^*_{LW} varies by only 0.8% for $n = 0.4$. The dependence of c^*_{LW} on tortuosity, ξ, was also investigated. The ξ-explicit form of effective density is given by (*Sen and Johnson*, 1983)

$$\rho_* = \rho_w \left[\frac{\xi(1-n)\rho_s + (\xi - 1)n\rho_w}{n(1-n)\rho_s + (\xi - 2n + n^2)\rho_w} \right]. \tag{3.8}$$

Eq. 3.8 reduces to Eq. 3.2 for $\xi = (3 - n)/2$, corresponding to $\xi = 1.29$ for $S1$, a value close to that of 1.33 obtained by *Reed et al*. (2010) for 364 μm sand using image analysis. Other reported values for sand are 1.49 (*Reed et al*., 2002) and 1.46 to 1.59 (*Delgado*, 2006). The literature has suggested several other relationships for the dependence of tortuosity on porosity, including $1-0.5 \ln n$ (*Weissberg*, 1963) and $n^{-1/2}$ *Sen et al*. (1981), which give values of 1.44 and 1.56 for $S1$, respectively. For $n = 0.4$, tortuosity ranges from 1.30 to 1.58 for the three different n dependencies listed above and ρ_* (Eq. 3.8) varies from 1686 kg/m^3 to 1740 kg/m^3 (for $\rho_s = 2650$ kg/m^3). For this range of tortuosiy and $K_s = 4.25 \times 10^{10}$ Pa, c^*_{LW} (Eq. 3.1) varies by 1.6%, which is lower than the spread among the reported sound speeds as well as the 5% difference between our unscaled measurements and model predictions.

The spread among the Ψ-scaled sound speeds is independent of transducer configuration relative to the sediment sample (Fig. 3.9a). In Fig. 3.9b, the Ψ-scaled sound speeds are plotted as a function of degassing procedure. Most studies report either boiling or holding their sediment samples under vacuum to remove air. Others agitated their sediment samples underwater to release trapped air by using a vibrator (*Park et al*., 2009), by pumping distilled water through their samples (*Argo IV et al*., 2011) or by repeated pourings underwater *Sessarego and Guillermin* (2012). Examining Fig. 3.9b, the degassing procedure (or lack of) cannot readily explain the spread among the Ψ-scaled sound speeds.

In Fig. 3.9c, the Ψ-scaled sound speeds are plotted as a function of sediment compaction method. For the present study, nothing was done to compact the granular material. *Argo IV et al*. (2011) used a fluidized bed set-up to control porosity, which was computed from the height of the fluidized column and the known mass of the sediment. Several studies used a vibrator to pack the sediment (*Thomas and Pace*, 1980; *Lee et al*., 2009; *Kimura*, 2011; *Yang et al*., 2018). Of these studies, only *Thomas and Pace* (1980) report that their porosity measurements were carried out on samples vibrated in the same way as those used for their acoustic trials. *Lee et al*. (2009) and *Kimura* (2011) do not specify and *Yang and Seong* (2018) (which provide details on the experimental method used for the *Yang et al*. (2018) dataset) suggest that the actual porosities of their vibrated sediment samples could be lower than those they measured for unpacked sediment. Examining Fig. 3.9c, most of the Ψ-scaled sound speeds for the compacted sediments are higher than those for which no compaction procedure was implemented.

Since Ψ is approximately linearly proportional to n over the range of interest, a lower (higher) porosity due to increased (decreased) compaction would lead to lower (higher) Ψ-scaled sound speeds and a better collapse of the data. For $\rho_s = 2650$ kg/m^3, Ψ would increase by 3.4% if the porosity increases from 0.4 to 0.45. To illustrate the sensitivity of the results to porosity, Fig. 3.10 shows sound speeds scaled by $\hat{\Psi}(\hat{n})$ where $\hat{n}$ is the adjusted porosity equal to $n - 0.02$ for the vibrated samples and $n + 0.02$ for the present results. For the *Thomas and Pace* (1980) data set, the porosity was not adjusted because their porosity measurements were carried out on samples treated in the same way as those used for their acoustic trials. Note that the standard deviation on our porosity measurements for replicate trials is slightly less than 0.01 and that the difference between the porosity measurement methods is 0.008 for $S1$ and 0.01 for G (see Sec. 3.3.1). Comparing Fig. 3.10 to Fig. 3.9c, these small changes in porosity can be seen to have substantially reduced the spread between our measurements and the reported sound speeds in vibrated sediments, thereby illustrating the (known) high sensitivity of sound speed to the value of porosity. Nevertheless, it is not obvious how the porosities in the actual sediment rings used for the present sound speed measurements could be systematically higher than those measured. In fact, it is the authors' view that the opposite is more likely to have been the case due to the sediment settling. Thus, differences in sediment porosity, possibly due in part to differences in compaction procedure, is a possible explanation for some and perhaps all of the remaining spread among the Ψ-scaled data.

3.6 Summary and Conclusions

The phase speed of compressional sound waves in water-saturated sand and glass beads was measured for $0.5 < ka < 1.2$. The sediment samples were boiled under pressure to remove air before transfer to the measurement tank. Sound speed was estimated from the travel time through different thicknesses of sediment using a pair of broadband transducers over a frequency range of 1.0 to 2.0 MHz, with the transmit transducer in the water and the receive transducer buried in the sediment. Negative dispersion was observed, consistent with previously reported measurements and the multiple scattering prediction of *Schwartz and Plona* (1984). Scaling the sound speed by a factor dependent on grain density and porosity reduces the spread among the measurements by nearly a factor of 2, from 12.5% down to 6.9%. It is suggested that the remaining spread among the scaled

sound speeds could be due to uncertainty in sediment porosity arising from the methods used to compact the sediments.

3.7 Acknowledgements

We thank Richard Cheel and Walter Judge for technical assistance. The literature data were extracted from published figures using Web Plot Digitizer (*Rohatgi*, 2015). This work was funded by the Natural Sciences and Engineering Research Council of Canada through an Alexander Graham Bell Canada Graduate Scholarship (CGS-D) to J. H. and a Discovery Grant to A. E. H.

3.8 Appendix: Reference Velocity

This section pertains to the values used for the reference velocity, c_0, in Eq. 3.4. This equation was obtained by *Kimura* (2014) from a best-fit regression to *Schwartz and Plona*'s EMA model prediction for sound speed in water-saturated glass beads normalised by the EMA-predicted long wavelength sound speed given in *Schwartz and Plona*, Table II, i.e. $c_0 = 1760$ m/s. Note that the measured long wavelength sound speed reported by *Schwartz and Plona* was different, i.e. 1790 m/s. *Kimura* (2011) compared measured phase speeds in water-saturated sediment to predictions from the Biot model modified to include gap stiffness (the BIMGS model) and to *Schwartz and Plona*'s multiple scattering model (Eq. 3.4). The difference between *Schwartz and Plona*'s predicted and observed long-wavelength phase speeds complicates the choice of reference velocity. *Kimura* (2011) overcame the difficulty by making his comparisons in dimensionless c/c_0 space. For his results, *Kimura* (2011) chose the velocities at $ka = 0.25$ computed from the BIMGS model for c_0. For values from the literature, *Kimura* (2011) chose c_0 to be the maximum observed value of the phase speed for each sample (*Kimura*, 2011, Fig. 10). The result of this transformation into non-dimensional c/c_0 vs ka space was to show that the transformed data exhibited a maximum at $ka \simeq 0.25$, with regions of negative (positive) dispersion at higher (lower) values of ka. However, *Kimura*'s method depended upon the observed sound speeds: (1) for *Kimura*'s own measurements, some of the BIMGS model parameters are obtained by fits to the measured sound speeds; (2) for the data obtained by others, *Kimura* normalized by the maximum measured value. In

contrast, c^*_{LW} depends only upon the density and sound speed in the fluid, the density of the sediment grains, and the porosity of the mixture, and is independent of the sound speed measurements themselves.

In Fig. 3.11a, the reported phase speeds from Fig. 3.1 are plotted as a function of ka with the data reported by *Argo IV et al*. (2011), *Kimura* (2011) and *Schwartz and Plona* (1984) in different colours. Also highlighted are the corresponding maximum phase speeds, c_{max}. These data sets were chosen because they exhibit either a clear maximum or a plateau at low ka: i.e., with $x = ka$, $\partial c/\partial x = 0$. In Fig. 3.11b, c_{max} is plotted as function of the value of ka at c_{max}. While most values of c_{max} occur below $ka = 0.25$, all are very close to $c_{0.25}$, the value of c at $ka = 0.25$, consistent with *Kimura* (2011)'s findings. In Fig. 3.11c, c_{max} and c^*_{LW} are compared, the latter computed using Eqs. 3.1, 3.2 and 3.3 with $K_s = 4.25 \times 10^{10}$ Pa. The ratio c_{max}/c^*_{LW} is within $\pm 2\%$ of unity, and exhibits no systematic dependence on ka, indicating that the use of c^*_{LW} does not introduce any additional dependence on ka. We conclude that, for the purposes of this study, the choice of c^*_{LW} for the reference velocity c_0 is both appropriate and has the advantages of being dependent upon readily-measured properties of the solid and fluid components of the granular medium as well as being independent of the measured sound speeds.

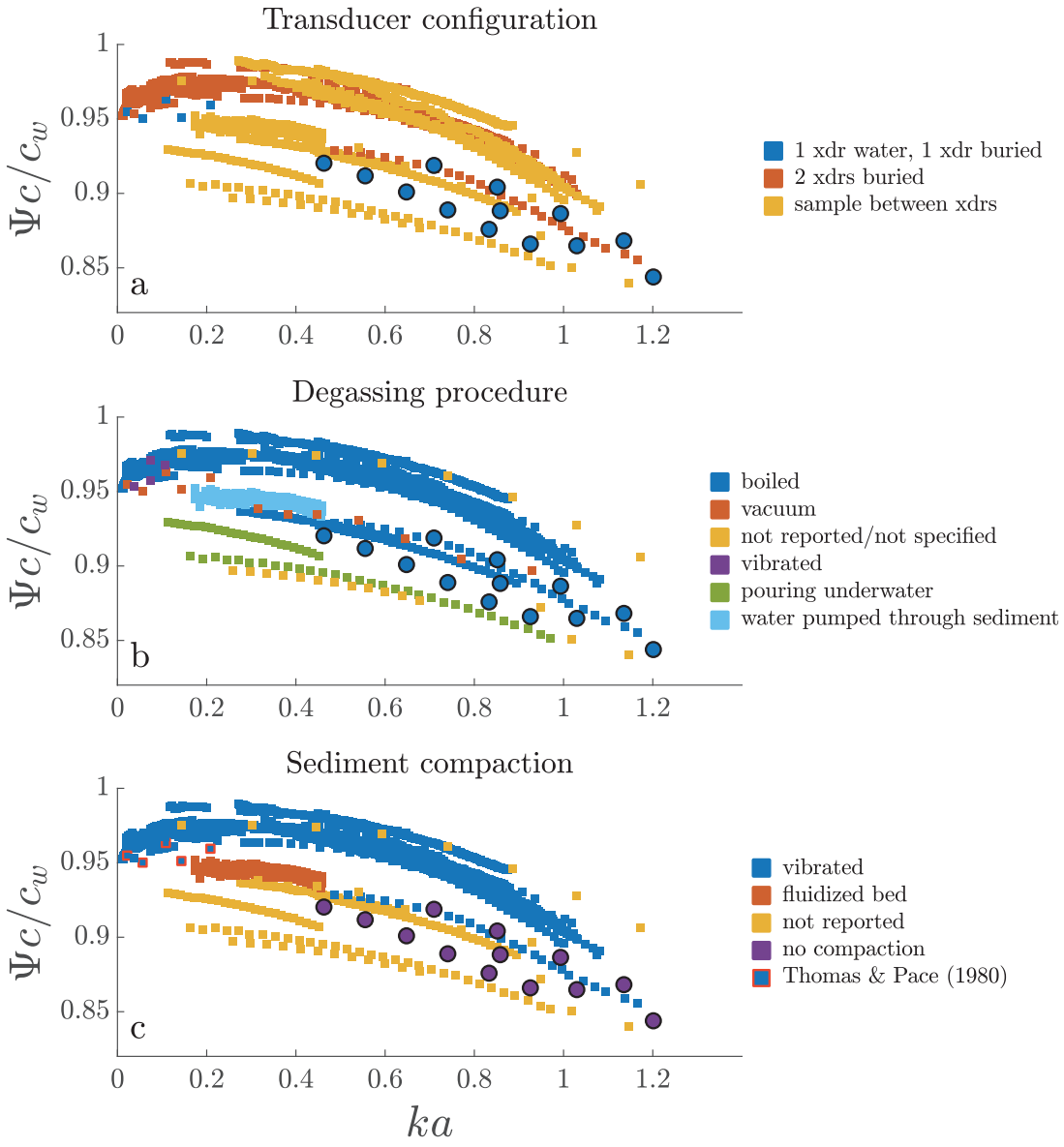

Figure 3.9: Ψ-scaled sound speed for reported data (squares) and the present results based on δh (circles). Symbol colour represents (a) transducer configuration, (b) degassing procedure and (c) sediment compaction method.

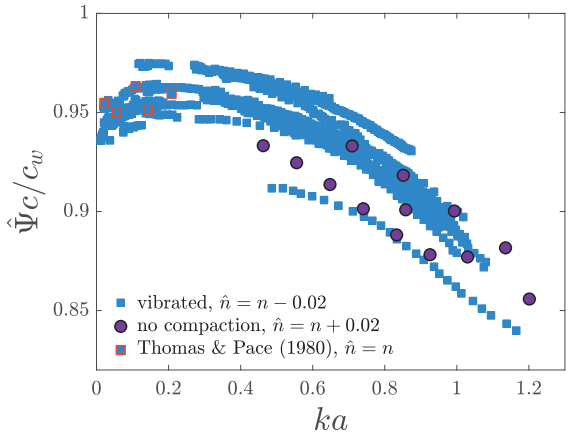

Figure 3.10: $\hat{\Psi}$-scaled sound speed for reported data which vibrated their sediment (blue squares) and the present results based on δh (circles) for which there was no compaction. In contrast to Fig. 3.9c, adjusted porosities, $\hat{n}$, have been used to compute $\hat{\Psi}$ except for the *Thomas and Pace* (1980) data, which are highlighted (see legend and also the text).

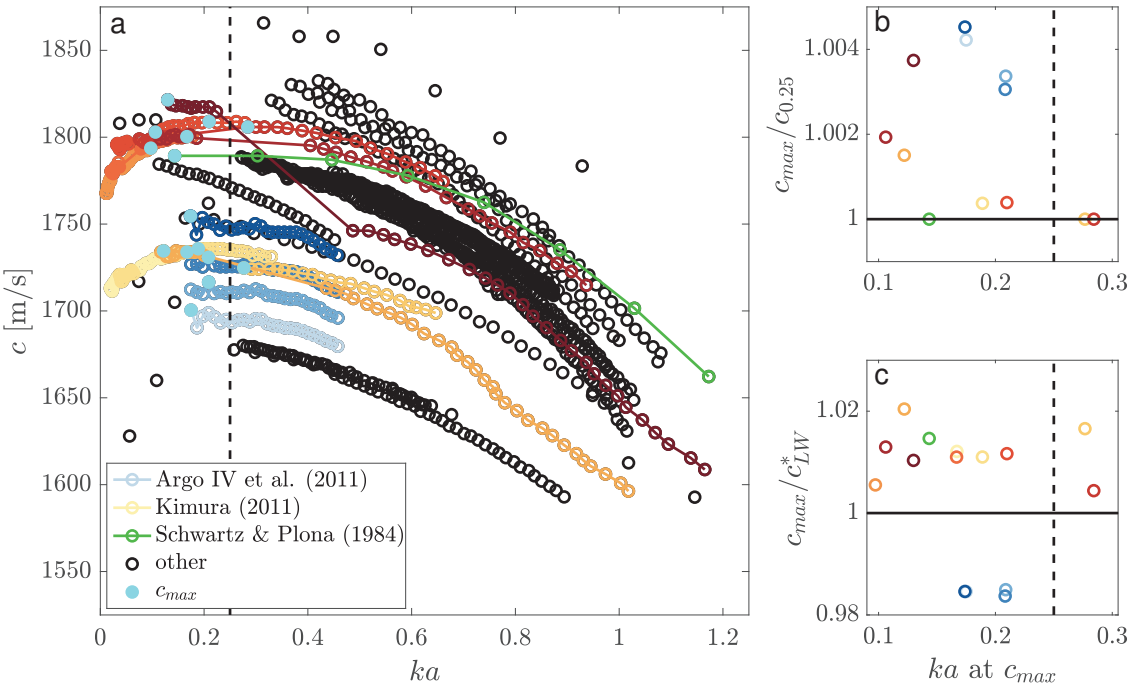

Figure 3.11: (a) Reported phase speed as function of ka with colour indicating data reported by *Schwartz and Plona* (1984) (green), *Argo IV et al.* (2011) (blues) and *Kimura* (2011) (yellows and reds). The maximum sound speeds for the coloured data are indicated. Ratio between the maximum phase speed and c at $ka = 0.25$ (b), and the long wavelength limit of phase speed (c), as a function of the value of ka at c_{max}. Note that the ratios are close to unity.

CHAPTER 4

ON ACOUSTIC REFLECTION FROM SAND-SIZED WATER-SATURATED GRANULAR MEDIA AT MHZ FREQUENCIES: MEASUREMENTS, MODELS AND THE ROLE OF SPECKLE

This chapter was first published in *The Journal of Acoustical Society of America*[1]

Abstract

Acoustic reflection coefficients are reported for water-saturated granular media at frequencies from 1.2 to 2.0 MHz using a narrow-beam broadband transducer in a monostatic geometry at near-normal incidence. Natural sand and glass beads with median grain diameters ranging from 0.22 mm to 0.40 mm were used. For each granular medium, bed elevation and rms roughness were measured using side-on photographs of the sediment-water interface. The probability density distributions of the bed elevations are Gaussian. The roughness parameter is close to 1, indicating that the reflected pressure field is mainly due to coherent scattering. The probability distribution of the observed reflection coefficients is nearly Gaussian, consistent with the predictions from a coherent single-scattering model. The horizontal decorrelation length of the observed reflection coefficients is ~ 4 mm, with no consistent dependence on either frequency or grain size, and approximately

[1]Reproduced from **Hare, J.**, and A. E. Hay, On acoustic reflection from sand-sized water-saturated granular media at MHz frequencies: Measurements, models and the role of speckle, *J. Acoust. Soc. Am.*, 148, 3291–3304, 2020b, with permission of AIP Publishing.

equal to 20% of the transducer diameter. This behaviour, which is reproduced by the single-scattering model, is due to speckle. The size/frequency-dependence of the reflection coefficients are well described by *Eckart* (1953)'s prediction for a rough surface with Gaussian-distributed surface elevations. Comparisons are made to previously reported reflection coefficient measurements.

4.1 Introduction

The reflection of sound by the seafloor is important for modelling sound propagation in shallow waters and within the seafloor as well as for inferring the geoacoustic properties of sediments (*Jackson and Richardson*, 2007). Previous research has mainly focused on the sub 300 kHz frequency range and comparisons to Biot theory. At higher frequencies (i.e. $ka > 0.25$, where k is the wavenumber in water and a is the grain radius), scattering becomes important. Multiple scattering models (*Waterman and Truell*, 1961; *Lloyd and Berry*, 1967; *Schwartz and Plona*, 1984) have been used to predict sound propagation and attenuation in low-concentration suspensions (*Hipp et al*., 1999; *Peters and Petit*, 2000) and in water-saturated sediments (*Kimura*, 2011; *Hare and Hay*, 2018; *Yang et al*., 2018).

Few measurements exist of the reflection coefficient from sand-sized water-saturated granular materials for ka values of order unity. *Nolle et al*. (1963) measured reflection losses of 11 dB from a sand-water interface for $0.12 < ka < 1.4$ and found no appreciable variation with frequency or grain size. More recently, *Le Gonidec and Gibert* (2007) observed an increase in reflection losses from ∼10 dB to ∼40 dB over $0.2 < ka < 10$ for water-saturated glass beads. Similarly, *Sessarego et al*. (2008a) and *Sessarego and Guillermin* (2012) measured the reflection loss from water-saturated sediment (glass beads and sand) and reported values increasing from 10 dB to 27 dB for $0.5 < ka < 3.5$. *Sessarego and Guillermin* (2012) concluded that for this ka range the sediment cannot be considered to be a continuous homogeneous medium, in contrast to the low ka case.

The purpose of this paper is to present laboratory measurements of the reflection coefficient at near-normal incidence for water-saturated granular materials. The measurements were made with a broadband narrow-beam transducer using short duration tone bursts with centre frequencies ranging from 1.2 to 2 MHz. Natural sand and glass beads with median grain diameters ranging from 0.22 mm to 0.4 mm were used, corresponding to $0.5 < ka < 1.7$. The results are compared to values previously reported in the

literature and to model predictions for smooth and rough surfaces, including a simplified single-scattering model, which successfully reproduces the observed reflection coefficient statistics and horizontal decorrelation lengths.

The paper is organized as follows. Theory and previous measurements are presented in Sec. 4.2. The experimental set-up and analysis methods are described in Sec. 4.3. The results from the measurements and the model are given in Secs. 4.4 and 4.5, respectively. These results are discussed in Sec. 4.6 and conclusions are given in Sec. 4.7.

4.2 Theory

Assuming plane wave propagation, the pressure reflection coefficient for normal incidence at a smooth boundary between two continuous homogeneous media is given by (*Clay and Medwin*, 1977)

$$R_0 = \frac{Z_2 - Z_1}{Z_2 + Z_1} \tag{4.1}$$

where the subscripts 1 and 2 denote the two media, $Z = \rho c$ is the acoustic impedance, ρ is the density and c is the sound speed. In the present case, medium 1 is water and medium 2 is a smooth reflector with the bulk properties of the reflecting medium.

For water-saturated granular media, sound speed varies with frequency and particle size. At the frequencies and particle sizes of interest here, multiple scattering theory predicts that the dispersion is negative (*Schwartz and Plona*, 1984), consistent with observations (*Schwartz and Plona*, 1984; *Kimura*, 2011; *Lee et al.*, 2007; *Hare and Hay*, 2018, 2020a). By applying a best-fit regression to the *Schwartz and Plona* results for water-saturated glass beads, *Kimura* (2014) obtained the following relation

$$\frac{c}{c_0} = 1 - 8.54 \times 10^{-3} (2ka)^{2.45} \tag{4.2}$$

where c_0 is a reference velocity. For the data of *Schwartz and Plona*, $c_0 = 1790$ m/s, their measured phase speed in the long wavelength limit. A question arises as to what value of c_0 to use in other cases.

Hare and Hay (2020a) chose the reference velocity to be

$$c^*_{LW} = \sqrt{K_*/\rho_*} \tag{4.3}$$

where K_* is the effective bulk modulus and ρ_* is the effective density. Eq. 4.3 is based on multiple scattering theory for a dense random packing of loose grains in an inviscid fluid at wavelengths long compared to the size of the scatterers (*Sen and Johnson*, 1983). For a composite medium comprised of water and sediment, K_* is given by

$$\frac{1}{K_*} = \frac{1-n}{K_s} + \frac{n}{K_w} \tag{4.4}$$

with n being the porosity and K_w and K_s the bulk moduli of water and sediment, respectively. For a tortuosity equal to $(3-n)/2$, ρ_* is given by

$$\rho_* = \rho_w \left[\frac{n\rho_w + (3-n)\rho_s}{(3-2n)\rho_w + 2n\rho_s} \right] \tag{4.5}$$

where ρ_w is the density of water and ρ_s is the sediment grain density (*Sen and Johnson*, 1983; see also *Williams*, 2001). With ρ_* in this form, Eq. 4.3 is non-dispersive. For $0.25 \lesssim ka \lesssim 1.5$, *Hare and Hay* (2020a) showed that, for a given grain size, density and porosity, the sound speeds estimated from Eq. 4.2 – using c^*_{LW} as the reference velocity – are accurate to within $\sim$5%. Note that this choice of reference velocity is independent of the observed sound speeds. For $ka \lesssim 0.1$, *Kimura* (2011) and others have demonstrated that measured phase speeds exhibit weak positive dispersion, consistent with several different implementations of the Biot model. Therefore, it is important to recognize that c^*_{LW} is a *reference velocity* and is not the actual long wavelength phase speed.

As frequency and grain size increase, the effects of surface roughness on the reflection coefficient must be considered (*Ogilvy*, 1991). For a rough surface with a Gaussian elevation distribution, *Eckart* (1953) showed that the coherent reflection coefficient at normal incidence is

$$R = R_0 e^{-\frac{g}{2}} \tag{4.6}$$

where g is the roughness parameter. *Eckart* (1953) obtained Eq. 4.6 by applying Kirchhoff theory to scattering of acoustic waves from the sea surface when roughened by surface waves. This theory has been applied to water-saturated sediments (*Thorne et al.*, 1988; *Chotiros*, 1994) with $g = (2k\sigma_\eta)^2$, where σ_η is the root-mean-square (rms) bed elevation. The reflection coefficient expressed in dB is referred to as the reflection loss, or bottom loss: $BL = 20\log_{10}|R|$.

Concerning the Kirchhoff approximation used in *Eckart*'s model, a criterion of applicability based on geometrical considerations – where the incident wavenumber is much larger than the curvature of the rough surface – may be used (*Beckmann and Spizzichino*, 1963). For normal incidence, this criterion is

$$2kr_c \gg 1 \tag{4.7}$$

where

$$r_c = \frac{L_\eta^2}{2\sigma_\eta} \tag{4.8}$$

is the local radius of curvature of the surface (*Pace et al*., 1985) and L_η is the surface correlation length. Eq. 4.7 has been shown to hold for backscattering from water-saturated gravel at 250 kHz and 1 MHz (*Pace et al*., 1985). Note that *Thorsos* (1988) concluded that the key parameter for determining the validity of the Kirchhoff approximation depends on L_η rather than r_c. However, for backscatter at near normal incidence, the approximation remains accurate (*Thorsos*, 1988; *Jackson and Richardson*, 2007).

For rough surfaces with large g, incoherent scattering becomes important (*Ogilvy*, 1991). *Thorne and Pace* (1984) present a rough surface reflection model, which includes both the coherent and incoherent contributions. For a monostatic geometry at normal incidence and using notation consistent with the present work, the prediction of *Thorne and Pace* (1984, Eq. 31) for the normalised scattering coefficient (proportional to the backscattered intensity) from a rough surface with Gaussian height distribution and Gaussian autocorrelation function is

$$S_c = R_0^2 e^{-g} + \frac{R_0^2 W^2}{8z_0^2}\frac{L_\eta^2}{\sigma_\eta^2}\mathbb{Z}(g) \tag{4.9}$$

where z_0 is the distance from source to the surface, $\mathbb{Z}(g) = ge^{-g}\sum_{m=1}^{\infty}\frac{g^m}{(sL_\eta^2+m)m!}$, $s = 0.5\left[W^{-2} + gW^2/(-2\sigma_\eta z_0)^2\right]$ and W is the radius of the insonified area on the surface determined for the point at which the transducer directivity falls to $1/e$ of its axial value. The first term in Eq. 4.9 represents the coherent intensity and is the square of the coherent reflection coefficient given by *Eckart* (Eq. 4.6), whereas the second term is the contribution from incoherent scattering. *Thorne and Pace* (1984) found good agreement between the model prediction and the measured reflection from a surface made of low density

polyurethane foam over a wide range of frequencies (corresponding to $0.1 < g < 500$). For $g < 1$, they found that the return signal was predominately coherent and that as g increased, the incoherent component became more important, consistent with Eq. 4.9.

4.3 Methods

4.3.1 Sand and glass beads

The sediment samples used in the present experiments are the same soda lime glass beads (G) and quartz sands ($S1$ and $S2$) as those used in *Hare and Hay* (2018, 2020a). Median grain size d_{50}, porosity n and grain density ρ_s are listed in Table 2.3. See *Hare and Hay* (2018) for details on how these grain parameters were measured as well as the grain size distributions.

4.3.2 Sediment-water interface roughness

Sediment was poured to a depth of $\sim$1 cm into a 5.9 cm long x 8.4 cm wide x 3.3 cm high clear-walled rectangular container. Water was added until there was a $\sim$1 cm deep layer over the sediment. For each granular medium, photographs of the sediment-water interface were taken through the container sidewall using a 5-Megapixel digital microscope (Celestron Handheld Digital Microscope Pro). The number of images taken were 13, 10 and 26 for $S1$, $S2$ and G, respectively. An example photograph of the interface for $S1$ sand is presented in Fig. 4.1, with x indicating the horizontal co-ordinate and z the vertical co-ordinate. The images were calibrated using a 2 mm x 2 mm printed square taped to the side of the container, visible in each image (not shown in Fig. 4.1).

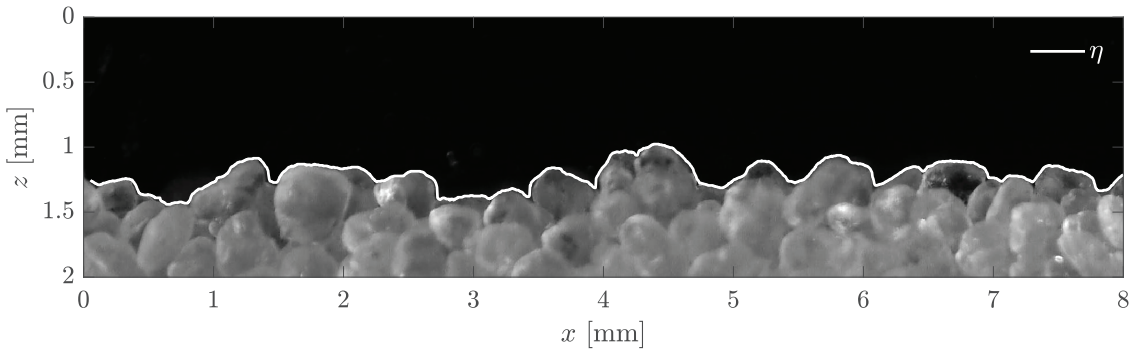

Figure 4.1: Photograph of $S1$ sediment taken through the clear sidewall of the rectangular sample container, showing the extracted sediment-water interface, η.

For each image, the sediment-water interface, $\eta(x)$, was obtained as follows. An approximate interface, η', was determined when the entropy (*Gonzalez et al.*, 2004) of each pixel exceeded a specified threshold. The entropy of all pixels was normalized by the average entropy along η' and a binary image was created, with normalized entropy above a specified threshold assigned a value of 1 and all others a value of 0. Isolated groups comprised of fewer than 300 equi-valued connected pixels were replaced with their binary opposite value. For the column of pixels corresponding to a given horizontal position in the image, the elevation of the sediment-water interface, η, was given by the uppermost non-zero pixel.

For each picture, η was divided into segments based upon visual inspection of the local trend. Segment lengths varied from 3 to 38 mean grain diameters with average values of 17, 12 and 10 diameters for $S1$, $S2$ and G, respectively. For each segment, the local trend was removed and used to compute the lagged autocorrelation function. The surface correlation length, L_η, was defined as the distance at which the autocorrelation function equalled e^{-1} of its value at zero lag (*Beckmann and Spizzichino*, 1963). The values of L_η reported here are the average of the values from all segments.

4.3.3 Experimental set-up

A wide-band circular transducer (Imasonic) was mounted at the top of a 46 (height) x 30 (side) cm polycarbonate rectangular apparatus, facing downward. Two sides of the apparatus were open to allow easy access to the sample volume inside. The whole assembly was placed in a 43 (width) x 90 (length) x 48 (height) cm rectangular glass-walled tank filled with distilled water.

A 20.3 (width) x 21.6 (length) x 2.52 (height) cm rectangular "tray" was placed on the bottom of the rectangular apparatus. The tray was a single piece of polyvinyl chloride (PVC) with a 1 cm deep, 17.3 cm wide by 18.5 cm long well milled out of its upper surface, leaving 1.5 cm wide containment walls of uniform height bounding the four sides of the uniformly deep well. Sediment was poured into the tray from containers fully immersed in the water-filled tank. To obtain a flat sediment-water interface, the excess granular material was scraped off by carefully drawing a squeegee – longer than the tray width, so that it rested on the sidewalls – across the tray. Nothing was done to compact the granular material. After completing measurements for a given sample, the tank was drained, cleaned and refilled with distilled water.

Measurements of the backscattered waveform were acquired using a digital oscilloscope sampling at 125 MHz. The 8 μs transmit pulse and analog electronics were similar to those used in *Hay et al*. (2012). Frequencies ranging from 1.2 to 2 MHz, separated by the 125 kHz bandwidth of the transmit pulse, were used. A 2.55 cm thick aluminum plate was used as a planar, smooth surface reflector to calibrate the backscatter amplitude from the sediment-water interface. Due to the high sound speed in aluminum, a 4 μs pulse length was used to avoid contamination of the surface return by the reflection from the bottom face of the plate.

Using the set-up described in *Wilson and Hay* (2017), the transducer beam pattern was measured by recording the backscatter from a 16 mm diameter tungsten carbide sphere at a range of 1.5 m and at different positions perpendicular to the beam axis, both vertically and horizontally. The measured beam pattern was fitted to the theoretical directivity for a circular piston transducer in the farfield: i.e., $D = 2J_1(ka_t \sin\beta)/(ka_t \sin\beta)$ (*Clay and Medwin*, 1977) with the transducer radius a_t used as the fitting parameter and where J_1 is the cylindrical Bessel function of the first kind and β the angle between the beam axis and the target. The best fit value of a_t was 1.1 cm, consistent with the 2.2 cm transducer diameter specified by the manufacturer. The computed transducer beam pattern properties, i.e. the polar angle to the half-power point β_0, to the peak of the first sidelobe β_s and the polar angle β_e for which $D^2 = e^{-1}$, are listed in Table 4.1. Also listed are the ranges to the farfield $R_c = \pi a_t^2/\lambda$ and to the last axial pressure maximum $R_c' = a_t^2/\lambda$, where λ is the acoustic wavelength (*Zemanek*, 1971; *Clay and Medwin*, 1977). In the present work, the vertical distance between the transducer and the sediment-water interface was 40.7 cm. Thus, the reflection measurements were made in the far-field for 1.2 MHz and 1.4 MHz and beyond the last pressure maximum for the higher frequencies.

Table 4.1: Transducer beam pattern properties computed using a water sound speed of 1480 m/s and $a_t = 0.011$ m.

f [MHz]	R_c' [cm]	R_c [cm]	β_0 [°]	β_e [°]	β_s [°]
1.2	9.8	30.8	1.7	2.0	5.3
1.4	11.4	36.0	1.4	1.7	4.5
1.6	13.1	41.1	1.2	1.5	3.9
1.8	14.7	46.2	1.1	1.3	3.5
2.0	16.3	51.4	1.0	1.2	3.2

4.3.4 Reflection coefficient measurement procedure

In order to avoid having air bubbles trapped within the sediment, the samples were boiled before transferring them to the measurement tank as follows. Dry sediment was poured into a 1.1 L cylindrical aluminum chamber and filled with distilled water, leaving a 250 mL air gap. After boiling for 30 seconds, the chamber was sealed off and allowed to cool to room temperature. The chamber was then placed in the water-filled measurement tank and opened underwater. The sediment sample was transferred to small containers that were kept underwater for the duration of the experiment. This procedure was repeated until there was enough sediment, typically 0.5 to 1 L. Then, the rectangular tray was filled with sediment underwater as described in Sec. 4.3.3.

Acoustic data were collected at each tray position, which was moved carefully by 2 cm increments – about 1 transducer diameter – in both along- and across-tray horizontal directions. After each set of measurements, the sediment was removed from the tray (underwater), poured back in and then the procedure was repeated. The total number of positions, N, recorded for each granular medium and transmit frequency is given in Table 4.2.

Table 4.2: Number of tray positions, N, for each granular medium and transmit frequency.

Granular media	1.2 [MHz]	1.4 [MHz]	1.6 [MHz]	1.8 [MHz]	2.0 [MHz]
S1[1]	0	0	310	0	0
S1	16	16	16	16	16
S2	108	107	51	50	47
G	18	18	18	18	18

For each frequency and tray position, the received signals from 10 transmit pulses were ensemble-averaged. Example signals, $V(t)$, from the aluminum plate and from $S1$ sand are shown in Fig. 4.2, with the interface return $V_I(t)$ highlighted. Noise level, N_s, was defined as the rms value of the signal prior to $V_I(t)$. $V_I(t)$ was defined to start at the first amplitude value larger than three times the noise level and to end one pulse length later. The rms value of $V_I(t)$, designated by A, is used throughout the remainder of the paper as the measure of the amplitude of the backscatter from the interface. The signal-to-noise ratio (SNR) is the ratio A/N_s.

The ratio of the amplitudes from the sediment-water and aluminum-water interfaces

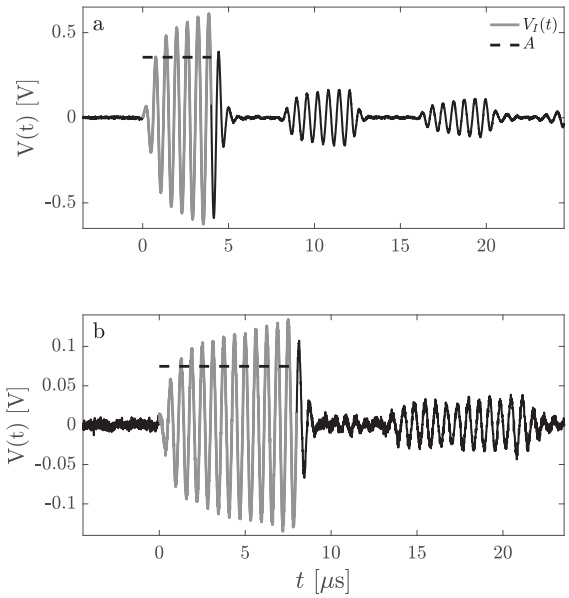

Figure 4.2: Backscatter amplitude (black) from a single trial at 1.6 MHz for (a) the aluminum plate and (b) $S1$ sand. The returns from the sediment-water and aluminum-water interfaces, $V_I(t)$, are indicated in grey, with their respective rms amplitudes indicated by the dashed lines. Note the presence of successive reflections from the back face of the aluminum plate in (a) and from the base of the sediment tray in (b).

yields the reflection coefficient

$$R = \frac{A}{A_{\text{ref}}} R_{\text{ref}} \tag{4.10}$$

where A_{ref} and R_{ref} are the backscatter amplitude and reflection coefficient from the aluminum plate, R_{ref} being estimated using Eq. 4.1 with a density of 2700 kg/m^3 (*Kreith and Goswami*, 2004). The sound speed in the aluminum was estimated from the time delay between successive reflections from the back of the aluminum plate given by the time difference between the first peak and the second and third peaks of the Hilbert transform of the cross-correlation. These time differences, together with the appropriate multiple of the plate thickness (2 or 4) were used to compute sound speed in the aluminum plate. The average of these two values ranged between 6422 to 6468 m/s. The average over all trials was 6444 $\pm$ 11 m/s, close to the handbook value of 6420 m/s for aluminum (*Rossing*, 2007). In addition, the water sound speed c_w was computed using the MATLAB Gibbs Seawater Oceanographic Toolbox using the International Thermodynamic Equation Of Seawater (*IOC et al.*, 2010) and using the measured water temperature. The temperature of the water was measured each day experimental trials were executed and ranged from

20.3°C to 22.0°C.

4.3.5 Integral length scale procedure

A modified version of the experimental set-up described in Sec. 4.3.3 was used to investigate the dependence of backscatter amplitude on horizontal position. In this set-up, the transducer mount was modified so as to enable horizontal translation of the transducer parallel to the sediment tray. In addition, the sides of the rectangular apparatus were lengthened, increasing the distance between the transducer and the bottom to 68 cm, which permitted reflection measurements to be made in the farfield at all frequencies. As before, the entire apparatus was submerged in a larger glass-walled tank, but filled in this case with tap water. The measurements were made over a 4 day period, starting 13 days after filling the tank. For these trials, air was removed from dry sediment samples under vacuum. The sediment-filled aluminum chamber was held at 91 kPa below atmospheric pressure for 1 to 2 min. The sealed chamber was then transferred to the measurement tank, where it was opened underwater in the same way as before.

Sediment was poured into the tray, which was placed on the bottom of the rectangular apparatus, and the excess sediment was scraped off (see Sec. 4.3.3). Using the same transmit frequencies and pulse lengths as those given in Sec. 4.3.3, backscatter amplitude was recorded at 30 positions of the transducer separated by 0.16 cm horizontally. For each position and frequency, the received signals from 10 transmit pulses were ensemble-averaged. The signal reflected from the sediment-water interface, $V_I(t)$, and its rms value, A, were determined in the same manner as described in Sec 4.3.4. Accounting for two-way travel, the time at which the interface return started was converted to a distance to the interface, z_0, using the water sound speed, c_w. Two and three repeat trials were executed for sediments $S1$ and $S2$, respectively. The procedure was repeated for the aluminum plate placed on the bottom of the rectangular apparatus. The measured water temperature varied from 19.9°C to 20.4°C for this set of measurements.

4.4 Results: Measurements

4.4.1 Surface roughness

The probability density distribution functions (PDFs) of bed elevation normalized by its standard deviation, $p(\eta/\sigma_\eta)$, are plotted in Fig. 4.3 and compared to Gaussian distributions with a variance of unity. The observed distributions are well-represented by the Gaussian PDF. Listed in Table 4.3 are standard deviations σ_η, surface correlation lengths L_η and radii of curvature r_c. For all three granular media, the surface correlation length and radius of curvature were one to two times the mean grain radius. The normalised roughness σ_η/a was 0.75, 0.56 and 0.43 for S1, S2 and G, respectively. The values of σ_η/a are larger for the sands than the glass beads, consistent with the glass beads being smoother than the sand grains. (For comparison, *Pace et al*. (1985) and *Thorne et al*. (1988) obtained values of σ_η/a between 0.34 and 0.44 for surfaces comprised of natural gravel which, on the basis of Fig. 3 in *Pace et al*. (1985), appear to have been very smooth.) For 1.2 to 2 MHz and the measured parameters listed in Table 4.3, $2kr_c$ (Eq. 4.7) varied between 1.8 and 5.3.

Table 4.3: Surface roughness parameters.

Sediment	σ_η [μm]	L_η [μm]	r_c [μm]	σ_η/a	L_η/a	r_c/a
$S1$	82.2	178	193	0.75	1.6	1.8
$S2$	115	269	315	0.56	1.3	1.6
G	71.5	160	180	0.43	0.96	1.1

For the measured sediment parameters and frequencies used in the present work, the roughness parameter g varies from 0.5 to 3.8. Since $g \sim 1$, these sediment surfaces are moderately rough (*Ogilvy*, 1991). For these values of g, the ratio of the incoherent scattering term to the coherent term in Eq. 4.9 varies from 0.04% to 3.1%. Thus, the contribution to the reflected amplitude from incoherent scattering is expected to be small, indicating that the measured reflection coefficients should be consistent with the *Eckart* formula (Eq. 4.6).

4.4.2 Reflection coefficient measurements

Fig. 4.4 shows the probability distribution of the reflection coefficient, normalized by its standard deviation, for $S1$ sand at 1.6 MHz. The distribution is symmetric about the

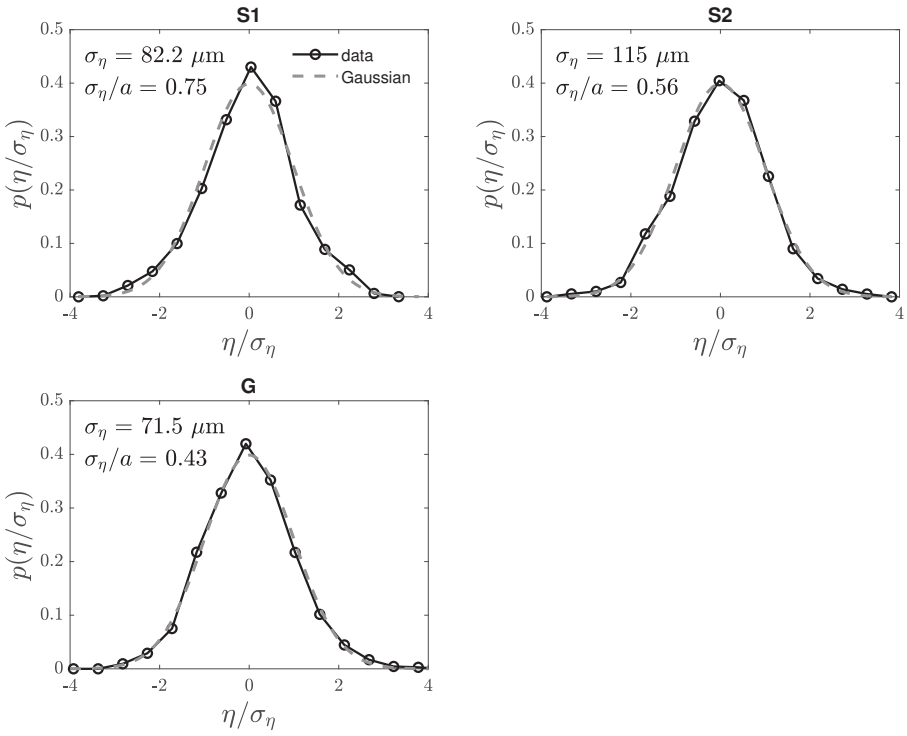

Figure 4.3: Probability density distributions of elevation, η, normalized by the standard deviation, σ_η, for each granular medium type and size. The dashed lines are Gaussian distributions with the same standard deviation.

median value, with a skewness of -0.2 and a kurtosis of 2.7, only slightly different from the expected values of 0 and 3 for a Gaussian-distributed random variable. The distribution is very different from the Rayleigh distribution, a point which is discussed later.

The mean signal-to-noise ratio, SNR, is plotted in Fig. 4.5 as a function of frequency for each of the three granular materials. The variation in SNR for $S1$ reflects the bandwidth of the transducers. SNR decreases with increasing grain size, especially evident at the higher frequencies. As will be seen, the reflection coefficient decreases with increasing particle size and acoustic frequency. Note that all values of SNR are well above unity.

In Fig. 4.6, reflection coefficients averaged over all tray positions are plotted as a function of ka and compared to values from the literature. Similar to the present experiments, the reported values represent averages over many positions of a horizontally-translated sediment tray. *Sessarego et al*. (2008a) and *Sessarego and Guillermin* (2012) averaged 50 return signals for a tray 25 cm below the transducer, whereas *Le Gonidec and Gibert* (2007) averaged 30 returns from a tray 60 cm away. The transmit frequencies spanned

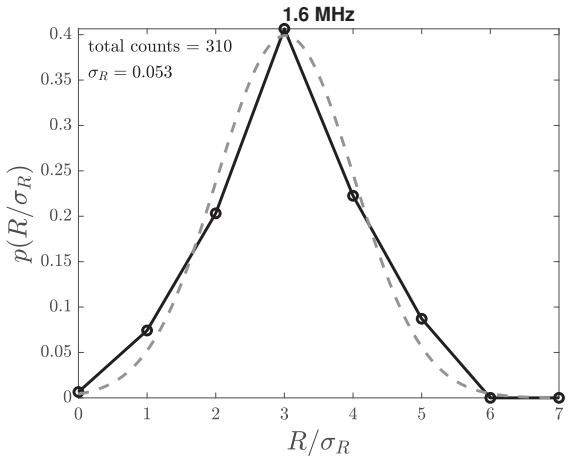

Figure 4.4: Probability distribution of the measured reflection coefficient for $S1$ sand at 1.6 MHz normalized by its standard deviation. The dashed line is a Gaussian distribution with the same mean and standard deviation.

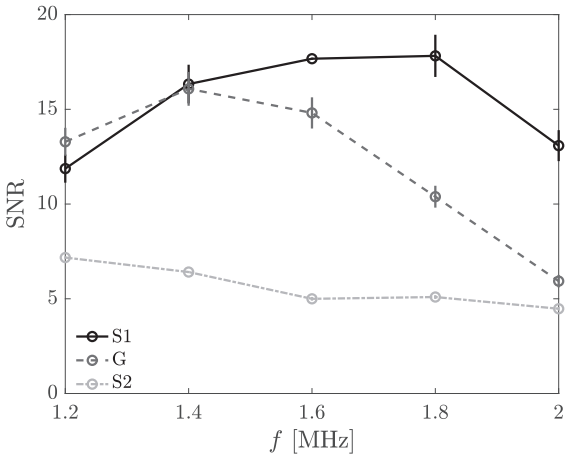

Figure 4.5: Mean signal-to-noise ratio as a function of frequency for each granular medium. Vertical bars denote ± 1 standard error from the mean.

by the literature data are 200 kHz to 1 MHz (*Le Gonidec and Gibert*, 2007), 200 kHz to 7 MHz (*Sessarego et al*., 2008a) and 200 kHz to 1.5 MHz (*Sessarego and Guillermin*, 2012). Only data for which $0.15 \leq ka \leq 2$ are plotted in Fig. 4.6. The predicted reflection coefficients for smooth (Eq. 4.1) and rough (Eq. 4.6) surfaces were determined using *Schwartz and Plona*'s multiple scattering theory for sound speed (Eq. 4.2 with c_0 equal to c^*_{LW} given by Eq. 4.3), Eq. 4.5 for the effective density, and the measured sediment properties listed in Table 2.3 with $K_s = 4.25 \times 10^{10}$ Pa, the average of the measured values reported by *Richardson et al*. (2002) for sand. For the smooth surface curves, the ka-dependence is due solely to the negative dispersion predicted by *Schwartz and Plona*'s multiple scattering theory. In contrast, the rough surface curves are different for each grain size, illustrating the important influence of the roughness parameter on R.

At long wavelengths, the present results tend toward the smooth surface prediction and to the 11 dB reflection loss measurement for sand measured by *Nolle et al*. (1963) at 500 kHz and 1 MHz and by *Chotiros et al*. (2002) for 8-17 kHz. At larger ka, both the present and the literature estimates decrease more rapidly with increasing ka than the smooth surface prediction and follow more closely the ka-dependence of the rough surface prediction. The present estimates of R for the glass beads are larger than those for sand, also consistent with the rough surface prediction. However, the predictions from the rough surface theory tend to be lower than the measured values for $S1$ and higher for $S2$ and G.

4.4.3 Spatial variation in the reflection coefficient

As described in Sec. 4.3.5, measurements were made at different horizontal positions by translating the transducer. Let x be the horizontal position of the transducer, and $z_0(x)$ be the distance to the sediment-water interface measured at 1.6 MHz at location x. The detrended distances to the interface, $z_0'(x)$, for the aluminum plate, $S1$, and $S2$ are plotted in Fig. 4.7abc. The $z_0'(x)$ profiles are all comparably flat, each with a standard deviation of ~ 30 μm. The corresponding horizontal profiles of detrended $A(x)$ are presented in Fig. 4.7def. The $A(x)$ profiles for both sand sizes exhibit pronounced oscillatory variations with $\sim$2 to 3 cm nominal wavelengths. Despite the fact that the $z_0'(x)$ profile for aluminum is comparably flat to those for sand, the $A(x)$ profiles for aluminum do not exhibit any sinusoidal variation, particularly not at $\sim$2 to 3 cm length scales. Thus, the

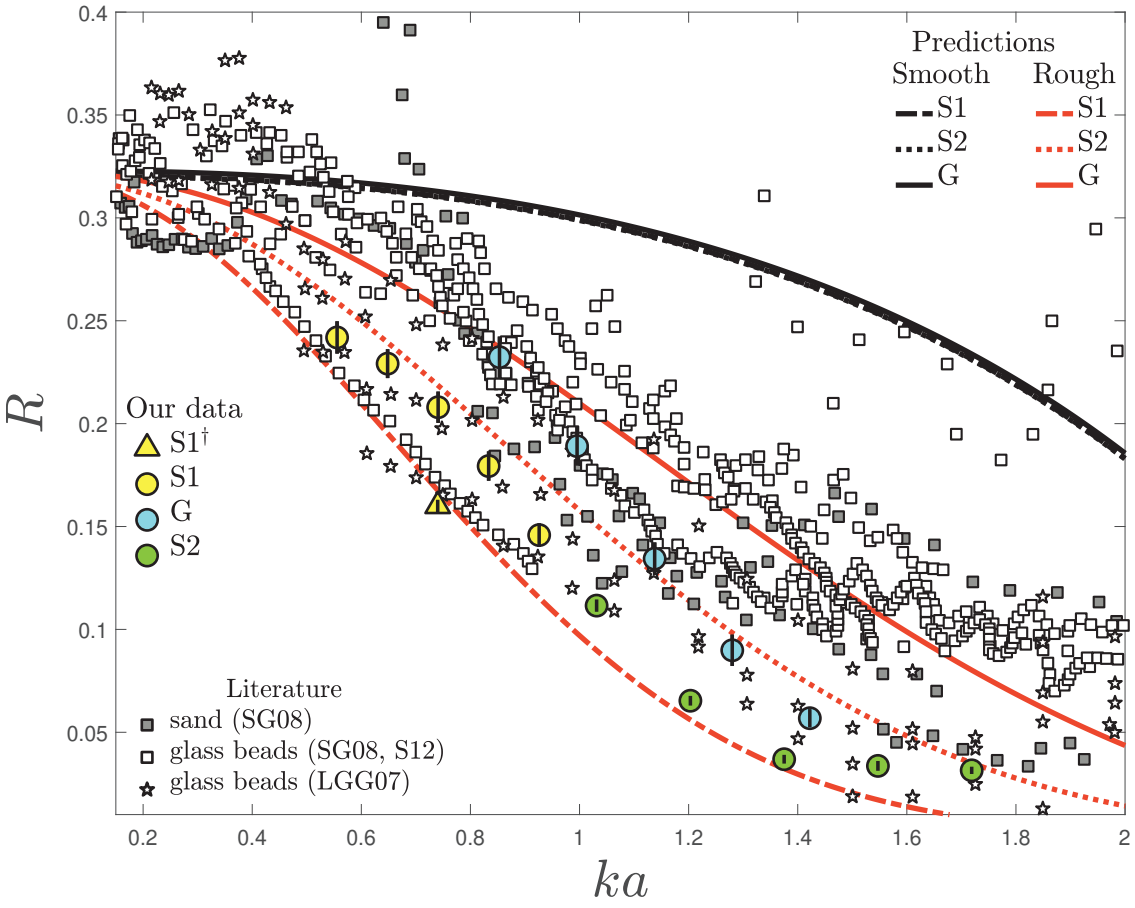

Figure 4.6: Reflection coefficient as a function of ka. Previously reported measurements (*Le Gonidec and Gibert*, 2007; *Sessarego et al.*, 2008a; *Sessarego and Guillermin*, 2012) are indicated by gray shaded squares for sand and open squares and pentagrams for glass beads. Values from the present work are indicated by the coloured symbols. The point identified by † indicates that only 1.6 MHz frequency data were collected. Vertical black lines indicate ± 1 standard error from the mean. The black curves are the predictions for a smooth surface using Eqs. 4.1, 4.2 and 4.5 and the measured sediment properties. The red curves are the predictions for a rough surface using Eq. 4.6 and the measured values of σ_η.

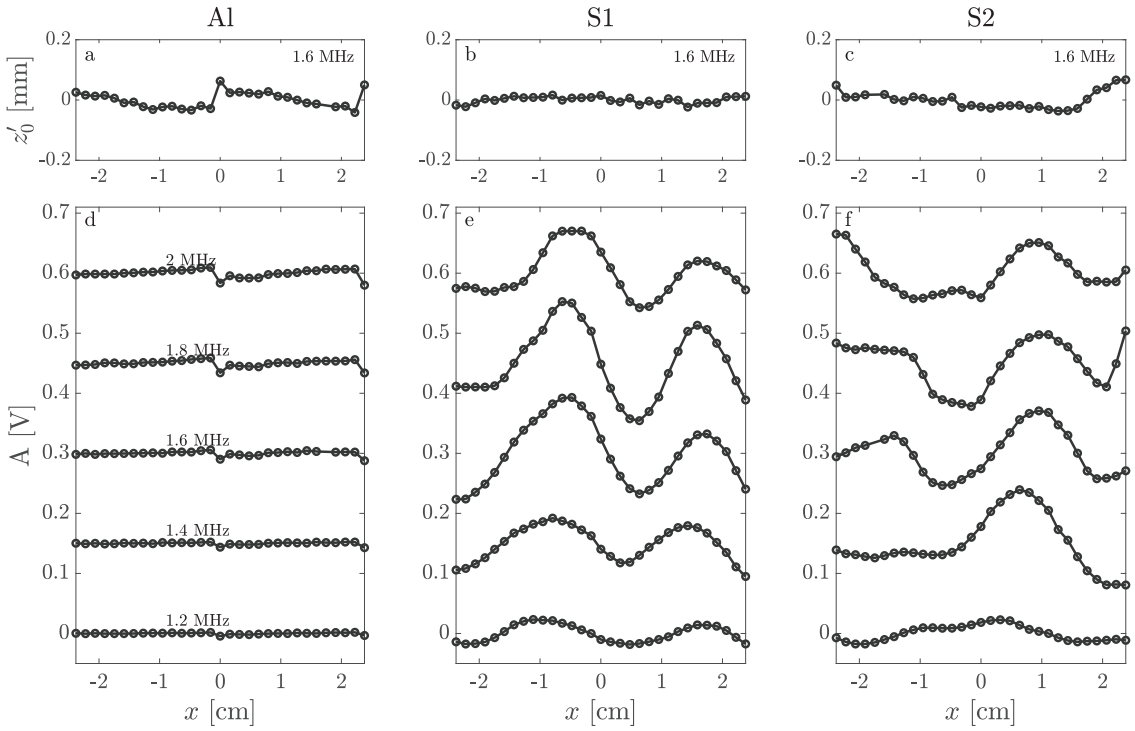

Figure 4.7: Detrended vertical distance from the transducer to the reflecting surface as a function of horizontal position: (a) the aluminum plate; (b) $S1$ and (c) $S2$. (d-f) Examples of the detrended backscatter amplitude as a function of horizontal position at the transmit frequencies (offset in the vertical) for the aluminum plate and the two sand sizes, $S1$ and $S2$.

roughly sinusoidal variations in the $A(x)$ profiles for the granular surfaces are not associated with sinusoidal changes in elevation in the sediment-water interface: i.e., there are no sinusoidal variations in $z_0'(x)$ with $\sim$2 to 3 cm wavelengths. Similar sinusoidal variations were observed in all sediment repeat trials (not shown). Note that there is a dip in the amplitude of the reflection from the aluminum plate at $x = 0$, likely due to the inhomogeneity observed at the same location in the z_0' profile. This inhomogeneity was observed at the same x location in the aluminum-water interface profiles for all frequencies (not shown).

For each frequency and sediment trial, the lagged auto-correlation function for $A(x)$, C_{AA}, was computed. Let the decorrelation length be the lag at which $C_{AA} = e^{-1}$ and the integral length scale be the first maximum of the integral of C_{AA} with respect to x. Average decorrelation lengths, x_d, and integral length scales, Λ, for $S1$ and $S2$ are listed in Table 4.4, where the averages were computed over frequency and repeat trials.

The values for both sand sizes are comparable. No consistent variation with respect to frequency was found for either parameter.

Table 4.4: Decorrelation length, x_d, and integral length scale, Λ, for $S1$ and $S2$ sands, respectively. The errors are ± 1 standard deviation.

	$S1$		$S2$	
	x_d [mm]	Λ [mm]	x_d [mm]	Λ [mm]
Measured	4.5 ± 0.3	3.8 ± 0.3	4.9 ± 1.0	4.0 ± 0.8
1D	4.3 ± 0.6	3.5 ± 0.5	4.7 ± 0.5	3.8 ± 0.4
quasi-2D	4.5 ± 0.6	3.7 ± 0.5	4.5 ± 0.5	3.7 ± 0.4

4.5 Results: Model

4.5.1 Model formulation

A reflection model based on single-scattering from discrete particles was constructed to investigate the reflection coefficient statistics and the decorrelation length. Both one- and two-dimensional versions of the model were developed. A simulated grain supply was created by interpolating the measured grain size distribution (based on mass) to 1 μm increments and then converting to a number distribution assuming spherical particles. Particles were selected at random, with replacement, from this grain supply and placed on the x-axis sequentially, such that the centres of adjacent particles are separated by the sum of their respective radii (Fig. 4.8). The length of the resulting linear array of particles was 20 cm. Shadowing by nearest neighbour particles is not taken into account in the model. The particles were then displaced vertically by $\Delta z_j = \epsilon d_{50} \chi_j$, where χ_j is drawn from a Gaussian distribution and ϵ was chosen so as to yield a modelled roughness parameter $\hat{\sigma}_\eta$ close to the measured values listed in Table 4.3. As shown in Fig. 4.9, the PDFs of the modelled bed elevations for the three granular media are Gaussian. The 1D model was extended to a quasi-2D version by stacking 221 realisations of the 1D model in y, forming a 2D array of particles. The distance between the rows was set to the maximum grain diameter. The model assumes continuous wave transmission, which is appropriate in the context of the present work because the effective acoustic footprint on the surface is determined entirely by the transducer beam pattern: i.e., the finite (8 μs) duration of the

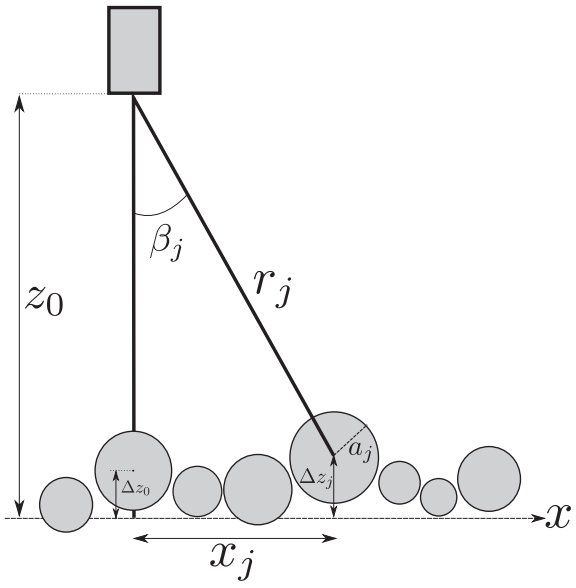

Figure 4.8: Definition sketch for the 1-dimensional single-scattering reflection model.

transmit pulse does not limit the size of the footprint.

In the 1D model, the backscattered pressure from the jth particle is given by

$$\hat{p}_j = p_* r_* \sqrt{\sigma_j} \frac{D_j^2}{r_j^2} e^{i\phi_j} \tag{4.11}$$

where p_* is a reference pressure, r_* is a reference distance, σ_j is the backscatter cross-section for the jth particle and $D_j(\beta_j)$ is the transducer directivity. The phase difference between the ray path to particle a_j and that to the particle at the origin is $\phi_j = 2k(r_j - (z_0 - \Delta z_0))$, where $r_j = \sqrt{(z_0 - \Delta z_j)^2 + x_j^2}$ (Fig. 4.8). In the quasi-2D model case, r_{ij} and β_{ij} are the range and angle from the transducer centre to the ith particle in the jth row and are a function of both x_{ij} and y_{ij}. For both cases, the complex amplitudes arriving from particles within the transducer's frequency-dependent circular footprint were summed to give the total complex pressure amplitude $P = \sum_{j=1}^{N_p} p_j$, where N_p is the number of particles in the transducer footprint $2z_0 \tan \beta_m$ with $\beta_m = 2\beta_0$ (Table 4.1). In addition, $p_* r_* \sqrt{\sigma_j}$ is set to unity: i.e. the scattering cross-section is the same for all particles.

4.5.2 Predicted amplitude and phase statistics

The probability distributions of amplitude and phase obtained from 300 realisations of the 1D model are presented in Fig. 4.10. Both distributions are comparable to Gaussians, consistent with the nearly Gaussian behaviour of the measured reflection coefficients (Fig.

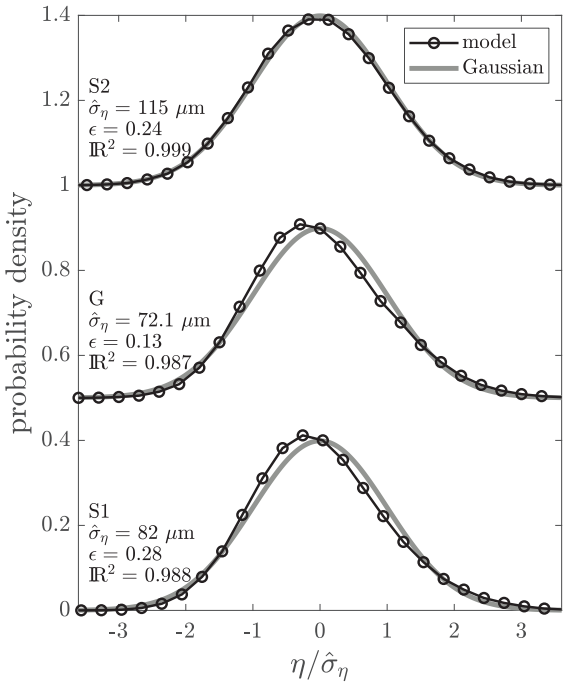

Figure 4.9: Probability density distribution of modelled grain elevations for 100 realisations. For each granular medium, a Gaussian distribution with same mean and standard deviation is also shown. The distributions for G and $S2$ are offset in the vertical by 0.5 and 1 respectively. The coefficients of determination, $\mathbb{R}^2$, between the probability density distribution and the Gaussian are listed.

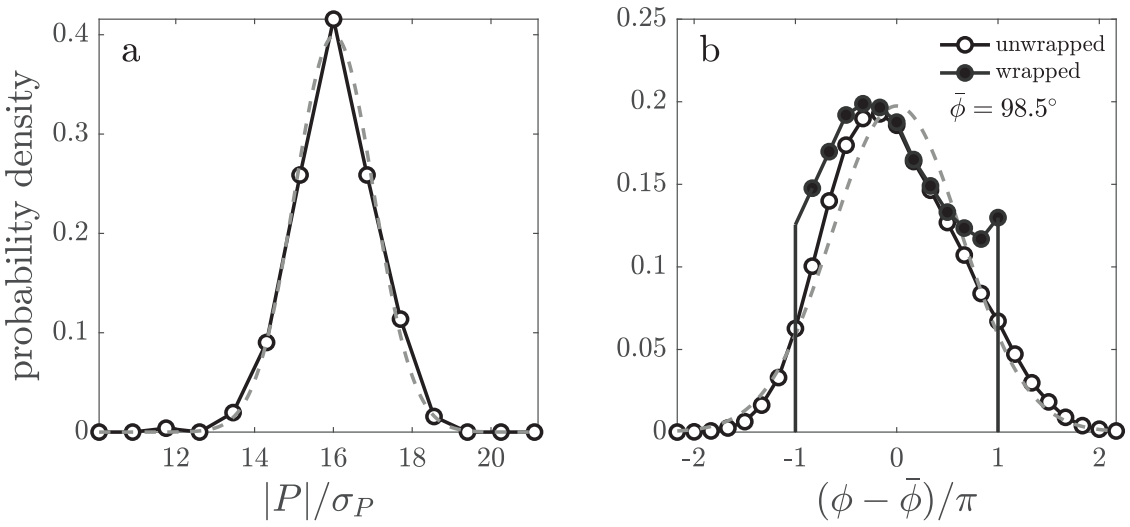

Figure 4.10: Probability distributions of the (a) amplitude and (b) phase predicted by the 1D model for $S1$ sand at 1.6 MHz and $z_0 = 41$ cm (solid lines). In (b), the distributions for unwrapped phases and wrapped phases to $\pm\pi$ are given by the empty and filled circles, respectively. Gaussian distributions with the same means and standard deviations as the predictions are shown (dashed lines).

4.4). The same approximately Gaussian behaviour was observed for the quasi-2D model. This departure from Rayleigh statistics occurs because, for a given wavelength and particle size, the range of possible phase differences is constrained by the particle spacing (horizontal and vertical) and the transducer beamwidth so that the phases are not uniformly distributed on the interval $\pm\pi$. In the quasi-2D model, the amplitude distribution tends towards a Rayleigh distribution if the beamwidth is increased and 90% or more of the particles within the transducer footprint are removed.

4.5.3 Predicted spatial variation in the reflected amplitude

To investigate the spatial variation in the reflected amplitude, the virtual transducer was displaced horizontally by the same increment as that used for the measurements, i.e. 0.16 cm. The model-predicted detrended backscatter amplitudes for $S1$ and $S2$ as a function of transducer position are shown in Fig. 4.11 for a single realization of the quasi-2D model with $z_0 = 65$ cm. The spatial structure of the predicted amplitudes is comparable to that exhibited by the measurements (Fig. 4.7). The lagged auto-correlation function was computed for the 20 cm long profile in 5 cm detrended segments with 1 cm overlap. The integral length scale and the decorrelation length were ensemble-averaged over all 5 cm segments. The decorrelation length and integral length scale averaged over 10 realisations

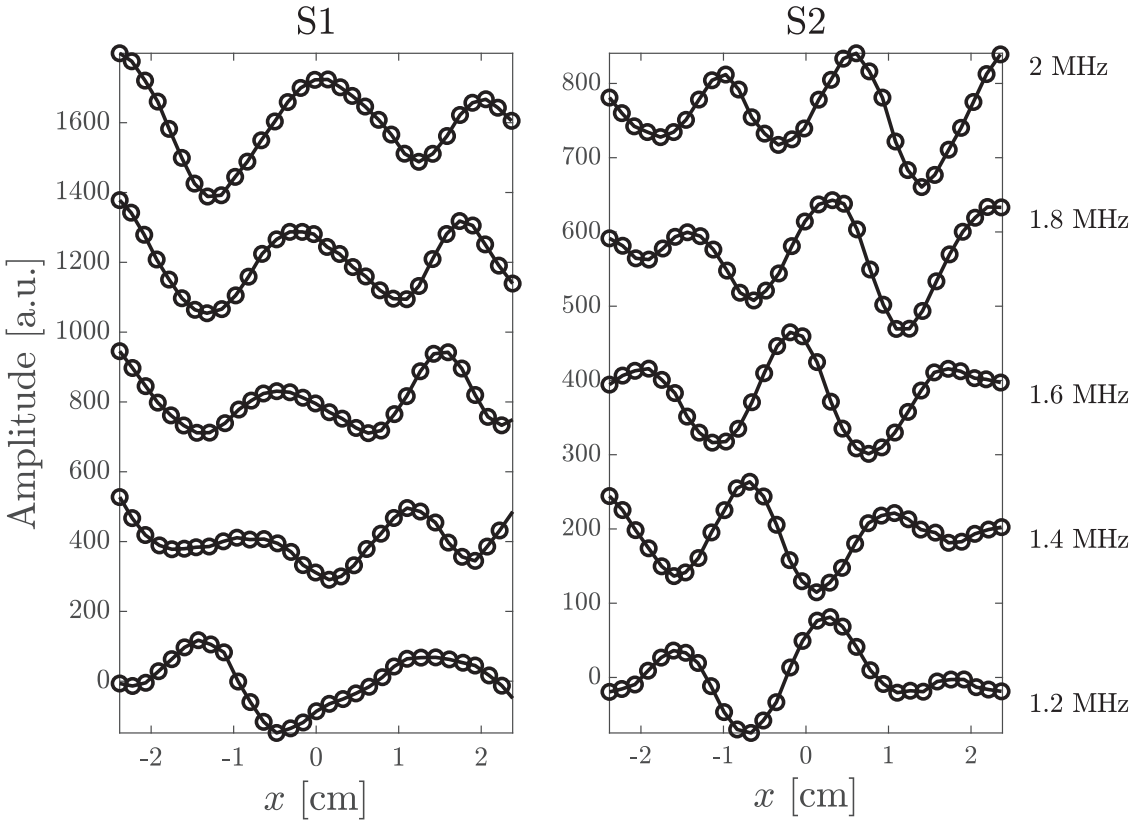

Figure 4.11: Examples of the detrended backscatter amplitude (arbitrary units) as a function of position x and frequency (offset in the vertical) predicted by the quasi-2D model for the two sand sizes, $S1$ and $S2$, $z_0 = 65$ cm and $\beta_m = 2\beta_0$.

and all 5 frequencies are listed in Table 4.4. The values from both the 1D and quasi-2D models are comparable to each other and to the measurements and, like the measurements, no consistent frequency-dependence was found for either parameter. Similar results were obtained for $z_0 = 41$ cm.

For the quasi-2D model, varying the spacing between rows from half to twice the maximum grain diameter did not significantly affect x_d or Λ. In addition, no significant difference was found for random perturbations of the y coordinate of each particle by $\Delta y_{ij} = \epsilon_y d_{50} \chi_{ij}$, where χ_{ij} is drawn from a Gaussian distribution, for $0 \leq \epsilon_y \leq 1$.

The dependence of $A(x)$ on β_m was investigated. Model-predicted detrended $A(x)$ profiles for a range of values of β_m are shown in Fig. 4.12. In this case, the quasi-2D model was constructed by stacking 451 realisations of the 1D model so as to accommodate the larger transducer footprint for the larger β_m values. As β_m increases, the spatial pattern becomes smoother due to an increase in the range of relative phases. Most of the

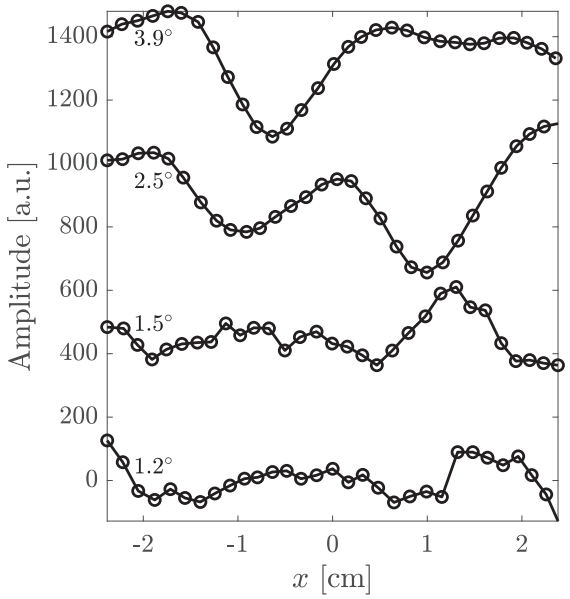

Figure 4.12: Predicted backscatter amplitudes from the quasi-2D model as a function of horizontal position for $S1$ sand at 1.6 MHz and for $z_0 = 65$ cm. The different curves – which are detrended and offset in the vertical – are from the same model realization for the indicated values of β_m: i.e. β_0, β_e, $2\beta_0$ and β_s.

main lobe of the directivity pattern is contained within $\pm 2\beta_0$ and, in this case, 85% of the maximum energy – i.e. $\int 2\pi x D^2 dx$ – is contained within the footprint. For these values of β_m, no significant difference was found for either x_d or Λ averaged over 5 realisations. Comparable results were obtained for the 1D model.

The frequency-dependence of the amplitude of the spatial structure was investigated. One of the $S1$ measurement trials (Fig. 4.7e) exhibited a decrease in variance (normalised by the square of the mean return from the aluminum plate) by a factor of 3 from 1.2 MHz to 2.0 MHz. In contrast, the other four measurement trials exhibited no discernible frequency dependence. For the quasi-2D model, the mean variance of the amplitude over all 5 cm detrended segments from 10 trials decreases by a factor of two from 1.2 MHz to 2.0 MHz for both sand sizes. However, the standard deviations are large, ranging from 67% to 89% of the mean. This variability is attributed to differences in particle arrangement and is a possible explanation for the differences observed between the two $S1$ measurement trials.

4.6 Discussion

4.6.1 Spatial variation in the reflected amplitude: speckle

The agreement between the observed and predicted spatial patterns in the reflected amplitude is confirmation that the pattern is a consequence of the interference among the waves scattered from the sediment-water interface, and also consistent with the coherent scattering being the dominant contributor to the backscattered amplitude in the observed range of ka. Known as speckle, this phenomenon has been extensively studied using laser light (*Goodman*, 1976). Acoustic speckle (*Abbott and Thurstone*, 1979) has been of interest in the medical field with the focus being on reducing speckle in ultrasound imaging (*Burckhardt*, 1978). For lateral translations of a linear phased array over two rough surfaces (a contrast-detailed phantom and a fine-grained sponge), *Trahey et al*. (1986) found that decorrelation occurred at translations of about 40% of the aperture length, independent of frequency or reflecting material.

Consistent with the measurements of *Trahey et al*. (1986), the observed and predicted decorrelation lengths here are frequency-independent and independent of the rough surface material. The decorrelation length divided by the transducer diameter is about 0.2 for the present observations and model predictions, which is shorter than those measured by *Trahey et al*. (1986). However, their measurements were based on volume scattering at low scatterer concentrations and therefore Rayleigh-distributed amplitude statistics in contrast to the Gaussian statistics applicable to the present results.

The agreement between the present observed and the model-predicted decorrelation lengths indicates that the horizontal separation between measurement positions must be at least 0.2 transducer diameters in order to be independent. This criterion is more than satisfied by the present reflection coefficient measurements, which were made approximately one transducer diameter apart. The separation to transducer diameter ratio ranged from 0.12 to 0.39 for the data of *Sessarego et al*. (2008a) and 0.17 to 0.2 for *Sessarego and Guillermin* (2012). *Le Gonidec and Gibert* (2007) did not report their transducer size.

4.6.2 Mean value of the reflection coefficient

The probability distribution of the reflection coefficient is Gaussian, as indicated by the observations and substantiated by the model. This fact allows us to estimate the 95% confidence interval for the observed mean value R, given the number of independent

measurements and the standard deviation (*Montgomery and Runger*, 2010). Our best estimate of the standard deviation is that for $S1$ at 1.6 MHz: 0.053. There is 95% confidence that the error in the mean is 3.7% for $N = 310$ compared to 7.2% for $N = 16$ (Table 4.2).

Calibrating the return signal using a smooth planar surface compared to a standard spherical target can introduce a bias due to the frequency-dependence of the beamwidth (in other words, the size of the footprint reflecting from a smooth surface). In Sec. 4.9, an expression for the frequency-dependent beamwidth correction factor, γ_B, is derived. As noted in Sec. 4.9, γ_B varies from 1.05 to 1.12 for the frequencies and range used for the present work (Fig. 4.15). *Sessarego and Guillermin* (2012) used the air-water interface to calibrate their measurements. Based on their reported transducer diameters and ranges, γ_B would have ranged from 1.01 to 1.40, with a mean of 1.1. Beamwidth-corrected reflection coefficients, $\hat{R} = R/\gamma_B$, are presented in Fig. 4.13 and can be compared to the uncorrected values in Fig. 4.6. The colours in Fig. 4.13 indicate the effective density, ρ_*, computed using Eq. 4.5. Only the data of *Sessarego and Guillermin* (2012) are shown in Fig. 4.13 because *Le Gonidec and Gibert* (2007) did not report their transducer diameter or sediment density and *Sessarego et al*. (2008a) did not report sediment density or porosity. For *Sessarego and Guillermin* (2012), ρ_* was computed using their reported porosities and wet densities to estimate ρ_s. Fig. 4.13 indicates that some of the spread among the data points can be ascribed to differences in the effective density of the water-saturated sediment. The dependence on other bulk parameters such as ρ_s (not shown) and n (Fig. 4.14) were investigated, but a clear separation in the data was indicated only for ρ_*.

4.6.3 Applicability of the *Eckart* model

In Sec. 4.4, $2kr_c$ was found to vary between 1.8 and 5.3, which is larger than 1. Given that the probability density distributions of the grain elevations are comparable to Gaussian curves and that the Kirchhoff approximation (Eq. 4.7) is valid for the frequencies of interest, *Eckart*'s equation for the rough surface reflection coefficient (Eq. 4.6) should apply. Although the estimated values of $2kr_c$ are not much much larger than 1, especially at the lower frequencies, *Beckmann and Spizzichino* (1963) do state that natural surfaces tend not to contain many sharp edges compared to human-made objects and so the $2kr_c \gg 1$ criterion can be "more forgiving". The results presented here tend to indicate that this is the case for at least some surfaces comprised of sand-sized granular material, including

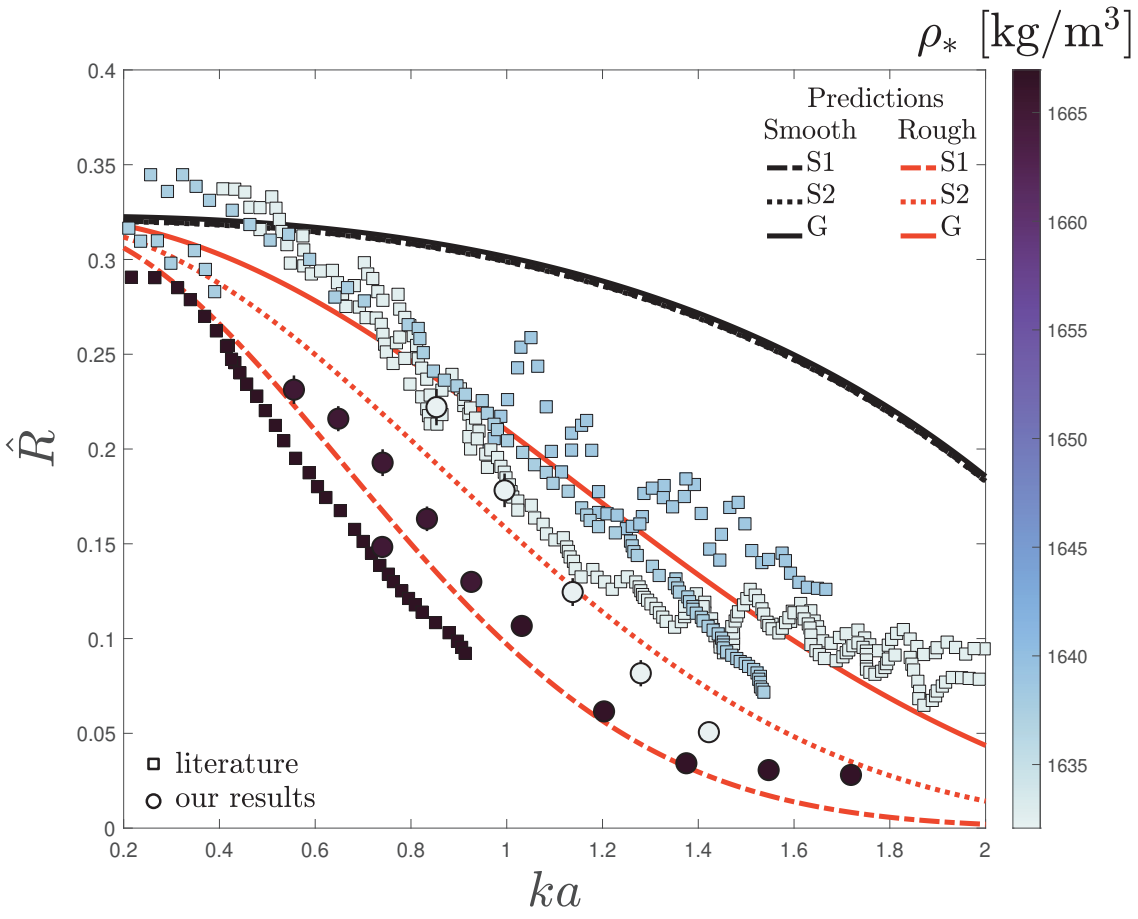

Figure 4.13: Beamwidth-corrected reflection coefficients for saturated water-particle mixtures as a function of ka, where squares and circles are estimates from *Sessarego and Guillermin* (2012) and the present work, respectively. The marker colour indicates the calculated ρ_* (Eq. 4.5). See also caption for Fig. 4.6.

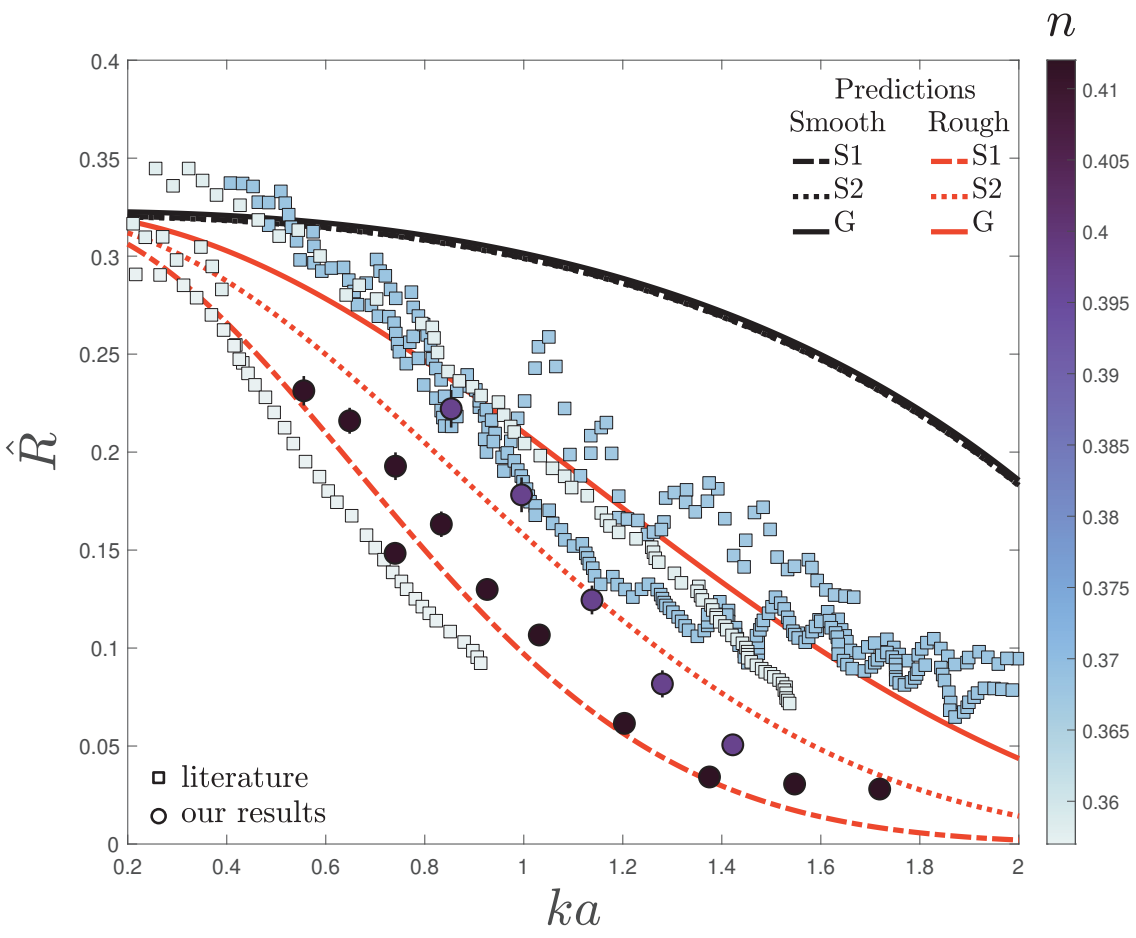

Figure 4.14: Beamwidth-corrected reflection coefficients for saturated water-particle mixtures as a function of ka, where squares and circles are estimates from *Sessarego and Guillermin* (2012) and the present work, respectively. The marker colour indicates the sediment porosity. See also caption for Fig. 4.6.

the two natural sands used here.

As shown by the results in Fig. 4.6, the *Eckart* model accounts for much of the observed size/frequency-dependence of the reflection coefficient in this range of ka. There remains, however, considerable spread among the available measurements plotted in Fig. 4.6, some of which might be due to experimental error, and some to the fact that the surface roughness was not measured in the previously-reported experiments. However, as shown in Fig. 4.13, it appears that some of the spread can be attributed to differences in the effective density of the bulk material.

Eckart (1953)'s prediction for the reflection from a rough surface has previously been applied to sound scattering from rippled sandy bottoms with $\sigma_\eta = 7.7$ mm (value extrapolated from *Chotiros* (2002, Fig.5)) and from flat sandy bottoms with $\sigma_\eta = 5.6$ mm (*Isakson et al*., 2012). *Chotiros* (2002) obtained agreement with *Eckart*'s prediction for frequencies between 10 and 15 kHz (corresponding to $0.4 < g < 0.9$). At higher frequencies, *Eckart*'s model under-predicted the reflection coefficient due to the reflected energy being mainly incoherent. *Isakson et al*. (2012) found that *Eckart*'s model over-predicted the reflection losses by more than 10 dB at near-normal angles for $0.05 < g < 14$, explained by the roughness power spectrum being non-Gaussian. To the authors' knowledge, the *Eckart* model has not been previously applied to reflection at normal incidence from sand-sized granular sediments at wavelengths comparable to the grain size.

4.7 Summary and Conclusions

The reflection of sound from water-saturated sand and glass beads was investigated for $0.5 < ka < 1.7$ using a narrow-beam broadband transducer in a monostatic geometry. Backscattered amplitude was calibrated using the reflection from an aluminum plate. For each granular medium, the roughness of the sediment-water interface was measured by photographing the interface through the sidewall of a transparent rectangular container. The probability density distributions of the surface elevations were Gaussian. Higher roughnesses were obtained for sand compared to the glass beads, consistent with the glass beads being smoother than the two natural sands used in the experiments, and indicating that roughness cannot be estimated from grain size alone. Roughness parameters were close to 1, signifying that – for the granular materials and sizes investigated here – the

sediment-water interface can be considered a moderately rough surface at MHz frequencies. For these values, incoherent scattering is relatively weak at near-normal incidence and the total reflection coefficient reduces to *Eckart*'s prediction for coherent reflection.

The probability distributions of the observed reflection coefficient are nearly Gaussian. This result is reproduced using a 1D single-scattering model, demonstrating that the relative phases of the waves backscattered from different points on the surface are not uniformly distributed between $\pm\pi$, and thus explaining the departure from Rayleigh statistics. The observed backscatter amplitudes exhibited pronounced oscillatory variations as the transducer was translated horizontally. The associated decorrelation length scales are about 4 mm and independent of grain size or acoustic frequency (at least within the error bounds of the measurements). This behaviour is a consequence of speckle in the reflected amplitude field and is replicated both qualitatively and quantitatively by a quasi-2D version of the single-scattering model. The ratio between the decorrelation length and the transducer diameter was 0.2, shorter than values reported in the medical ultrasound literature, which were based on volume scattering and Rayleigh statistics, but consistent with this literature in the sense of being independent of frequency.

The size/frequency-dependence of the present measurements and those previously reported in the literature are well-represented by *Eckart* (1953)'s prediction for a rough boundary. There remains, however, considerable spread among the data. Differences in effective density may contribute to some of this spread.

4.8 Acknowledgements

We thank Richard Cheel and Walter Judge for technical assistance. The literature data were extracted from published figures using Web Plot Digitizer (*Rohatgi*, 2015). This work was funded by the Natural Sciences and Engineering Research Council of Canada through an Alexander Graham Bell Canada Graduate Scholarship (CGS-D) to J. H. and a Discovery Grant to A. E. H.

4.9 Appendix: Beamwidth Correction

In this section, an expression for a frequency-dependent beamwidth correction factor is derived. Let the smooth surface be in the xy plane, centred at $x = 0$ and at a distance

z_0 away from the transducer. The smooth surface reflection case is equivalent to a virtual source placed at $z = -z_0$ (mirror image). Dropping time dependence and water attenuation, the reflected signal at the transducer is

$$p_b = R\frac{p_* r_*}{r} D(\beta) e^{ikr} \tag{4.12}$$

where r_* is a reference distance, p_* is a reference pressure and $D(\beta) = 2J_1(ka_t \sin\beta)/(ka_t \sin\beta)$ is the directivity for a circular transducer with radius a_t (*Clay and Medwin*, 1977). β and $r = \sqrt{4z_0^2 + w^2}$ are the angle and distance from the surface to the transducer with w being the radial distance along the transducer face. The total force on the transducer face is

$$F = 2\pi \int_0^{a_t} \xi p_b w dw \tag{4.13}$$

where $\xi = 1 - (r - 2z_0)/c_w\tau$ is a fractional pulse overlap function and τ is the pulse length. Note that $\xi = 1$ for normal incidence, i.e. $r = 2z_0$, and $\xi = 0$ for $r = c_w\tau + 2z_0$. Substituting Eq. 4.12 into Eq. 4.13,

$$F = \pi R\frac{p_* r_*}{z_0} \Gamma_B \tag{4.14}$$

where

$$\Gamma_B = \int_0^{a_t} \xi D e^{ikr} \frac{w}{\sqrt{1 + w^2/4z_0^2}} dw. \tag{4.15}$$

Since the intensity is proportional to the square of the force, the ratio between the intensity of a surface in the distant farfield z_∞ to that at z_0 is

$$\frac{I(z_\infty)}{I(z_0)} = \frac{z_0^2}{{z_\infty}^2} \gamma_B^2 \tag{4.16}$$

where γ_B is

$$\gamma_B = \frac{|\Gamma_B(z_\infty)|}{|\Gamma_B(z_0)|}. \tag{4.17}$$

To correct pressure (or voltage) measurements made at $z_0 < z_\infty$, Eq. 4.16 can be rearranged to

$$V(z_\infty) = \frac{z_0}{z_\infty} \gamma_B V(z_0). \tag{4.18}$$

The z_0/z_∞ factor corrects for spherical spreading and γ_B is the frequency-dependent

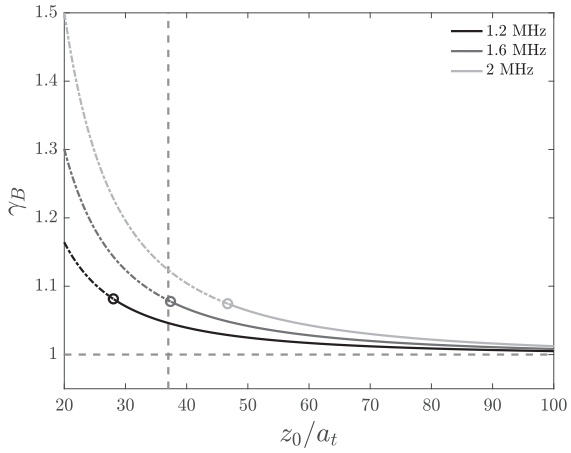

Figure 4.15: Beamwidth correction factor as a function of frequency and distance from the transducer to the smooth surface, z_0, normalised by the transducer radius, a_t. The circles indicate R_c (Table 4.1) and the vertical dashed grey line is $z_0 = 40.7$ cm.

beam correction factor.

Fig. 4.15 shows the beamwidth correction factor computed for the transmit properties used for the aluminum plate measurements, that is a 4 μs transmit pulse with frequencies ranging from 1.2 MHz to 2 MHz, using the farfield directivity. At large values of z_0/a_t, γ_B tends to unity for all frequencies. For the present measurements, which were made at $z_0 = 40.7$ cm, γ_B varies from 1.05 to 1.12.

CHAPTER 5

VELOCITY STRUCTURE AND EFFECTIVE VISCOSITY IN SUB-AQUEOUS GRANULAR FLOW DOWN A SLOPE: FIXED BOTTOM ROUGHNESS

Abstract

Measurements of the vertical structure of sub-aqueous gravity-driven granular flow down an incline are reported for the fixed bed roughness case. The sediments – either 0.336 mm diameter glass beads or 0.406 mm diameter natural sand – were released from a cofferdam, producing a layer with a thickness of O(1) cm moving at O(10) cm/s. The velocity profile within the moving layer was measured using a wide-band pulse-coherent Doppler profiler (MFDop) operating at 1.2 MHz. Velocity measurements were also made with side-view and top-view video cameras using particle imaging velocimetry (PIV), and with a 10 MHz commercially available Doppler profiler (Vectrino). The Vectrino and top-view PIV measurements are comparable to those from the MFDop, but are confined to the upper part of the flow. The estimates from the side-view camera are much lower due to sidewall friction. The observed velocity profile exhibits a mid-layer maximum, bounded above and below by zones of negative and positive shear rate, immediately below the sediment-water interface and immediately above the bed, respectively. Good agreement is obtained between the observed velocity profile and that predicted from an analytic low Reynolds number viscous fluid model. The agreement is better for glass beads ($\mathbf{R}^2 =$

0.94) than sand ($\mathbf{R}^2 = 83$). Porosity and effective viscosity within the moving layer are estimated from the model fits using *Bagnold* (1954)'s semi-empirical relation for the effective viscosity for the macro-viscous regime.

5.1 Introduction

In the ocean, sediment transport impacts beach morphology, benthic ecology, coastal infrastructure and pollutant transport. These processes occur over a wide range of temporal and spatial scales. Of particular interest is bedload transport, the part of the total sediment load that is mostly in continuous contact with the bed (*Fredsoe and Deigaard*, 1992). Bedload can be driven by shear stress (*Ribberink and Al-Salem*, 1995; *Houssais et al.*, 2015), pressure (*Flores and Sleath*, 1998) or gravity (*Cassar et al.*, 2005). The movement of granular material exerts a controlling influence on the nearbed flow, turbulence and stress and the feedbacks between these processes are still not well understood. Thus, bedload prediction remains a challenge (*Houssais et al.*, 2015; *Ancey*, 2020a) and experimental research is needed to understand these complex relationships (*van Rijn et al.*, 2013). In addition, studying the grain-scale physics that regulate granular flows are important for a wide range of disparate fields (*Mehta et al.*, 2009), including geophysics (e.g. snow avalanches, debris flows, sediment transport in rivers) and industrial processes (e.g. size segregation in granular mixtures (*Shinbrot and Muzzio*, 2000))

Measuring bedload transport at high spatial and temporal resolution is challenging. Direct sampling methods are typically made using sediment traps, which provide only time-integrated measurements and thus give no information on short time and small spatial scales (*White*, 1998). Laboratory measurements of the velocity profile within a moving layer of granular material have been obtained using particle tracking velocimetry (PTV) in a rotating drum (*Jain et al.*, 2004) and using particle image velocimetry (PIV) in a tiltable Hele-Shaw cell (*Doppler et al.*, 2007). However, these types of side-on video-imaging techniques can be affected by friction from tank sidewalls. Others have measured velocity and concentration profiles in shear-induced flows in a rectangular (*Aussillous et al.*, 2013) or annular (*Houssais et al.*, 2015) channel by recording the laser-excited fluorescence of a dye dispersed in the fluid containing index-matched particles, which allowed images to be made in the centre of the channel, beyond the influence of sidewall friction. This method is not applicable to natural sand in water.

In principle, acoustic remote-sensing technologies can be used in the laboratory to obtain measurements without disturbing the mobile bed or the near-bed flow and away from tank sidewalls. In addition, the instrumentation can be made sufficiently robust to deploy in the field with energetic forcing conditions. Broadband MHz-frequency acoustic systems, which simultaneously measure backscatter amplitude and phase at mm-scale range resolution, have been developed to study small-scale flow and sediment dynamics (*Hurther et al.*, 2011; *Hay et al.*, 2012). Promising results of nearbed flow have been obtained in sheet flow conditions (*Revil-Baudard et al.*, 2015; *Fromant et al.*, 2018), over migrating ripples under skewed waves (*Hurther and Thorne*, 2011), dunes under uni-directional flow (*Wilson and Hay*, 2016) and in the field (*Hay et al.*, 2014). In a recirculating tilting flume, *Bareš et al.* (2016) obtained velocity profiles of granular flow of lightweight sediment with a relative density of ~ 1.4. To the authors' knowledge, vertical profiles of velocity within sub-aqueous gravity-driven granular flows using natural sand or sediment with densities similar to that of sand have not been obtained using these types of acoustic systems prior to the present study.

The purpose of this paper is to present laboratory measurements of sub-aqueous gravity-driven granular flows. Sediments were released in the upstream portion of a 15.2 cm wide chute, producing a O(1)cm-thick moving layer of sediment with a width-to-thickness aspect ratio greater than 10 to 1. The sediments used were glass beads and natural sand. The thickness of, and vertical structure of the velocity within, the moving layer were measured using a wide bandwidth coherent Doppler profiler located midway between the chute sidewalls. The velocity profiles are compared to measurements made with video imagery through the chute sidewall. Velocities at and near the sediment-water interface are compared to estimates made with a commercially available Doppler profiler (Vectrino) operating at 10 MHz, and with an overhead video camera, also located away from the chute sidewalls. The observed velocity profiles are compared to predictions from a analytic viscous fluid model, which, in combination with *Bagnold* (1954)'s semi-empirical relation for effective viscosity in high-concentration granular media, yield estimates of porosity and viscosity within the moving layer.

The paper is organized as follows. Sec. 5.2 briefly summarizes the relevant aspects of the theory of granular flow. The experimental setup and instruments are described in Sec. 5.3 with the data analysis methods presented in Sec. 5.4. The measured velocity profiles

and model results are given in Secs. 5.5 and 5.6, respectively. These and related results from the literature are discussed in Sec. 5.7. The summary and conclusions are given in Sec. 5.8.

5.2 Theory

Consider steady, uniform flow of a fluid with excess density $\hat{\rho}$ flowing down a slope of angle α_c relative to the horizontal, with the x coordinate positive downslope and parallel to the bottom, and z positive upwards and normal to the bottom. Assuming hydrostatic pressure and neglecting the non-linear and lateral friction terms, the x-component of the momentum equation is (e.g. *Turner* (1979))

$$\frac{d\tau}{dz} = -\hat{\rho} g \sin \alpha_c \tag{5.1}$$

where τ is the shear stress, $\hat{\rho} = \rho - \rho_w$, ρ is the density of the moving fluid and ρ_w is the density of the ambient fluid, i.e. water in this case.

In his pioneering work on the flow of grains in fluids (*Bagnold*, 1954, 1956), Bagnold identified two regimes, the macro-viscous and grain-inertia regimes, separated by a transitional region. In the grain-inertia regime, stresses are transmitted via particle collisions and depend on the square of the shear rate. In the macro-viscous regime, the shear stress depends on the fluid viscosity modified by the presence of the particles and is linearly proportional to the shear rate

$$\tau = \mu_e \frac{du}{dz} \tag{5.2}$$

where μ_e is the effective viscosity and u is the x-component of velocity. The present work focuses on the macro-viscous regime, with gravity-driven granular flow treated as a fluid obeying Eqs. 5.1 and 5.2 with density ρ given by

$$\rho = (1 - n)\rho_s + n\rho_w \tag{5.3}$$

where n is the porosity and ρ_s is the grain density of the granular material.

Based on his experiments using neutrally-buoyant particles in the sheared annulus between two concentric cylinders, *Bagnold* (1954) defined a non-dimensional number (now referred to as the Bagnold number), Ba, given by the ratio of the inertia stress to the

viscous stress:

$$\text{Ba} = \frac{\rho_s \lambda^{1/2} d_{50}^2 \gamma}{\mu_w} \tag{5.4}$$

where d_{50} is the grain diameter, μ_w is the dynamic viscosity of the interstitial fluid and $\gamma = du/dz$ is the velocity shear rate. *Bagnold* (1954) defined the linear grain concentration, λ, as the ratio of the particle diameter to the average distance between particles, which is related to the volume concentration, $\phi = 1 - n$, by

$$\lambda = \frac{1}{(\phi_0/\phi)^{1/3} - 1} \tag{5.5}$$

where ϕ_0 is the maximum possible static concentration, at which $\lambda = \infty$. For uniformly-sized spheres, ϕ_0 ranges from 0.52 to 0.74 depending on the packing arrangement (*Graton and Fraser*, 1935). For natural uniformly-sized grains, *Bagnold* (1956) assumed a value of 0.65. *Hanes and Inman* (1985) measured values ranging from 0.55 to 0.64 for glass beads and sand. For layers of uniform spheres in a triangular packing pattern, *Bagnold* (1954) found that λ must be less than 22 to allow enough space between adjacent layers of particles to slide past one another. For different sized particles, *Bagnold* (1954) suggested this value would be reduced to ~ 14. For the macro-viscous regime, $Ba < 40$ and for the grain-inertia regime, $Ba > 450$.

For the macro-viscous regime, *Bagnold*'s experiments yielded the following empirical relation for the grain shear stress

$$\tau_g = 2.25 \lambda^{3/2} \mu_w \frac{du}{dz} \tag{5.6}$$

which would be added to the fluid shear stress (*Bagnold*, 1954, Eq. 7). However, for the total shear stress (grain + fluid) in Eq. 5.2, *Bagnold* (1954) indicated that the following semi-empirical expression for μ_e may be more reliable

$$\mu_e = (1 + \lambda)(1 + 0.5\lambda)\mu_w \tag{5.7}$$

where, in this case, τ is not separable into grain and fluid contributions. For $\lambda = 0$, τ reduces to the shear stress of a grainless fluid, i.e., $\mu_w \gamma$.

5.3 Measurement Methods

5.3.1 Experimental set-up

Two types of sediment were used in the present experiments: soda lime glass beads (G) and quartz sand ($S2$), both having been used previously for the sound speed, attenuation and reflection measurements reported in *Hare and Hay* (2018, 2020a,b). Median grain size d_{50}, porosity n and grain density ρ_s are listed in Table 2.3. Details on how these properties were measured are given in *Hare and Hay* (2018).

A scale diagram of the experimental set-up is presented in Fig. 5.1a. A 60 (length) x 15.2 (inside width) x 14.0 (height) cm rectangular chute made of 1.3 cm thick polycarbonate plate was submerged in a 90 (length) x 43 (width) x 48 (height) cm glass-walled tank filled with tap water. The chute was secured at a slope angle, α_c, at which a moving layer of relatively constant thickness could be achieved. This angle choice was determined experimentally for each granular medium (Table 5.1) and was also guided by the work of *Cassar et al*. (2005). Throughout the paper, the coordinate system is defined such that x is parallel to the chute bottom and positive downslope, and z is positive upwards normal to the chute bottom with $z = 0$ at the chute bottom (Fig. 5.1). The chute bottom was covered with anti-slip traction tape (Gator Grip), ensuring a no-slip bottom boundary condition for the granular flow. A reservoir with a movable gate was installed at the upstream end of the chute (Fig. 5.1). The gate height, h_g, was set to 10 mm and 12 mm for the $S2$ and G trials, respectively. A removable rectangular cofferdam made of high-density polyethylene (HDPE) fitted inside the reservoir, flush with side and end walls and the gate.

Table 5.1: Number of repeat trials, N, for the two sediment samples. The chute angle α_c and the range to the fixed roughness bed, r_D, from the MFDop center transducer are listed.

Granular medium	N	α_c [°]	r_D [cm]
G	6	27.1	14.4
$S2$	3	32.5	11.8

For each repeat trial, sediment was poured into the cofferdam (about 570 mL and 850 mL of water-saturated sediment for the sand and the glass beads, respectively) and

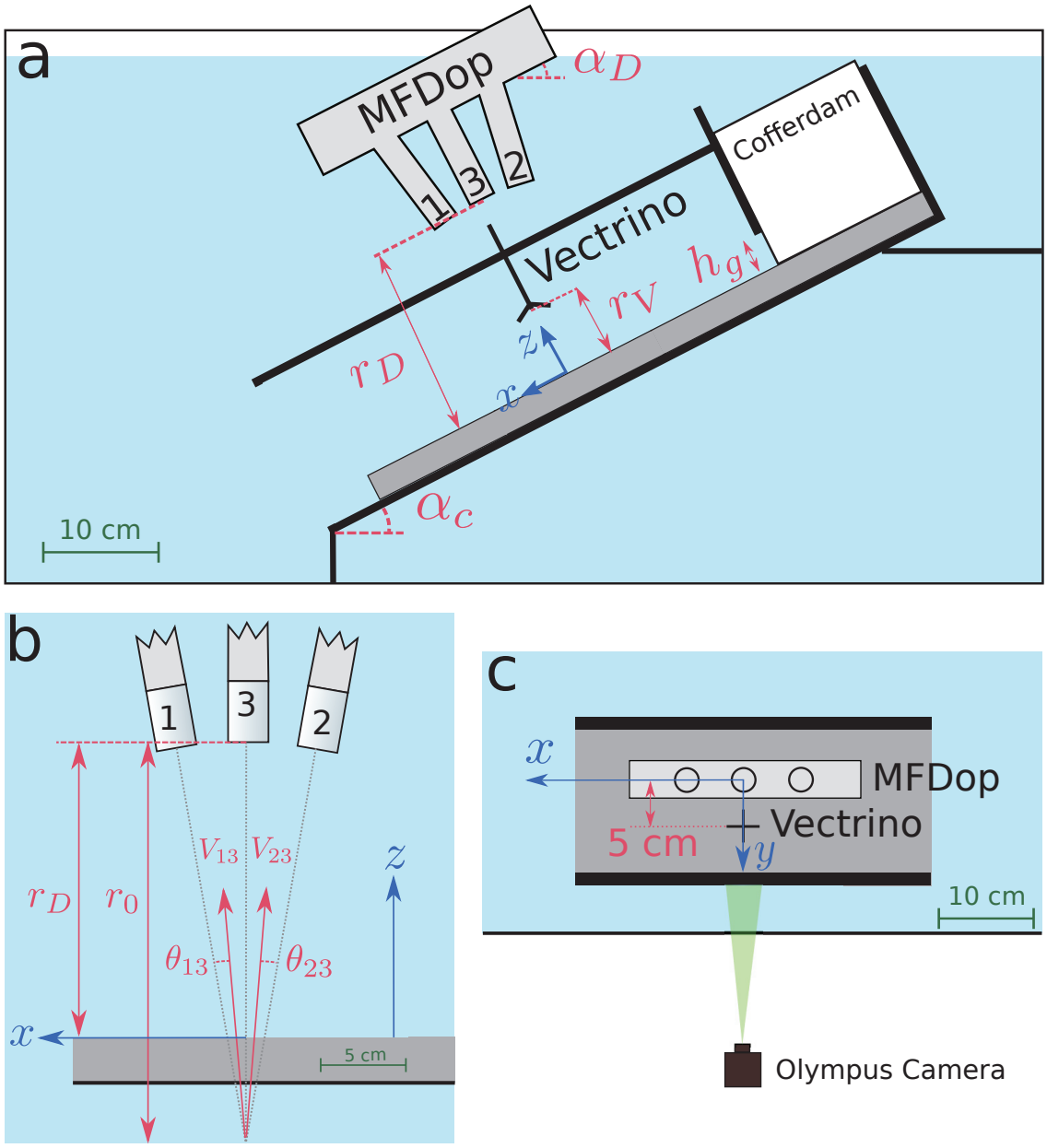

Figure 5.1: Experimental set-up: (a) side view of the chute submerged in the water-filled tank. The gray color indicates the PVC blocks. (b) MFDop geometry, showing the bisector angles θ_{13} and θ_{23}, beam velocities V_{13} and V_{23} and beam intersection point. (c) Top view of the chute looking down the z axis. The chute (x, y, z) coordinate system used throughout the paper is indicated in blue.

data collection was started. The cofferdam was then removed, producing a thin layer of sediment flowing down the chute at a relatively constant thickness. Once the sediment stopped flowing, it was collected and poured back into the reservoir for the next trial. The number of repeat trials, N, for each granular medium is given in Table 5.1. For the G trials, 20 μm polyamid particles were added to provide acoustic scatterers in the water column in order to obtain velocity measurements in the water column immediately above the moving sediment layer. The seeding particles were mixed with the sediment in the cofferdam and also added to the surrounding water.

5.3.2 MFDop instrument

Near-bed flow and backscatter measurements were obtained using a wide-band coherent Doppler profiler (MFDop) based upon the instrument described in *Hay et al*. (2012). In this version, the transducer assembly was constructed from Delrin – a 5.1 (height) x 22.9 (length) x 3.8 (width) cm rectangular support – and three hollow 2.5 cm diameter rods held in place by set screws. Wideband 22 mm diameter Imasonic transducers with 1.7 MHz centre frequency were mounted on the end of each rod with the signal wires running from the transducers through the hollow rods to the data acquisition system described in *Hay et al*. (2012). The center transducer had transmit/receive capabilities, while the two outboard transducers were receive only. The angle between the beam axes of the center and outboard transducers was 10°. The beam axes intersected at a distance $r_0 = 23$ cm from the center transducer (Fig. 5.1c). The bisector angles, θ_{13} and θ_{23}, were 5°. As indicated in the sketch, the geometry of the transducer assembly is isosceles, so that these bisector angles remain the same, independent of range (*Hay et al*., 2012). Based on the theoretical directivity for a circular piston transducer (*Clay and Medwin*, 1977), the nominal start of the farfield is 31 cm and the range to the last pressure maximum is 9.8 cm for 1.2 MHz (*Hare and Hay*, 2020a).

The transmit pulse was a tone burst with a duration of 1.5 μs, corresponding to 1.1 mm resolution in range, which is 3.3 and 2.7 grain diameters for G and $S2$, respectively. The transmit center frequency was 1.2 MHz, so the corresponding full beamwidth at half-power was 3.3°. Data were acquired in 10 pulse pair ensembles at an ensemble acquisition rate of 50 Hz.

The MFDop was mounted so that the centre transducer was ~ 5 cm from the nearest sidewall and about 23 cm downslope of the gate (Fig. 5.1). The MFDop was aligned

by maximizing the bottom return from the chute registered by the center transducer. The vertical distances between the fixed roughness bed and the MFDop center transducer, r_D, used for each granular medium are listed in Table 5.1. Contamination from the sidelobes of the sediment-water interface affected the returns from within the bed due to sound attenuation for these grain sizes and transmit frequency. Thus, the MFDop was positioned closer to the chute bottom than r_0, thereby reducing the size of the transducer footprint at the sediment-water interface and minimizing the contamination of returns from within the moving layer by sidelobe returns from the interface. For the $S2$ trials, this contamination needed to be further reduced and so the instrument was tilted by about 1°. The velocities were computed from the rate of change of phase using the isoceles bistatic geometry (see *Hay et al*. (2012) and Sec. 5.4.1).

5.3.3 Other instruments

Three-component velocity measurements were also made using a commercially available Doppler profiler: the Nortek Vectrino Profiler. The Vectrino was mounted so that it was aligned with the MFDop centre transducer in x, but separated from it laterally by 5 cm in the $+y$ direction (Fig. 5.1c) and ~ 5 cm from the nearest sidewall. The vertical distance, r_V, between the Vectrino centre transducer and the fixed roughness bed was 6.8 cm (Fig. 5.1). The Vectrino operated at an acoustic frequency of 10 MHz with 178 pulse pair ensembles at an ensemble acquisition rate of 50 Hz and a range resolution of 1.0 mm.

For the $S2$ sand, simultaneous observations were made with a digital camera (Olympus E-M10 Mark III) through one of the tank sidewalls (Fig. 5.1d), giving a side-view of the moving layer. High-definition videos were shot at 120 frames per second (fps). The camera was mounted on a tripod ~ 16 cm away from the chute sidewall and tilted to the same angle as the chute. Video calibration was done by placing a ruler in the frame at the start of each trial. A second camera (ELP USB camera) recording at 30 fps replaced the Vectrino in order to optically measure the velocity at the sediment-water interface in mid-chute. The ELP camera was mounted in an acrylic tube (7 cm outer diameter, 49.5 cm height) with a transparent window at the immersed end. The tube was mounted at the same angle as the MFDop with the window about 9 cm away from the bottom. The camera was placed in the tube so that the narrow side of its rectangular field of view was (nearly) parallel to the chute sidewall. For calibration, the ruler was placed against, and parallel to, the chute sidewall. By extracting two points on the ruler from a video frame,

a rotation angle of 1.6° was computed. This angle was used to correct the estimated velocities (see Sec. 5.4.3).

Particle image velocimetry (PIV) measurements could not be made for the glass bead trials, because of the lack of sufficient colour contrast among the glass beads.

5.4 Analysis Methods

5.4.1 MFDop

The MFDop observed velocities are the projections of the flow along the bisectors for each beam pair (Fig. 5.1b) and are given by (*Hay et al.*, 2012)

$$V_{13} = u \sin\theta_{13} + w \cos\theta_{13} \tag{5.8}$$

$$V_{23} = -u \sin\theta_{23} + w \cos\theta_{23} \tag{5.9}$$

where u and w are the x and z components of velocity. For $\theta_{13} = \theta_{23} = \theta_0$, the velocity components are given by

$$u = \frac{V_{13} - V_{23}}{2 \sin\theta_0} \tag{5.10}$$

$$w = \frac{V_{13} + V_{23}}{2 \cos\theta_0}. \tag{5.11}$$

A second estimate of w is given by the detected velocity along the center beam, V_{33}. For the $S2$ trials, because the MFDop was tilted slightly away from normal, the bistatic calculation was taken. From Eq. 5.8 and using $w = V_{33}$, the x component of velocity in instrument coordinates is

$$\tilde{u}_{13} = \frac{V_{13} - V_{33} \cos\theta_0}{\sin\theta_0}. \tag{5.12}$$

The velocity was then rotated to chute coordinates as described in Sec. 5.4.5. All MFDop velocities were high-graded by removing points for which the magnitude of the ensemble-averaged complex correlation between consecutive pulses for any transducer was less than 0.7. Averaged over N repeat trials, the percentage of discarded data points in the water column was $83\% \pm 1.6\%$ and $38\% \pm 9\%$ for $S2$ and G, respectively. Fewer data points were discarded for G since seeding particles were used for these trials, leading to higher correlations in the water column. In the granular flow layer, nearly all data points had

correlations higher than 0.7.

The sediment-water interface, η_D, was defined to be the range at which both the backscatter amplitude and correlation registered by the center transducer exceeded specified thresholds. A one-dimensional median filter of order 100 was then implemented to remove the quantized variations associated with discrete range bins. For the MFDop data, $z = 0$ was given by the range to the maximum amplitude at the beginning of the trial, i.e. before the arrival of the leading edge of the downslope granular flow.

As an initial validation test of the MFDop measurements, the bulk sediment transport volume was estimated from $S2$ trials with h_g set to 13.8 mm. For these trials, the MFDop was positioned normal to the bed with $r_D = 25.8$ cm. The first estimate of bulk volume, V_B, was computed by subtracting the volume of water-saturated sediment that remained in the chute upstream of the measurement point after a trial was completed from the volume of water-saturated sediment initially poured into the cofferdam, which was 1000 mL for these trials. Second, the bulk volume was computed using the MFDop measurements: $V_D = W \int u(h_D, t) h_D(t) dt$, where W is the chute width, $h_D(t)$ is the thickness of the moving layer estimated from the Doppler backscatter amplitude, and $u(h_D, t)$ is the velocity at the sediment-water interface. The measured surface velocity was used here instead of the velocity profile due to the returns from within the bed being contaminated by sidelobe returns from the sediment-water interface (discussed in Sec. 5.3.2) for this MFDop position. The bulk volume equation makes several assumptions including a constant surface velocity across the chute (which neglects wall effects) and a constant velocity profile within the moving layer (which is not the case as shown later). Averaging over 3 repeat trials, V_D was 25% larger than V_B. Given these approximations and the relatively crude nature of the test, it was judged that this degree of agreement was sufficiently good to proceed.

5.4.2 Vectrino

Similar to the MFDop measurements, the Vectrino data with correlations below 0.7 were rejected. The sediment-water interface was determined as follows. First, a binary image was created, with backscatter amplitude above a specified threshold assigned a value of 1 and all others a value of 0. Isolated groups of fewer than 20 equi-valued connected bins were replaced by their binary opposite value. The sediment-water interface, η_V, the subscript denoting the Vectrino, was given by the uppermost non-zero bin for each time

step. To remove quantized variations associated with discrete range bins, η_V was despiked by removing points where the difference between η_V and the low-passed filtered η_V was larger than 3 bins. To further smooth the sediment-water interface, a one-dimensional median filter of order 10 was implemented.

5.4.3 Cameras

Single frames were extracted from each video file. An example frame from the side-view camera for one of the $S2$ trials is presented in Fig. 5.2, where the sediment-water interface, $\eta_{sv}(x)$, is indicated, the subscript sv denoting "side-view". This interface was computed using the method outlined in *Hare and Hay* (2020b) and summarized here. A binary image was created with normalized pixel entropy above a specified threshold assigned a value of 1 and all others a value of 0. Isolated groups of fewer than 1000 equi-valued connected pixels were replaced by their binary opposite value. The values of $\eta_{sv}(x)$ was given by the uppermost non-zero pixel for each horizontal position in the image.

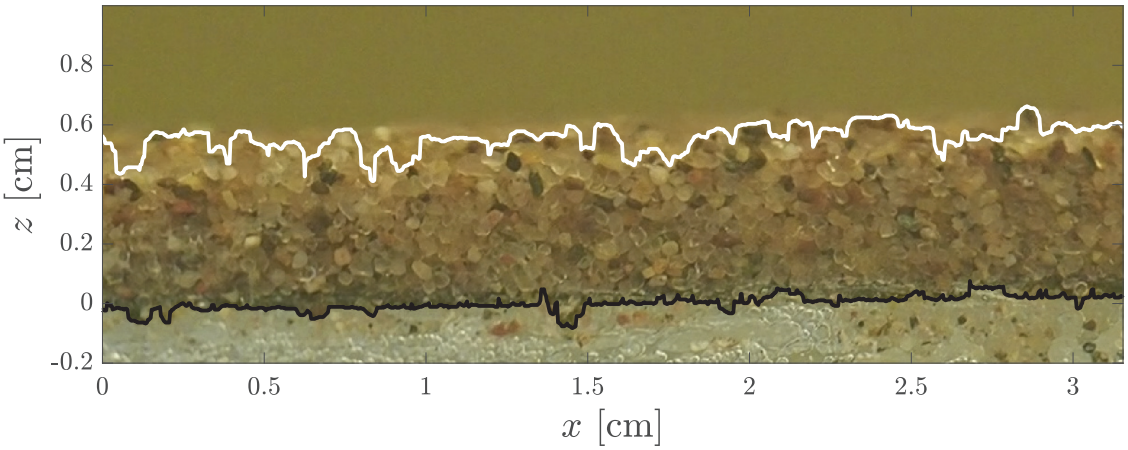

Figure 5.2: A video frame taken through the chute side-wall with the side-view camera during a $S2$ trial. The extracted sediment-water interface, η_{sv}, and the top of the fixed roughness bottom, z_0, are indicated by the white and black lines, respectively. The flow is from right to left.

The fixed roughness bottom, $z_0(x)$, was determined as follows. For each image, the intensity values in grayscale were first mapped to new values where the bottom 1% and the top 1% of all pixels are saturated. Similar to the detection of η_{sv}, a binary image was created and isolated groups of fewer than 1000 equi-valued connected pixels were replaced by their binary opposite value. The fixed roughness bottom was given by the

lowermost non-zero pixel for each horizontal position in the image. The time series of the sediment thickness, $h_{sv}(t)$, is given by the frame-averaged difference between $\eta_{sv}(t,x)$ and $z_0(t,x)$.

Velocities were computed using particle imaging velocimetry (PIV). Each frame was partitioned into non-overlapping rectangular sections measuring $10d_{50}$ (in x) x $2d_{50}$ (in z) and the mean intensity from each section was removed. For each rectangular section, the corresponding section in the subsequent frame was enlarged by $2d_{50}$ in the x direction. The peak of the normalised 2D cross-correlation between corresponding sections in each frame pair yielded the spatial lag in x and z for each section, which were then converted to a velocity by multiplying by the frame rate. Vertical profiles of $u(t,z)$ and $w(t,z)$ were obtained by first averaging over x for each frame pair and then over 0.2 s.

Similar to the side-view camera, surface particle velocities, $u(t,y)$ and $v(t,y)$, were computed from top-view camera frame pairs using the PIV method described above. However, in this case, frames were partitioned into $20d_{50}$-sized square sections with an overlap of $8d_{50}$ in x and y between sections. Due to camera distortion at the frame edges, only the centre part (1285 pixels x 743 pixels) of the total image (1920 pixels x 1080 pixels) was used. The y-boundaries of the cropped image were located at $\sim$2.5 cm and $\sim$5.3 cm from the nearest sidewall. The computed velocities were rotated to the chute coordinate system using the extracted rotation angle of 1.6° (see Sec. 5.3). The top-view velocities were then averaged over cross-chute position.

5.4.4 Five second averaging window

For the granular flow trials, the data streams from all instruments were synchronised by defining $t = 0$ as the time at which u at the elevation of the sediment-water interface exceeded a specified threshold, indicating the arrival of the leading edge of the downslope flow. Examples of the backscatter amplitudes and ensemble-averaged pulse-pair correlations from the MFDop center transducer are given in Fig. 5.3ab for a single $S2$ trial and Fig. 5.3cd for a G trial. The 5-s averaging window, during which the layer thickness remained relatively constant, is indicated for both trials. Five second was chosen because it was the minimum duration of the constant thickness portion of the record for all trials. The backscatter amplitude at the sediment-water interface is larger for G than for $S2$, consistent with a larger reflection coefficient for the glass beads (*Hare and Hay*, 2020b). During the 5-s averaging window, the returns from the chute bottom are larger for G than

for $S2$, which can be partially explained by the higher attenuation at the larger grain size for the sand, corresponding to a theoretical $G/S2$ backscatter amplitude ratio equal to 1.7 for two-way travel through a 8 mm thick stationary layer (*Hare and Hay*, 2018).

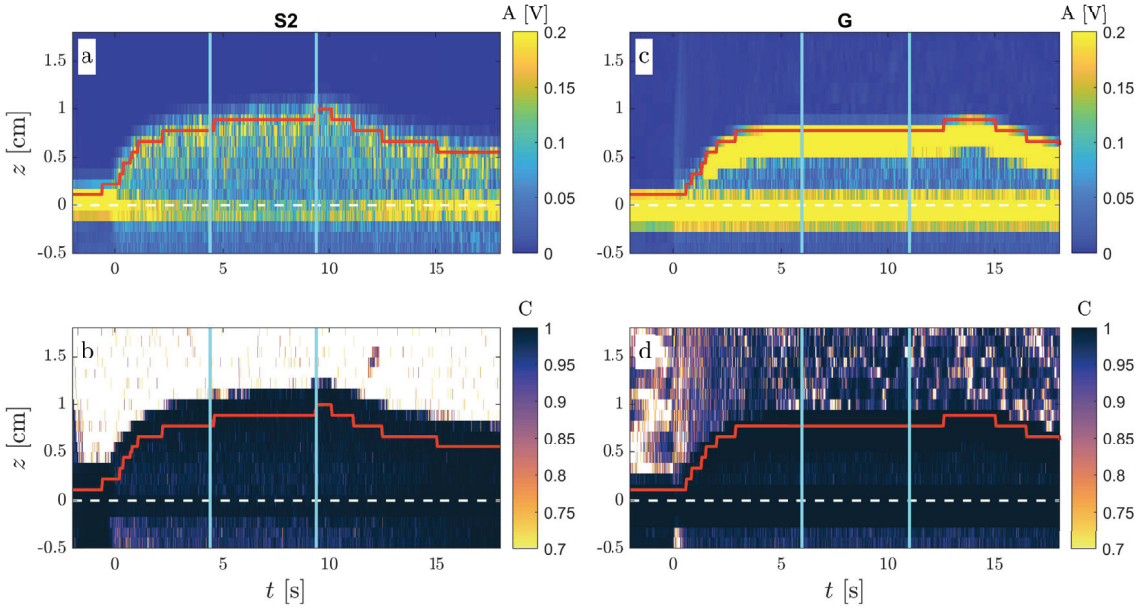

Figure 5.3: Backscatter amplitudes A and correlations C for single trials of $S2$ (a,b) and G (c,d) sediment. Data are from the MFDop center beam. Correlations within the moving layer are well above 0.7, and representative of all trials in this study. For the $S2$ trial, seeding was not used and so the correlations within the water column are low. The estimated thickness of the moving layer and the top of the fixed roughness bed are indicated by the red solid and white dashed lines, respectively. The vertical cyan lines denote the averaging window used to compute the time-averaged velocity profiles for these trials.

5.4.5 Coordinate rotation

Rotation from instrument to chute coordinates is given by

$$u = \tilde{u}\cos\beta - \tilde{w}\sin\beta \tag{5.13}$$

$$w = \tilde{u}\sin\beta + \tilde{w}\cos\beta \tag{5.14}$$

where the tildes denote the instrument coordinate system and β is a rotation angle. If $w = 0$, the rotation angle can be computed from Eq. 5.14:

$$\tan\beta = -\frac{\tilde{w}}{\tilde{u}}. \tag{5.15}$$

For the glass bead trials, the MFDop was oriented normal to the chute bottom and, as will be seen later, the 5-s averaged profile of w was close to zero within the moving layer. For the $S2$ measurements, because the MFDop was tilted so that the axis of the centre beam was at a slight angle with respect to the bed normal, rotation angles $\beta_D(z)$ were computed for each trial using the values of $\tilde{u}_{13}$ and V_{33} from within the moving layer using Eq. 5.15, thereby forcing w in the moving layer to zero. The velocities were then converted to chute coordinates using Eqs. 5.13 and 5.14. The average value of β_D from 3 repeat trials was $2.8° \pm 0.4°$.

An example of the 5 s average profiles of $\tilde{u}$ and $\tilde{w}$ measured by the Vectrino for a single trial of G is given in Fig. 5.4. The x component of velocity does not go to zero at $z = 0$ due to the high attenuation of sound in this medium at 10 MHz. Therefore, the velocities measured deeper within the moving layer in fact represent contamination from the sediment-water interface via the sidelobes in the transducer beam pattern. For these bins, the measured z component of velocity, $\tilde{w}$, is non-zero, indicating that the Vectrino was tilted relative to the sediment-water interface. Therefore, the Vectrino measurements were rotated to chute coordinates using Eqs. 5.13 and 5.14. To do so, an average rotation angle, β_V (Eq. 5.15), was computed for each trial using the velocity bins within the moving layer from $z = 0$ to z corresponding to the maximum value of $\tilde{u}$ within the moving layer (highlighted in Fig. 5.4). The computed rotation angle was small, with a mean rotation angle of $2.5° \pm 0.1°$ for all the G trials. The velocities corrected to chute coordinates are also plotted in Fig. 5.4, showing the near zero values of w, and that u overlays $\tilde{u}$.

5.5 Results 1: Velocity Profiles

5.5.1 MFDop vs PIV

Vertical profiles of $u(z)$ measured by the side-view camera and the MFDop averaged over 5 s and three repeat $S2$ trials are shown in Fig. 5.5. The error bars denote the minimum and maximum values and indicate the repeatability of the measurements. The MFDop u profile exhibits a velocity maximum within the moving layer, bounded above and below by shear layers: one immediately above the bottom and one spanning the sediment-water interface. The mean thickness of the moving layer estimated from the MFDop measurements was 9.2 ± 0.5 mm, corresponding to 23 grain diameters (see Table

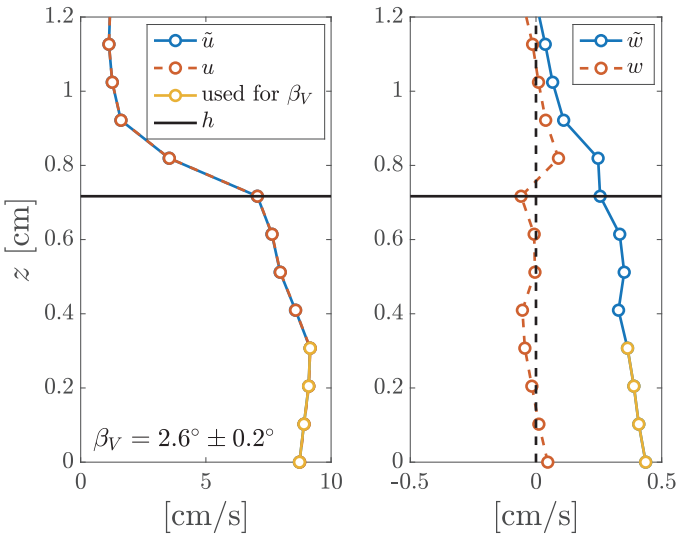

Figure 5.4: Vertical profiles of the x and z components of velocity obtained with the Vectrino in instrument ($\tilde{u}$,$\tilde{w}$) and chute (u,w) coordinates for a G single trial. The average rotation angle for this trial, $\beta_V = 2.6°$, was computed using the yellow velocity bins (see also Sec. 5.4.5). The thickness of the moving layer, h, is also indicated.

5.2). Compared to the MFDop estimates, velocities measured by the side-view camera are much lower (≤ 1 cm/s compared to ≤ 8.2 cm/s), and do not exhibit a velocity maximum at depth within the layer. The flow thickness estimate from the side-view is 35% less than the acoustic estimate. Visual observations indicated that the moving layer was thinner at the side wall. We attribute these differences to the effects of sidewall friction.

Table 5.2: Results from the MFDop velocity measurements where $\bar{h}$ is the moving layer thickness and $\bar{u}_m$ is the maximum velocity located at z_m within the moving layer. The overbar denotes the average over N trials (see Table 5.1). Also listed is ζ computed using Eq. 5.19.

Granular medium	h [mm]	h/d_{50}	$\bar{u}_m$ [cm/s]	z_m/h	ζ [s/m^2]
G	7.70 ± 0.08	23.0	8.0	0.56	1920
$S2$	9.2 ± 0.5	22.6	8.0	0.66	834

Time series of the x component of surface velocity measured by the MFDop and top-view camera for a single trial of $S2$ sand are plotted in Fig. 5.6. For the MFDop, the surface velocity was given by u at $z = h_D$. Both the top-view camera and MFDop data were averaged over 1 s intervals. The surface velocity averaged over the 5 s window

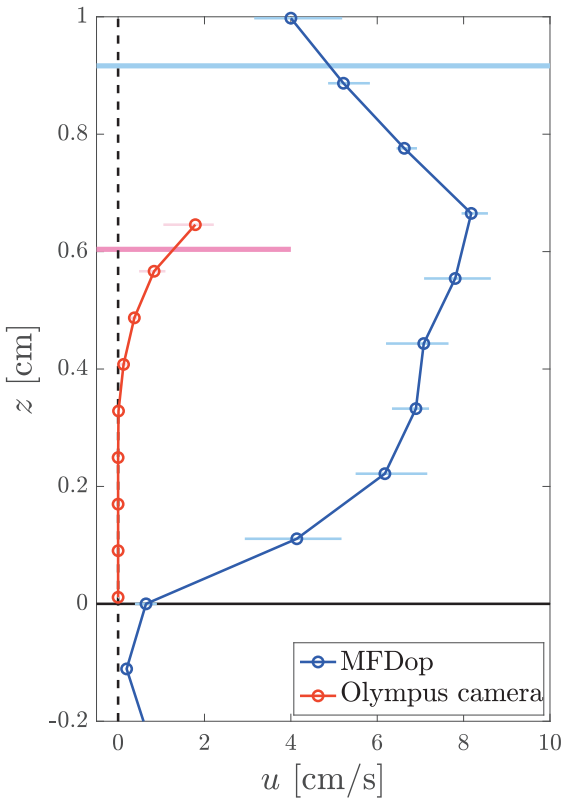

Figure 5.5: Vertical profile of the x component of velocity averaged over three repeat $S2$ trials measured by the MFDop (blue) and the side-view camera (red). Horizontal bars denote the minimum and maximum mean values for the three repeat trials. The mean thickness of the moving layer estimated from the MFDop backscatter amplitude and side-view camera imagery are indicated by the light blue and pink lines, respectively. The black line indicates the chute bottom at $z = 0$.

(dashed vertical bars in Fig. 5.6) and then over three repeat trials is 7.1 cm/s $\pm$ 0.3 cm/s and 4.6 cm/s $\pm$ 1.4 cm/s for the top-view camera and MFDop data, respectively. The MFDop velocity profile in Fig. 5.5 indicates a velocity of $\sim$7 cm/s at about 1 bin below the estimated sediment-water interface. The difference in surface velocity estimates from the top-view camera and the MFDop seems likely to be due to the two instruments capturing different parts of the moving layer, with the top-view camera imagery being biased toward particles at z-values below the position of the sediment-water interface detected by the MFDop.

5.5.2 MFDop versus Vectrino

The backscatter amplitude in dB (i.e., $20 \log_{10} A$) registered by the MFDop for a single G trial is shown in Fig. 5.7a with 2 s averaged u velocity profiles from the MFDop

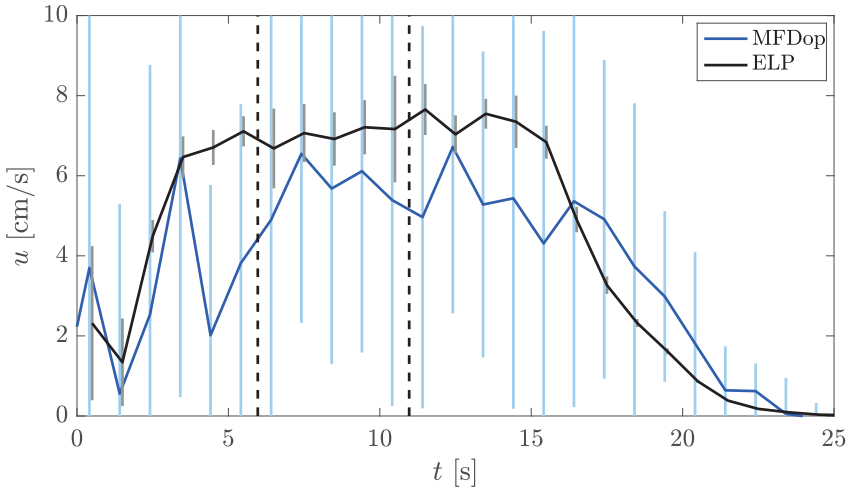

Figure 5.6: Mean x component of 1-s average velocity obtained from the top-view camera (black line) for a single $S2$ trial and from the MFDop at the sediment-water interface (blue line). Both quantities have been averaged over 1 s intervals. The vertical grey and blue lines represent ± 1 standard deviation. Over the 5 s interval indicated by the vertical dashed lines, the mean velocity is 7.0 cm/s and 5.7 cm/s for the top-view camera and MFDop, respectively.

and Vectrino overlayed. The MFDop data show that the flow is quite steady within the moving layer during the 5 s to 15 s interval after passage of the front. MFDop and Vectrino vertical profiles of u and w averaged over the 5 s window from $t = 6$ to 11 s and over similarly-chosen 5 s windows for 6 repeat trials are presented in Fig. 5.7b and c. The mean thickness of the moving layer measured by both instruments is comparable, differing by only 1 or 2 bins.

The MFDop u profiles in Fig. 5.7a and b exhibit a maximum velocity within the moving layer with velocities tending to zero at $z = 0$, similar to the observations for the $S2$ sand in Fig. 5.5. In the water column, the MFDop and Vectrino u velocities agree and tend toward zero with increasing distance away from the moving layer. Within the moving layer, the u profiles from the two instruments are in good agreement in the upper part of the flow, both exhibiting similar values and negative shear rates above the velocity maximum at mid-depth within the moving layer. However, the profiles diverge markedly as the bed is approached. In contrast to the MFDop measurements, the Vectrino u velocities close to the chute bottom (open circles in Fig. 5.7b) do not tend toward zero, instead remaining almost constant at the maximum value, for the reasons discussed in Sec. 5.4.5. The w velocities within the moving layer are near zero for both instruments.

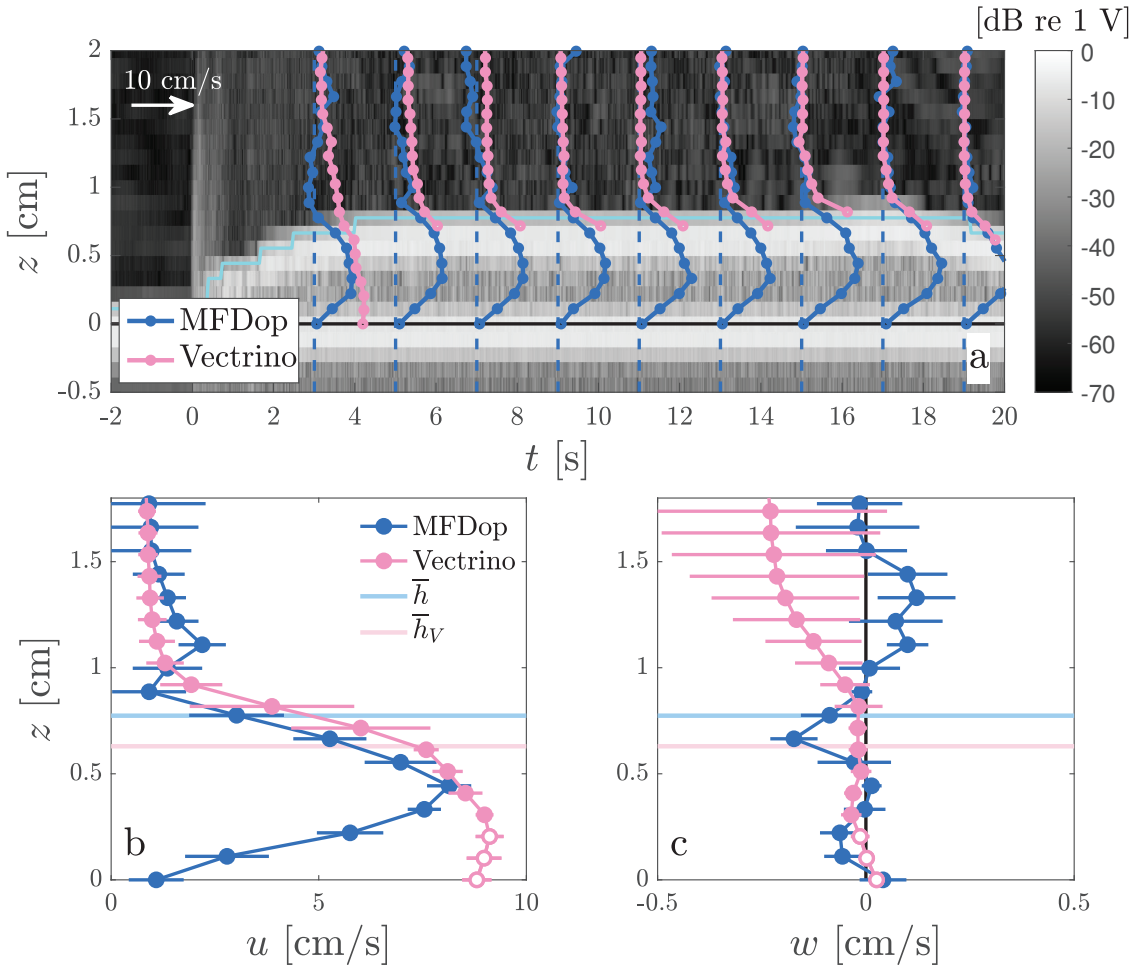

Figure 5.7: (a) Backscatter amplitude from the MFDop centre beam for a single G trial. The cyan line indicates the sediment-water interface. The horizontal black line is the chute bottom. Profiles of 2 s averaged u velocity measured with the MFDop and Vectrino are indicated in blue and pink, respectively. All Vectrino profiles except the first are truncated at the sediment-water interface, to reduce clutter. (b) Vertical profiles of u and (c) w averaged over a 5 s window and 6 repeat trials. The open circles represent the erroneous Vectrino data (see text). The error bars are ± 1 standard deviation. The horizontal light blue and pink lines are the mean thickness of the moving layer measured by the MFDop and Vectrino, respectively.

5.6 Results 2: Model Predictions

5.6.1 Assumptions

The MFDop velocity profiles in Fig. 5.7a indicate that during the $5 < t < 15$ s interval the 2-s mean flow profiles were steady, and the flow thickness constant, justifying the assumption of steady flow in Eq. 5.1. Given the good agreement between MFDop and Vectrino measurements of u at and immediately below the sediment-water interface, and given the 5 cm separation in y between these two instruments, it follows that lateral friction effects were small and can be neglected. Thus, we are justified in adopting the 2-dimensional form of the x-component of the momentum equation, a conclusion which is consistent with the small h/W aspect ratio of the granular flows in these experiments. Furthermore, as indicated by Fig. 5.7c, $w \sim 0$ throughout the moving layer, so $\partial w/\partial z \sim 0$. It follows from the 2-D form of the continuity equation that $\partial u/\partial x \sim 0$. We are therefore justified in dropping the advective term from the momentum balance as well. Thus, the momentum balance reduces to Eq. 5.1 which is used to predict the flow and effective viscosity within the moving layer using the two approaches outlined below.

5.6.2 Constant density model

The MFDop u velocity profile for the glass beads in Fig. 5.7b has the parabolic shape characteristic of plane Poiseuille flow (*Kundu*, 1990), despite the flow here being driven by gravity instead of an externally-imposed pressure gradient, and the absence here of a no-slip condition at the upper boundary. In the simple case of a constant density profile in the moving layer, Eq. 5.1 becomes

$$\mu_e \frac{d^2u}{dz^2} = -\hat{\rho} g \sin\alpha_c \tag{5.16}$$

where the effective viscosity, being a function of porosity, is independent of z as well. Invoking the boundary conditions $u = 0$ at $z = 0$ and $\gamma = 0$ at the velocity maximum at height z_m within the moving layer, the solution to Eq. 5.16 is parabolic:

$$u(z) = -\frac{\zeta}{2} g \sin\alpha_c (z^2 - 2z_m z) \tag{5.17}$$

where

$$\zeta(n) = \frac{\hat{\rho}}{\mu_e} \tag{5.18}$$

and $u = u_m$ at $z = z_m$. Eq. 5.17 indicates that if $z_m \geq h/2$, $u(h) \geq 0$. The parameter ζ was determined from Eq. 5.17 at the velocity maximum:

$$\zeta = \frac{2u_m}{g \sin \alpha_c z_m^2} \tag{5.19}$$

Given a value for ζ, and a relationship for μ_e as a function of n, the corresponding values of n and μ_e can then be calculated.

5.6.3 Variable density model

A second model was constructed to allow the porosity to vary with z, accounting for the vertical variations in the shear rate. Profiles of $\mu_e(z)$ were obtained by piecewise integration of Eq. 5.1 using two approaches: bottom-up or top-down. Eq. 5.1 was integrated from z to $z + \Delta z$ in the former and from z to $z - \Delta z$ in the latter. Using Eq. 5.2, the effective viscosity in each bin is

$$\mu_e(z \pm \Delta z) = \frac{\tau(z) - \hat{\rho}(z) g \sin \alpha_c \Delta z}{\gamma(z \pm \Delta z)} \tag{5.20}$$

where $\hat{\rho}(z)$ has been assumed constant in each Δz interval. In the top-down approach,the only unknown is the porosity at $z = h$, since a value for the shear is provided by the data. The porosity output from the constant density model, n, was used.

In the bottom-up approach, both the shear and the porosity at $z = 0$ are unknown. An estimate for the bottom shear was obtained by integrating Eq. 5.16 from 0 to z_m (making use of $\gamma = 0$ at z_m) and using Eq. 5.2 to get

$$\gamma(0) = \frac{\hat{\rho}(n) g \sin \alpha_c z_m}{\mu_e(0)}. \tag{5.21}$$

Integrating Eq. 5.1 over the half bin from $z = 0$ to $z = \Delta z/2$ yields the effective viscosity at $\Delta z/2$

$$\mu_e(\Delta z/2) = \frac{\tau(0) - \hat{\rho}(0) g \sin \alpha_c \Delta z/2}{\gamma(\Delta z/2)} \tag{5.22}$$

where $\tau(0) = \mu_e(0)\gamma(0)$ with $\gamma(0)$ given by Eq. 5.21 and $\mu_e(0)$ given by Eq. 5.7 with $n(0)$ set equal to the measured porosity for stationary sediment (Table 2.3).

5.6.4 Glass beads

The MFDop velocity profiles for the 6 repeat G trials are plotted in Fig. 5.8 together with their ensemble average, $\bar{u}(z)$, where the overbar denotes the average over N trials (Table 5.1). Also indicated is the corresponding maximum velocity, $\bar{u}_m$, at height z_m within the moving layer (listed in Table 5.2). This value was obtained from a second order polynomial fit to three points bracketing the maximum observed $\bar{u}$. The profile obtained from the constant density model, Eq. 5.17 with ζ given by Eq. 5.19 and the values listed in Table 5.2, is also plotted. The value of $\mathbf{R}^2$ between the observed $\bar{u}$ profile and the model prediction is 0.94.

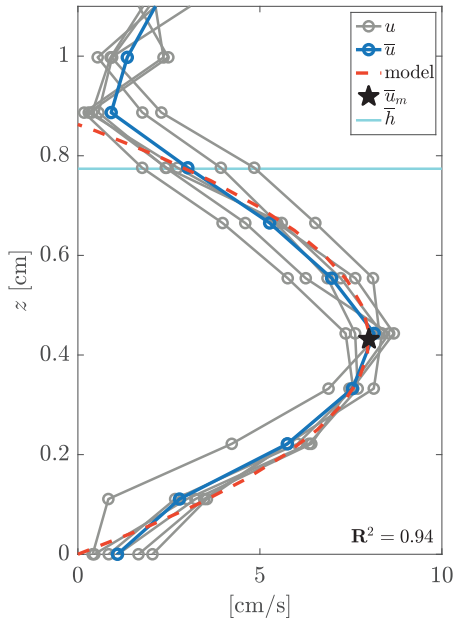

Figure 5.8: Vertical profiles of 5 s averaged u velocities measured with the MFDop for 6 repeat G trials. The velocity, $\bar{u}$, and height of the sediment-water interface, $\bar{h}$, averaged over the 6 repeat trials are indicated. The star is the maximum velocity from a second order polynomial fit to three points around the maximum of $\bar{u}$. The dashed red line is the fit to the constant density model, Eq. 5.17 with $\phi_0 = 0.6$. The coefficient of determination, $\mathbf{R}^2 = 0.94$, between $\bar{u}$ and the model is indicated.

From the computed ζ parameter (Eq. 5.19 and listed in Table 5.2), the porosity n and relative viscosity $\mu_r = \mu_e/\mu_w$ of the moving layer were determined using Eq. 5.18 with Eq. 5.3 for ρ and *Bagnold* (1954)'s expression for μ_e in the macro-viscous regime, Eq. 5.7 with $\phi_0 = 0.6$. The resulting values are listed in Table 5.3. Given the constant density profile assumed in the model, these two parameters represent the depth-averaged values

for the moving layer. The predicted porosity is higher than that measured for stationary glass beads (Table 2.3), consistent with the physics of the layer being more dilute due to shear-induced dilation. Also listed is the Reynolds number, $\mathrm{Re} = \rho \bar{u}_m \bar{h}/\mu_e$ with ρ given by Eq. 5.3 using the porosity from the model output n. The computed Reynolds number is small, consistent with laminar flow.

Table 5.3: Results from the constant density model where n and μ_r are the porosity and relative viscosity of the moving layer, λ is given by Eq. 5.5 and Re is the Reynolds number.

Granular medium	n[1]	μ_r	λ	Re
G	0.462	409	27	2.7
$S2$	0.438	1115	46	1.3

[1]Computed using Eq. 5.7. If Eq. 5.6 is used instead, n values are reduced by $\sim 2\%$.

The shear at the chute bottom and sediment-water interface were estimated from a fit to the two points of $\bar{u}$ closest to $z = 0$ and $\bar{h}$, respectively. Inserting these values into Eq. 5.2 and using the predicted depth-averaged effective viscosity (Table 5.3), the magnitude of the shear stress divided by ρ (Eq. 5.3 using n) was 35 $\mathrm{cm}^2/\mathrm{s}^2$ at the bottom and 46 $\mathrm{cm}^2/\mathrm{s}^2$ at the interface. These values are more than 2 orders of magnitude larger than the observed Reynolds stresses at the interface (see Sec. 5.10), indicating that the stress at the interface is dominantly viscous, and that the Reynolds numbers of these flows were too low for turbulence to play a role in the dynamics.

Results from the variable density model (using the equations given in Sec. 5.6.3) are plotted in Fig. 5.9 for both the top-down and bottom-up approaches to the piecewise integration. In Fig. 5.9a, the measured MFDop shear profile with the value at $z = 0$ computed using Eq. 5.21 is compared to the linear shear profile from the constant density model obtained from differentiating Eq. 5.17 with respect to z. The predicted profiles of viscosity using both approaches are comparable to each other and to the estimate from the constant density model. However, the estimate of μ_r at the $z = 0$ from the bottom-up approach is more than 400 times larger than μ_r from the constant density model. This difference stems from the requirement to assume values for $n(0)$ and $\gamma(0)$. The profiles of λ and Bagnold number are also plotted in Fig. 5.9. The predicted Bagnold numbers are less than 40, confirming that the flow is in *Bagnold*'s macro-viscous regime. The structure in the predicted porosity profile is driven by the shear with both approaches

predicting higher porosities at or just above the height of the velocity maximum, z_m. The porosity profiles from both approaches tend toward lower values in the layer between the velocity maximum and the bed. Otherwise, the predicted porosity profiles oscillate around the estimate from the constant density model with the average porosity from either approach only differing by 0.9% and 2.7% compared to n.

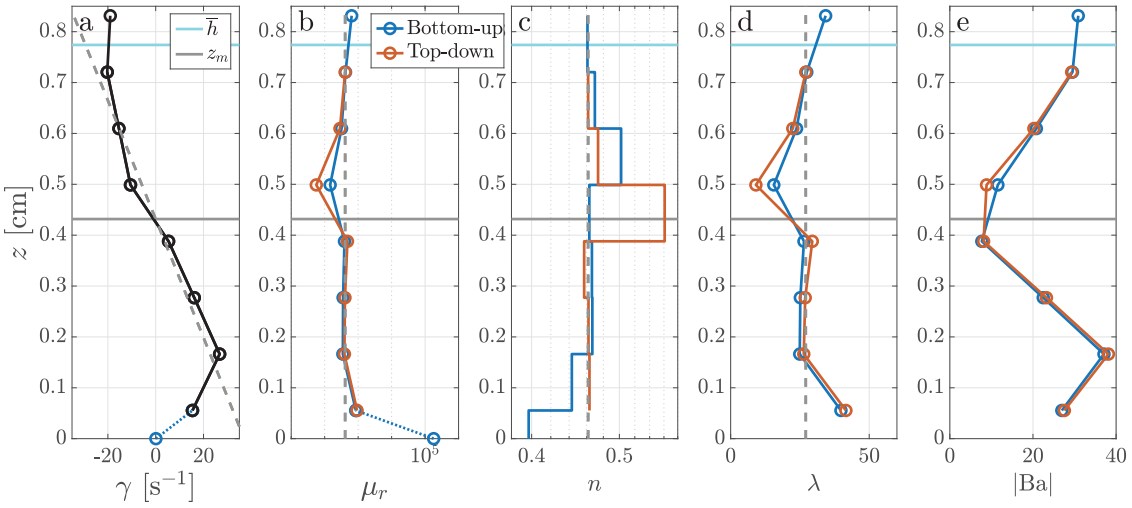

Figure 5.9: (a) MFDop-measured shear rate profile. The data point at $z = 0$ was estimated using Eq. 5.21. Profiles of (b) relative viscosity, μ_r, (c) porosity, n, (d) linear grain concentration, λ (Eq. 5.5) and (e) Bagnold number (Eq. 5.4) obtained for both versions of the variable density model. The horizontal solid cyan and grey lines indicate the average height of the sediment-water interface, $\bar{h}$, and the height of the velocity maximum, z_m, respectively. In (a), the dashed grey line is the modelled shear obtained from differentiating Eq. 5.17 with respect to z. In the other subplots, the dashed grey lines are the parameters from the constant density flow model listed in Table 5.3.

5.6.5 Sand

Fig. 5.10 presents the model-data comparisons for the $S2$ trials. The value of u_m is similar to that obtained for G, but located closer to the sediment-water interface. The shape of the velocity profile for $S2$ is less parabolic than that for G, but the fit to the constant density model is still quite good with an $\mathbf{R}^2$ value of 0.83. Also similar to G, the predicted depth-averaged porosity in the moving layer is larger than that measured for stationary sediment (Tables 2.3 and 5.3). The predicted depth-averaged effective viscosity for $S2$ is 2.7 times larger than that for G (Table 5.3).

The shear stress at the sediment-water interface and chute bottom were determined in the same manner as that described for G in Sec. 5.6.4. Absolute values of 182 cm^2/s^2

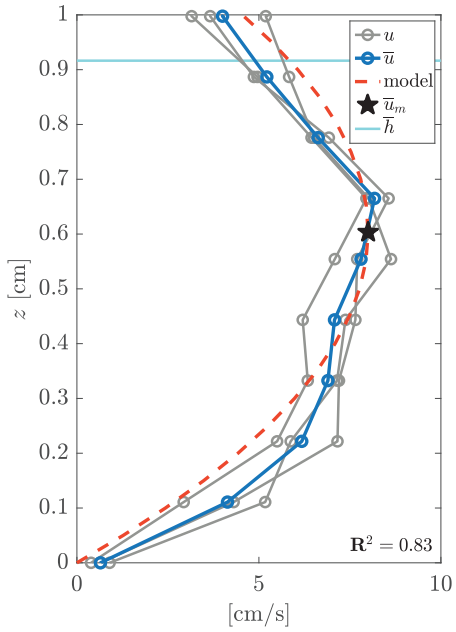

Figure 5.10: Same as Fig. 5.8 except for 3 repeat $S2$ trials.

(bottom) and 73 $\mathrm{cm}^2/\mathrm{s}^2$ (sediment-water interface) were computed for $S2$, which are 5.2 and 1.7 times larger than those obtained for G, respectively. The higher values of effective viscosity and shear stress at the upper and lower boundaries of the flow for sand compared to glass beads are consistent with scanning electron microscope images showing that the beads are much smoother and rounder than the irregularly shaped sand grains (*Hare and Hay*, 2018).

Results for $S2$ from both approaches of the variable density model are plotted in Fig. 5.11. Compared to the results for G, the measured shear profile deviates slightly more from the predicted linear profile of the constant density model due to the velocity profile being less parabolic. However, comparable to G, the predicted relative viscosity and porosity from both approaches oscillate around the values from the constant density model, and exhibit similar tendencies toward higher porosities in the layer above the velocity maximum and lower porosities in the layer between the velocity maximum and the bed. The Bagnold number is generally less than 40, confirming that most of the flow is in the macro-viscous regime. The values of Ba in the bins closest to the bottom are higher, suggesting that the nearbed flow may be in the lower end of the transitional regime (though still well below the grain-inertia regime for which Ba$>$ 450).

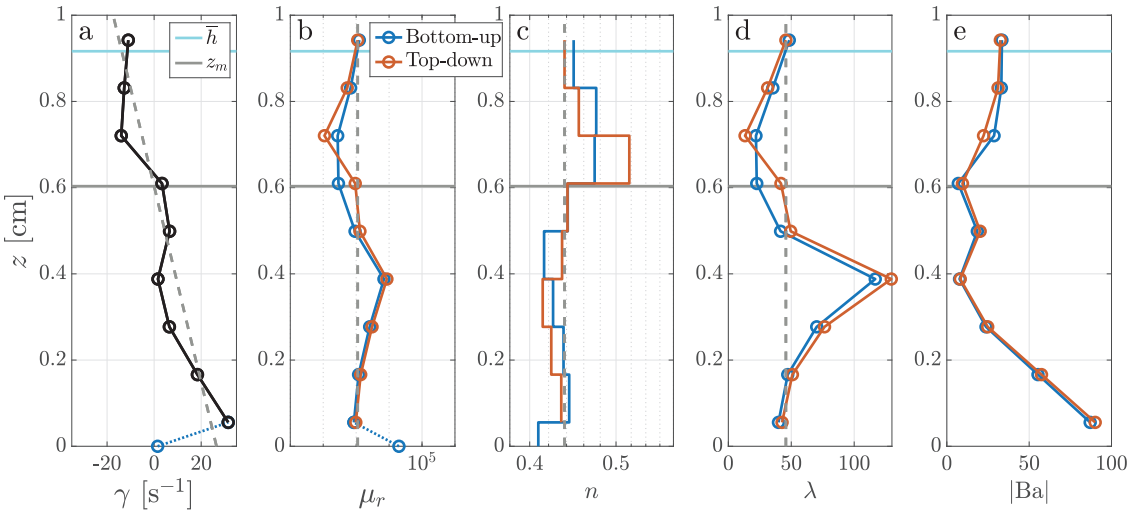

Figure 5.11: Same as Fig. 5.9 except for $S2$.

5.7 Discussion

5.7.1 Identifying the sediment-water interface

In order to determine the appropriate criterion for estimating the range to the interface from the observed backscatter amplitude profile, the quasi-2D single-scattering reflection model described in *Hare and Hay* (2020b) was implemented for G at 1.2 MHz. The model is briefly summarized here. Discrete particles are selected at random from the parent size distribution and placed side-by-side in a row. The particles in the row then undergo Guassian-distributed random vertical displacements so that the modelled surface roughness was close to the measured value. The quasi-2D array of particles is created from successive rows separated by a distance equal to the maximum grain diameter.

Here, the finite duration of the transmit pulse was taken into account. The transmit pulse was a 1.2 MHz cosine with a Hanning window applied to taper it and a pulse length $\tau_p = 1.5$ μs. The backscattered pressure from the jth particle in a given row is

$$p_j = p_* r_* \sqrt{\sigma_j} \frac{D_j^2}{r_j^2} e^{-2\alpha_w r_j} \cos(\omega t - \phi_j) \tag{5.23}$$

where p_* is a reference pressure, r_* is a reference distance, σ_j is the backscatter cross-section for the jth particle and $p_* r_* \sqrt{\sigma_j}$ is set to unity. In addition, ω is the angular frequency, D_j is the transducer directivity, r_j is the distance from the transducer to the particle center and ϕ_j is the phase difference between the ray path to particle j and that

to the particle at the origin. The attenuation of sound through the water column, α_w, is taken into account (*Medwin*, 2005, Eq. 2.73 for 1.2 MHz in 20°C fresh water). For each particle, the backscattered return was shifted in time based on the distance from the transmit transducer to the particle. Returns from the particles within the transducer's frequency-dependent circular footprint are summed in time and the two-way travel times converted to range using the water sound speed, c_w. The summed amplitudes were then range-gated by taking the rms value of the amplitude within bins sized $c_w\tau_p/2 = 1.1$ mm, which is the same size as the bins for the MFDop measurements.

The range-gated backscatter amplitude predicted by the model is plotted in Fig. 5.12a. The range to the sediment-water interface, η, given by the mean distance to the particles, lies above the range to the maximum amplitude. This result is due to the fact that the number of particles in any given constant-width annulus on the surface increases with increasing r_j. The synthetic profile can be compared to the averaged backscattered amplitude measured by the MFDop center transducer given in Fig. 5.12b. Similar to the model, the average height of the sediment-water interface lies above the peak amplitude from the surface particles, validating the choice of amplitude threshold for identifying the range to the sediment-water interface.

5.7.2 Possible biases due to beam geometry

A potential concern is the contamination of the amplitude returns from the signal sidelobes at the interfaces. The polar angle to the peak of the first sidelobe, β_s, is 5.3° at 1.2 MHz (*Hare and Hay*, 2020b, Table II). Let R_1 be the vertical distance between the MFDop center transducer and the sediment-water interface and $R_2 = R_1/\cos(\beta_s)$, which represents the distance from the sidelobe to the sediment-water interface. For two-way travel and $R_1 = 0.136$ m (the range to sediment-water interface for G), the contamination from the sidelobe return from the sediment-water interface would come later at a range of $2R_2 - 2R_1 = 1.16$ mm, almost equal to the bin width. However, the square of the directivity at the sidelobe angle is 1.7% of that at the centre of the main lobe and therefore should have less impact than the stronger returns from the main lobe from within the moving layer. In comparison, the contamination from the half width of the main lobe at 1.2 MHz is 0.6 mm, i.e. about half the bin size, and so main lobe returns would be contained within 1 bin for the pulse lengths used here. For the chute bottom, any sidelobe return would come later and therefore would not affect the returns from within the moving layer.

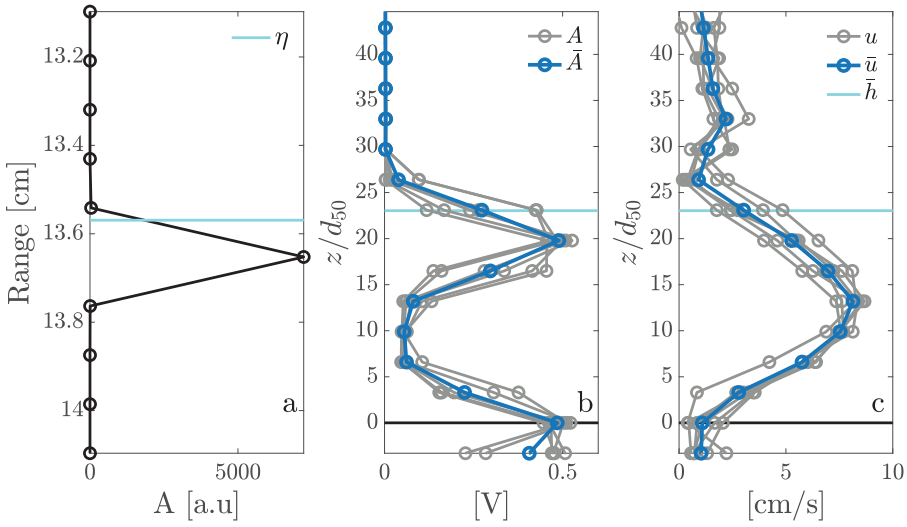

Figure 5.12: (a) Range-gated backscatter amplitude predicted by the quasi-2D single-scattering reflection model described in Chap. 4 (*Hare and Hay*, 2020b) for G at 1.2 MHz. The specified range to the sediment-water interface, η, is given by the cyan line. Vertical profiles of A (b) and u (c) measured with the MFDop and averaged over the 5 s window for 6 repeat G trials (grey), where z has been normalized by the median grain diameter, d_{50}. The velocity, $\bar{u}$, backscatter amplitude, $\bar{A}$, and height of the sediment-water interface, $\bar{h}$, averaged over the 6 repeat trials are indicated. The black line is the chute bottom.

Another potential concern is the contamination of the velocities within range bins just above a strongly-reflecting interface due to the path of least time taken by the interface-reflected pulse to an outboard transducer compared to that for the centre transducer due to the MFDop transducer geometry (*Hay et al.*, 2012; *Hare et al.*, 2014). For the current version of the MFDop with 5° bisector angles and for $r_D = 14.4$ cm (Table 5.1), the path of least time taken by the interface-reflected pulse to an outboard transducer is shorter by 0.5 mm than that for the centre transducer. Thus, the width of the interface contamination zone is small compared to the bin width and should not affect the velocity measurements one bin above the interfaces. This is one of the reasons 5° was chosen for the MFDop bistatic angle for these experiments. However, within one bin close to a strongly reflecting interface, the velocities will be contaminated.

In Fig. 5.12c, u at the chute bottom is not quite zero. This result is due to the finite bin size ($3.3d_{50}$ for G), where the velocities right at the chute bottom are being contaminated by the very small velocities of the particles just above the bottom as well as the bottom contamination described above.

5.7.3 *Bagnold* (1954)

The results reported by *Bagnold* in his 1954 paper have been revisited by *Hunt et al*. (2002), pointing out that the height-to-gap ratio of the test section in *Bagnold*'s concentric rotating cylinders was smaller than it should have been – given previous work with fluids free of particles – to be fully assured that the torque from the end caps would not have contributed significantly to the dynamic balance. Based in part on numerical simulations, *Hunt et al*. (2002) concluded that the end plates would have generated a secondary circulation in the annulus which would have significantly affected *Bagnold*'s measurements especially at high rotational speeds, corresponding to the grain-inertia regime. However, *Hunt et al*. (2002) concluded that the effects of the end cap boundary layers would have been small at the low Reynolds number (Re< 100) corresponding to the macro-viscous regime. Given the very low Reynolds numbers (Table 5.3), Eq. 5.2 should be applicable for the conditions in the experiments presented here.

The predicted porosities and viscosities depend on the value used for the maximum possible static concentration, ϕ_0. For the depth-averaged porosity estimates from the constant density model (Table 5.3), $\phi_0 = 0.6$. Theoretically, the maximum value of ϕ_0 is 0.74 for perfect spheres in a rhombohedral packing arrangement (*Graton and Fraser*, 1935). However, in order for the model predictions of n to be larger or equal to the measured porosity of the stationary sediment, ϕ_0 had to be less than 0.67 for G and less than 0.63 for $S2$. For values of ϕ_0 ranging from 0.55 to these maximum possible values of ϕ_0, the predicted porosity varies by 28% for G and 18% for $S2$.

Bagnold (1954) argued that his relation should be applicable to granular flow down an incline. However, the confining pressure in *Bagnold*'s experiments was provided by the flexible wall of the inner cylinder in his apparatus, whereas the only confining pressure in the present experiments is due to the immersed weight of the grains.

5.7.4 Comparison to previous work

Assuming hydrostatic conditions (the case here because the flow is steady, and $w \sim 0$ within the moving layer), the effective normal stress is given by

$$P_g = \hat{\rho} g \cos \alpha_c (h - z). \tag{5.24}$$

Several groups investigating granular flow dynamics (e.g. *MiDi* (2004); *Cassar et al*. (2005); *Forterre and Pouliquen* (2008)) have adopted an empirical approach that relates P_g to the shear stress: e.g., $\tau = P_g \mu_I(I)$, where μ_I is a friction coefficient depending on the inertial number, I, a dimensionless parameter. In the viscous regime, *Cassar et al*. (2005) propose that the viscous number, I_v, given by

$$I_v = \frac{|\gamma| \mu_w}{\alpha_p P_g} \tag{5.25}$$

should be used instead of I. For steady uniform flows on an inclined plane, *Cassar et al*. (2005) concluded that $\mu_I = \tau / P_g = \tan \alpha_c$ and is therefore constant with I_v being independent of z, yielding

$$u(z) = \frac{I_v \alpha_p}{\mu_w} \hat{\rho} g \cos \alpha_c (h - z/2) z. \tag{5.26}$$

Eq. 5.26 is parabolic but, unlike Eq. 5.17, does not have a velocity maximum for $z < h$ because friction at the sediment-water interface is not taken into account. *Cassar et al*. (2005) were able to measure only the surface velocity and could not observe the vertical structure of the flow within the moving layer.

Courrech du Pont et al. (2003) show that the viscous regime is defined for values of the Stokes number much smaller than 1 and for the square-root of the density ratio to be much greater than the Stokes number. The Stokes number, a non-dimensional parameter representing the relative importance of fluid viscous and grain inertia effects, is given by (*Courrech du Pont et al*., 2003; *Cassar et al*., 2005)

$$\mathrm{St} = \left(\frac{2}{3} \right)^{1/2} \frac{\alpha_p d_{50} \sqrt{\rho_s P_g}}{\mu_w} \tag{5.27}$$

where α_p is a constant related to the permeability of the medium. *Cassar et al*. (2005) used the value of 0.01 for their glass bead experiments based on the upper limit proposed by the literature. For the present glass bead trials, the Stokes number (Eq. 5.27 with Eq. 5.24 using the depth-averaged porosity n listed in Table 5.3) is less than 0.02 throughout the moving layer, indicating that the flow was in the viscous regime. In addition, values of I_v, computed using the MFDop shear rate, were less than 0.04 within the moving layer.

5.7.5 Future work

The model fits to the observed velocity profile involve the parameter ζ, which is a function of both the density and effective viscosity in the moving layer (Eq. 5.18). To properly test *Bagnold* (1954)'s and/or any alternative relation, independent measurements of the porosity would be needed. Acoustics could offer two possible approaches, in principle at least. Porosity could potentially be estimated from changes – between the moving and motionless states – in the amplitude of the sound reflected from the sediment-water interface. However, the reflection coefficient is a function of both the porosity and surface roughness (*Hare and Hay*, 2020b), so the change in surface roughness between moving and motionless sediment would also need to be measured. Alternatively, the attenuation of sound also has a dependence on n, and could possibly be estimated from the amplitude of the transmitted sound.

5.8 Summary and Conclusions

Experiments on granular flow down an incline over a fixed roughness bed were carried out in a water-submerged rectangular chute. Glass beads (G) and natural sand ($S2$) with median diameters of 336 μm and 406 μm were used. The chute was secured at an angle of 27.1° for G and 32.5° for $S2$. Sediments were released in the upstream portion of the chute, producing a moving layer with a thickness of 23 grain diameters. The velocity profile within the moving layer was measured using a wide bandwidth pulse coherent Doppler profiler (MFDop) operating at 1.2 MHz. The MFDop velocities at the sediment-water interface are comparable to those made with a commercially-available Doppler profiler (Vectrino) operating at 10 MHz. However, velocities deeper within the moving layer could not be resolved with the Vectrino due to attenuation at the higher transmit frequency. Velocity profiles obtained with video imagery through the chute sidewall indicate much slower flow speeds and a velocity maximum at the sediment-water interface. Both effects are attributed to sidewall friction.

The measured MFDop velocity profile has a parabolic shape similar to Poiseuille flow, except that the flow at the upper boundary – i.e., the sediment-water interface – is non-zero. Using a constant density model, good agreement is found between the predicted and measured velocity profile. Given this good agreement, we conclude that the granular flows studied here can be considered an incompressible continuous fluid with

bulk properties depending on the concentration of the grains, i.e. the shear stress equals the effective viscosity of the water-saturated granular media multiplied by the shear rate. The parabolic fit for the sand was not quite as good as that for the glass beads, likely due to the rougher surfaces and irregular shapes of the sand grains compared to the glass beads. Using *Bagnold* (1954)'s expression for effective viscosity for the macro-viscous regime, predictions of the depth-averaged porosity and viscosity of the moving layer were obtained. The model-predicted depth-averaged porosity is larger than that measured for the stationary granular material. The predicted depth-averaged viscosity of the moving layer was 409 and 1115 times larger than that of water for G and $S2$, respectively. Results from a variable density model were consistent with the results from the constant density model and showed that the structure in the predicted profiles of n and μ_e were driven by shear. The Bagnold number was generally less than 40, confirming that the flow was in *Bagnold* (1954)'s micro-viscous regime. Reynolds numbers and Reynolds stress were low, signifying that turbulence does not play a dominate role in the flow dynamics.

5.9 Acknowledgements

We thank Richard Cheel for technical assistance. This work was funded by the Natural Sciences and Engineering Research Council of Canada through an Alexander Graham Bell Canada Graduate Scholarship (CGS-D) to J. H. and a Discovery Grant to A. E. H.

5.10 Supplementary Material

Vertical profiles of Reynolds stress, $-\overline{u'w'}$ where the overbar denotes a time average and primes denote fluctuations about the 5 s mean, were estimated from the MFDop and Vectrino data. The results for the glass bead trials are presented in Fig. 5.13. The profiles exhibit little consistent variation with height. The value at the sediment-water interface is 0.06 $\mathrm{cm}^2/\mathrm{s}^2$ and 0.001 $\mathrm{cm}^2/\mathrm{s}^2$ estimated from the MFDop and Vectrino measurements, respectively.

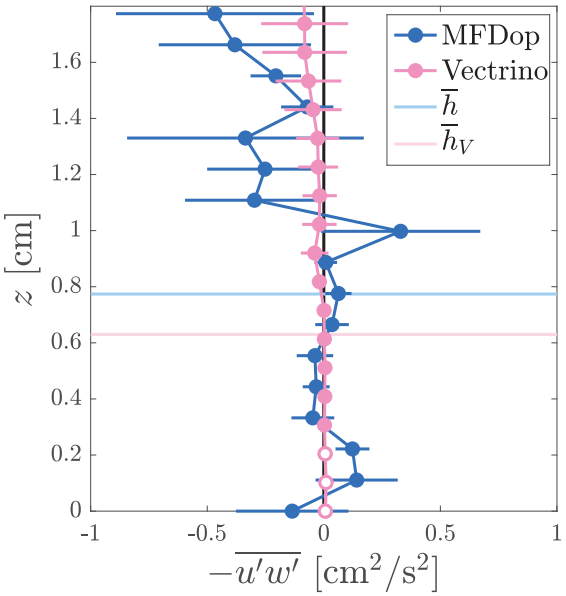

Figure 5.13: Vertical profiles of Reynolds stress computed from the MFDop and Vectrino measurements averaged over 6 repeat G trials. Erroneous Vectrino data are indicated by the open circles. The error bars are ± 1 standard deviation. The mean thickness of the moving layer measured by the MFDop and Vectrino are indicated by the light blue and pink lines, respectively.

CHAPTER 6

CONCLUSIONS

The results presented in this thesis can be divided into two parts: laboratory measurements of (1) the geoacoustic properties of water-saturated granular sediments at MHz frequencies and (2) the vertical structure of sub-aqueous gravity-driven granular flows. In the first part of the thesis, measurements of the attenuation, phase speed and group speed within water-saturated granular sediments, as well as the reflection coefficient at the sediment-water interface are presented. The measurements were made in the scattering regime over 1.0 to 2.0 MHz frequency range, corresponding to $0.5 < ka < 1.2$, where k is the acoustic wave number in water and a is the median grain radius. The granular materials used were natural sand and glass beads. In the second part of the thesis, granular flows down an incline were carried out in a water-submerged rectangular chute by releasing sediments from a cofferdam located upslope, producing a layer with a thickness of O(1) cm moving at O(10) cm/s. Measurements were made for granular flows over a fixed roughness bed and over an erodible bed of like material. Vertical profiles of downslope velocity were obtained remotely using a wideband pulse-coherent acoustic Doppler profiler (MF-Dop). The results are compared to measurements from a commercially-available Doppler profiler (Vectrino) and from side-view and top-view video cameras.

These datasets are used to address the following objectives: (1) determine the size/frequency-dependence of the geoacoustic properties of water-saturated granular sediments, (2) investigate the dependence of these properties on particle concentration and (3) characterize the internal structure of velocity within gravity-driven sub-aqueous granular flows over fixed roughness and erodible beds.

6.1 Key Findings and Implications

1. **Sound speed and attenuation versus the multiple scattering prediction of *Schwartz and Plona* (1984)**

   Attenuation and group speed in water-saturated natural sand and glass beads were measured for $0.5 < ka < 1$ using a single in-water transducer in a monostatic reflection geometry (Chap. 2). The results are consistent with reported measurements made in the more traditional transmission geometry using two transducers. The phase speed estimates, which were based on travel times through granular layers with one in-water transducer and one buried transducer, are consistent with previously reported data (Chap. 3). The measurements confirm the $(ka)^4$ dependence of attenuation and the negative dispersion of phase and group speeds predicted by the multiple scattering theory of *Schwartz and Plona* (1984) for $ka \gtrsim 0.5$.

   The thesis has validated the use of the monostatic geometry for measuring attenuation, which enabled the design of the chute experiments. The measured attenuation coefficients at 1.2 MHz indicate an e-folding scale (accounting for two-way travel) of 1.4 cm for stationary glass beads (Chap. 2). For the granular flow measurements over a fixed roughness bed presented in the thesis, the thickness of the moving layer was $\sim$1 cm, implying that it was thin enough to be probed acoustically at the transmit frequency of 1.2 MHz.

2. **The dependence of sound speed and attenuation on porosity**

   Group and phase speed measurements in water-saturated granular materials are compared to estimates from the literature for $ka \gtrsim 0.2$ (Chaps. 2 and 3). A scaling factor Ψ depending only on porosity and the densities of water and sediment grains is introduced. Scaling by Ψ is shown to reduce the spread among the group and phase speeds by factors of $\sim$3 and $\sim$2, respectively. Most of the collapse is attributed to differences in porosity. Evidence is presented indicating that the remaining spread among the Ψ-scaled phase speed measurements is likely due to uncertainty in sediment porosity arising from the methods used to compact the sediments. Similarly, the scatter among the present and previously reported attenuation measurements for $0.03 < ka < 10$ is greatly reduced when dividing by the solid volume fraction (Appendix D), implying that the attenuation is linearly dependent

on particle concentration (i.e., porosity) to first order.

This is the first time that all reported estimates of attenuation and sound speed for $ka \gtrsim 0.1$ have been collected together. The collapse of these data sets in non-dimensional space has allowed inferences to be made on the dependence of sound propagation on frequency, grain size and particle concentration in sand-sized granular materials at MHz frequencies. These results can be used to validate and improve multiple scattering models. In addition, the insight provided on the concentration dependence of attenuation is of use for inverting backscatter measurements to concentration estimates, especially for obtaining concentration profiles within granular flows.

3. **The size/frequency-dependence of the reflection coefficient versus *Eckart* (1953)'s prediction.**

   Reflection from the sediment-water interface is investigated at frequencies from 1.2 to 2.0 MHz using a broadband narrow-beam transducer at near-normal incidence (Chap. 4). The roughness of the sediment-water interface was measured using side-on, high-resolution photographs of the interface. The resulting bed elevation distributions are Gaussian with roughness parameters close to 1, indicating that the reflected pressure field is mainly due to coherent scattering. The measured reflection coefficients are consistent with the prediction of *Eckart* (1953) for a rough surface with Gaussian-distributed surface elevations.

   Few measurements exist of the reflection coefficient for ka values of order unity. This thesis presents new reflection measurements as well as estimates of the roughness of the sediment-water interface, allowing comparison to be made to *Eckart*'s model. To my knowledge, the *Eckart* model has not been previously applied to reflection at normal incidence from sand-sized granular sediments at wavelengths comparable to the grain size. Given that the *Eckart* model accounts for much of the observed size/frequency-dependence of the reflection coefficient in this range of ka, the model can be used to interpret acoustic returns in other conditions, including field experiments.

4. **A single-scattering model of backscatter from sub-aqueous granular interfaces: the probability distribution of amplitude and decorrelation lengths**

A single-scattering model of reflection from the surface of a granular medium at wavelengths comparable to the grain diameter was developed and is shown to reproduce the observed Gaussian distribution of the reflected amplitude (Chap. 4). The model also reproduces the observed oscillatory variations in the amplitude of the reflected pulse as the transducer was translated horizontally and the associated decorrelation length scales: i.e, $\sim$20% of the transducer diameter, independent of grain size or acoustic frequency. This behaviour is a consequence of speckle in the reflected amplitude field.

This is the first time that the decorrelation length has been investigated for the surface of a granular medium and that the spatial variations in the amplitude of the reflected pressure field have been attributed to speckle. These results increase our understanding of reflection from rough granular surfaces, which is also of interest to other fields such as the medical field (e.g. ultrasound imaging systems).

5. **Vertical velocity profiles within a flowing granular layer**

Vertical profiles of velocity within a gravity-driven granular layer over a fixed roughness bed were obtained with the MFDop operating at 1.2 MHz (Chap. 5). The MFDop measurements in the upper part of the flow are consistent with measurements from the Vectrino operating at 10 MHz, and with particle imaging velocimetry estimates obtained with a top-view video camera. The velocities deeper within the moving layer could not be resolved with the Vectrino due to attenuation at its higher transmit frequency. Shear layers are present above and below a velocity maximum within the moving layer. The MFDop downslope velocities tend towards zero close to the chute bottom as expected.

Compared to field or large-scale flume experiments, the use of the chute allowed for a detailed exploration of granular flows as well as better control over the experimental conditions. The thesis shows that measurements of the internal velocity structure within a moving sediment layer can be achieved at high spatial and temporal resolution using a wideband pulse-coherent Doppler profiler. This is the first time that such measurements are made for gravity-driven granular flows using sediment with densities similar to that of sand. Not only do these results validate the use of acoustics for measuring granular flows, but they also provide the basis for

making acoustic measurements of sediment flowing over like materials.

6. **Porosity and effective viscosity within a sub-aqueous gravity-driven granular flow**

   Good agreement is obtained between the observed velocity profile and that predicted from an analytic low Reynolds number viscous fluid model with constant density. The porosity and effective viscosity within the moving layer are estimated using *Bagnold* (1954)'s semi-empirical relation for the effective viscosity in the macro-viscous regime. The model-predicted depth-averaged porosity is larger than that measured for the stationary granular material, consistent with the moving layer being more dilute due to shear-induced dilation. Results from a variable density model indicate that viscosity and porosity are nearly independent of depth within the moving layer, consistent with the predictions from the constant density model.

   These granular flow results increase our understanding of the grain-scale physics that regulate these types of flows, which can be used to validate numerical models.

7. **Vertical profiles of velocity within a granular flow above an erodible bed.**

   Vertical profiles of downslope velocity within a gravity-driven granular layer flowing over a bed of like material are presented in Appendix C. Similar to the fixed roughness bed case, the downslope velocity profile exhibit a maximum bounded above and below by zones of negative and positive shear. However, in the erodible bed case, the velocities are non-zero below the initial undisturbed bed level ($z = 0$), signifying that the deeper granular material was moving due to the shear stress applied by the particles above. In addition, the maximum velocity within the layer is lower in the erodible bed case.

   These chute experiments of gravity-driven granular flows moving over like materials are particularly relevant to making acoustic measurements of sediment transport in high concentration bedload conditions, e.g. sheet flow. For these thin granular flows, the range resolution would have to be increased by decreasing the pulse length allowing higher frequencies to be used. However, when choosing the transmit frequency for a given grain size, there is a trade-off between range resolution and the depth of penetration of the acoustic signal given the $(ka)^4$ dependence of attenuation.

8. **The roughness of the sediment-water interface of a granular flow**
   The roughness of the sediment-water interface of a moving layer, measured via side-on video imagery, is larger than that for stationary sediment, implying that the reflection coefficient would be lower for the moving layer (Appendix B).

9. **Sound attenuation in a moving layer of granular material**
   In Appendix D, transmission measurements through a moving layer of glass beads are used to obtain an estimate of sound attenuation of 31.6 Np/m. This estimate is lower than the measured value of 37 Np/m for stationary glass beads, consistent with the moving layer being more dilute. The two-way e-folding scale for the moving glass bead layer is 1.6 cm, compared to 1.4 cm for the stationary sediment. This result indicates that the acoustically detectable thickness of sediment is larger for moving sediment, as expected.

6.2 Future Work

In the chute experiments, porosity and effective viscosity within the moving layer are estimated using *Bagnold* (1954)'s relationship, which are based on his sheared annulus experiments where the confining pressure on the particles was provided by the flexible wall of the inner cylinder. In the chute experiments, the confining pressure is due to the immersed weight of the grains. Thus, to properly test the applicability of *Bagnold* (1954)'s relationship for gravity-driven granular flows, independent measurements of the particle concentration within the moving layer are needed. Since sound attenuation has a dependence on concentration, the next steps would include inverting the range-dependent acoustic measurements to concentration profiles. The preliminary results of this study (Appendix D) are promising. Given the frequency-dependence of attenuation, it is expected that the use of multiple frequencies would be useful. The acoustically obtained concentration profiles within the moving layer could be compared to estimates made using other non-invasive or minimally invasive technologies. Good agreement between acoustic and conductivity probe measurements has already been found in sheet flow conditions (*Fromant et al.*, 2018), but using lightweight plastic mm-sized particles, not sand. Another concentration estimate could be obtained using X-ray tomography.

Attenuation measurements at different particle concentrations over $0.5 \lesssim ka \lesssim 1.5$ are needed, especially given the $(ka)^4$ dependence of attenuation in this region. New measurements of α in a fluidized bed set-up – similar to that used by *Argo IV* (2012) – over this ka range and over a wide range of volume concentrations should be made. These measurements would be used to validate models of attenuation in high-concentration suspensions for implementation in algorithms for inverting backscatter amplitude to concentration.

The phase speed and attenuation measurements, and most of those reported in the literature, were made using sediments with narrow grain size distributions. Phase speed and attenuation measurements in bimodal grain size distribution for glass beads have been reported (*Yang and Seong*, 2018). However, questions remain as to the dependence of sound propagation and reflection in sediments with very broad or multimodal distributions. Measurements in these types of sediments should be made in the scattering regime. In addition, measurements could be made in sediments with mixed mineralogical compositions and in sand-mud mixtures. These new laboratory measurements would help interpret field measurements with complex sediment compositions as well as validate existing multiple scattering theories.

APPENDIX A

SALINE DENSITY CURRENT

Using the chute set-up (Fig. 5.1), an experiment was devised to compare the Vectrino and MFDop velocity measurements in a weakly scattering medium: a saline density current. A saline solution with salinity of 71.7 was prepared by heating a mixture of salt and tap water to 65°C and stirring until the salt was fully dissolved. The solution was allowed to cool before seeding material was added and then poured into the cofferdam. The cofferdam was removed, allowing the solution to flow downslope as a saline density current.

The MFDop and Vectrino data were synchronised by defining $t = 0$ when the backscatter amplitude exceeded a specified threshold, indicating the arrival of the leading edge of the downslope flow. For this data set, 17 consecutive MFDop velocity profiles were averaged together to compensate for the different number of ensemble pulse pairs registered by the MFDop compared to the Vectrino. The MFDop and the Vectrino velocities were then averaged over the same 15 s time window starting at $t = 5$ s. As indicated by Fig. A.1, the averaged vertical profiles of downslope velocity measured by the two instruments are in good agreement.

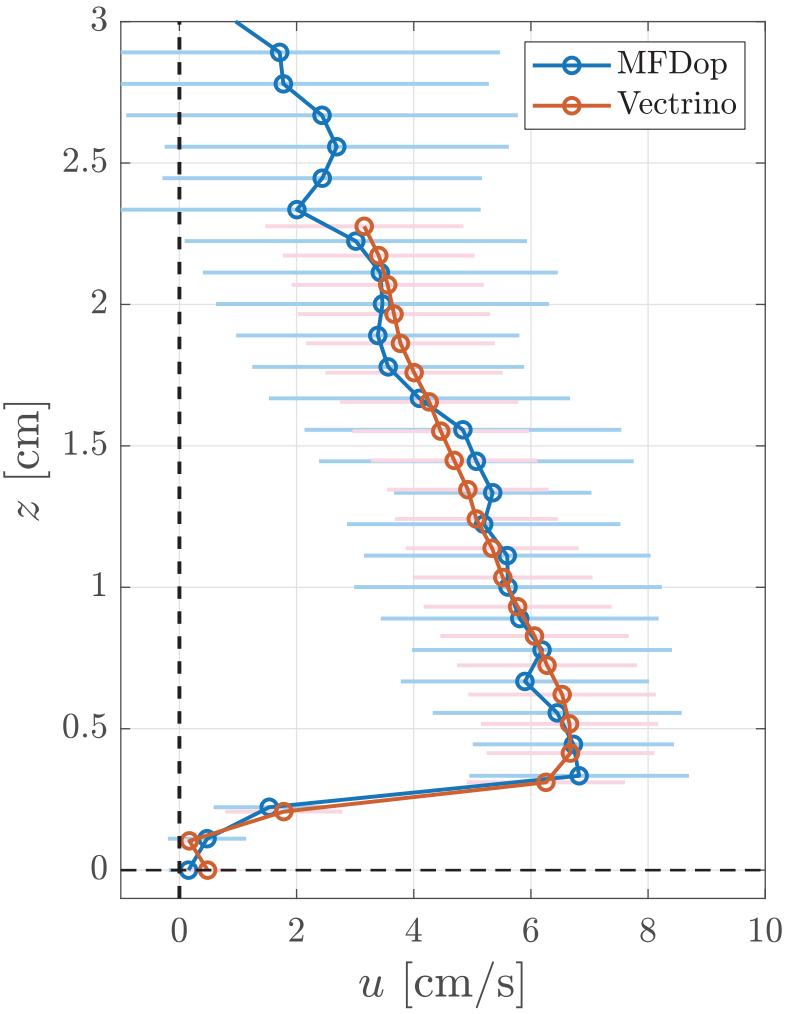

Figure A.1: Vertical profile of the x component of velocity measured by the MFDop and Vectrino for a saline density current. The open circles represent 15 s averages. The error bars are ± 1 standard deviation.

APPENDIX B

SEDIMENT-WATER INTERFACE ROUGHNESS FOR A MOVING LAYER

In Chap. 5, side-view videos of sub-aqueous gravity-driven granular flow down an incline were recorded for the $S2$ sand size. The roughness of the $S2$ sediment-water interface can be determined using the bed elevations computed from each frame recorded by the side-view camera (see Sec. 5.4.3). Only frames corresponding to 5 s after the front passed were used. For each frame, the bed elevation was detrended over 4 mm sections (i.e. $\sim 10d_{50}$). The probability density distribution function (PDF) of the detrended bed elevations for all three repeat trials (totalling 3697 frames) is plotted in Fig. B.1 and compared to a Gaussian function with same variance. The distribution is symmetric about the median value, with a skewness of 0.5 and a kurtosis of 4.4. The roughness, σ_η, given by the standard deviation of all of the detrended segments, was 336 μm, which is 1.7 times the grain radius. The average surface correlation length, L_η, from all segments was 255 μm (see Sec. 4.3.2 for details as to how L_η was computed).

The value of σ_η is 3 times smaller for stationary sand (Table 4.3) than the value measured here for moving sand, however the surface correlation lengths are comparable for both cases. The roughness parameter, g, is given by $(2k\sigma_\eta)^2$, where k is the wavenumber in water. For 1.2 MHz, g equals 1.4 and 11.7 for non-moving and moving $S2$ sand, respectively. Using Eq. 4.9, the ratio of the incoherent intensity term to the coherent intensity term is 0.4% for the value of g for stationary $S2$ sediment, indicating that the return signal was predominately coherent in that case. However, the incoherent intensity term is 21 times larger than the coherent term for moving $S2$ sand, implying that the contribution from incoherent scattering is non-negligible for moving sand. Note that these

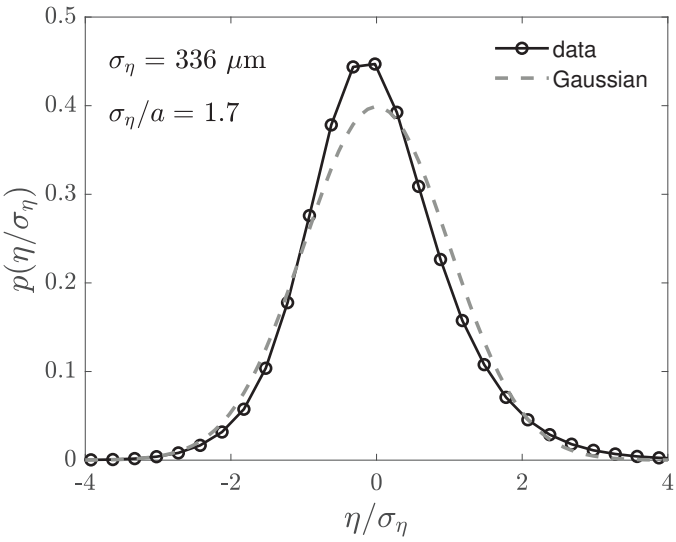

Figure B.1: Probability density distribution of the interface at the top of the moving layer, η, normalised by the standard deviation, σ_η. Only frames corresponding to 5 s after the front passed the measurement point were used. The dashed line is a Gaussian distribution with unity standard deviation.

measurements of surface roughness are based on side-view images and therefore are not representative of the faster flow present in the middle of the chute where the MFDop measurements were made (as discussed in Chap. 5).

APPENDIX C

VELOCITY STRUCTURE IN SUB-AQUEOUS GRANULAR FLOW DOWN A SLOPE: ERODIBLE BED

In Chap. 5, measurements of sub-aqueous granular flow over a fixed roughness bed were presented. Here, measurements of granular flow over an erodible bed of like material are given.

C.1 Methods

The chute set-up for the fixed roughness bed experiment (Fig. 5.1) was modified to include a well for the erodible bed trials (Fig. C.1). The well (15.2 cm long and 2.6 cm deep), located about halfway down the chute, was created by screwing two 2.6 cm thick polyvinyl chloride (PVC) rectangular pieces spanning the width of the chute to the chute bottom. The top sides of the PVC pieces were covered with anti-slip traction tape (Gator Grip). At the start of each erodible bed trial, sediment was poured into the well and a straight edge longer than the well was carefully drawn across so as to obtain a flat sediment-water interface. The coordinate system is given in Fig. C.1, where $z = 0$ is defined as the top of the sediment-water interface of the sediment-filled well. The rest of the procedure for producing the flowing granular layer was the same as that described in Sec. 5.3.

Two types of sediment were used for the erodible bed trials: soda lime glass beads (G) and quartz sand ($S1$), with the sediment properties listed in Table 2.3. The chute was secured at an angle, α_c, equal to 27.1° for G (same as that for the fixed roughness

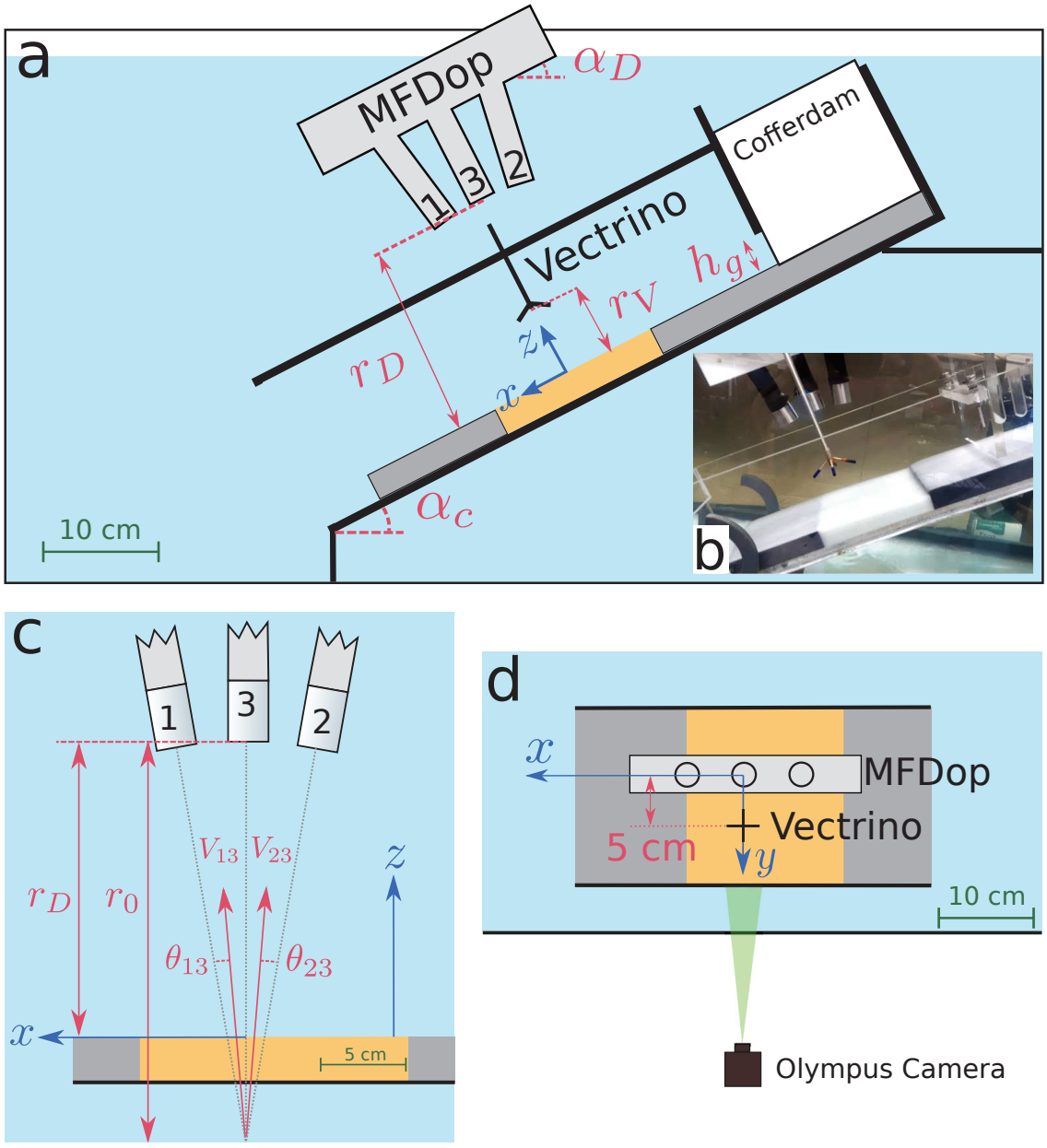

Figure C.1: Experimental set-up: (a) side view of the chute submerged in the water-filled tank and (b) photograph with glass beads in the well. The gray color indicates the PVC blocks. The yellow color indicates the well when filled with sand or glass beads. (c) MFDop geometry, showing the bisector angles, beam velocities and beam intersection point. (d) Top view of the chute looking down the z axis. The chute coordinate system used throughout the paper (x, y, z) is indicated in blue in panels (a), (c) and (d).

trials) and 32.5° for $S1$. Seeding particles (20 μm polyamid particles) were added to the surrounding water and sediment in the same manner as that described for the fixed roughness trials. Seven repeat trials were done for G. Only 1 trial is shown here for the $S1$ sand due to the unsteadiness of the flow.

Velocity measurements were made with the MFDop and Vectrino with the same settings as those for the fixed roughness trials (Sec. 5.3). The Vectrino and MFDop data were collected and analysed as described in Secs. 5.3 and 5.4. For the MFDop data, $z = 0$ was given by one range bin above the range to the maximum amplitude at the beginning of the trial, i.e. before the front passed the measurement point. The vertical distance between $z = 0$ and the MFDop center transducer, r_D, was 14.8 cm for G and 22.9 cm for $S1$. For each trial, the Vectrino data were rotated to chute coordinates as described in Sec. 5.4.5. The average rotation angle over the seven repeat G trials was $4.0° \pm 0.2°$.

C.2 Results

C.2.1 Glass beads

Velocities registered by the Vectrino for a single G trial for the fixed roughness and erodible bed cases are compared in Fig. C.2. In contrast to the fixed roughness trials, velocity fluctuations were observed in the water column, persisting for as long as the granular flow layer was moving. This increased activity in the water column was observed in all repeat erodible bed trials and is due to turbulence and sediment suspension generated at the scour pit formed at the well edge upstream from the measurement point. This scour pit was observed visually in a separate trial using $S1$ sediment without any seeding (Fig. C.3).

The backscatter amplitude in dB (i.e., $20 \log_{10} A$) from the MFDop for a single G trial is shown in Fig. C.4a with 2 s averaged u velocity profiles obtained by the MFDop and Vectrino overlayed. The MFDop profiles show that the flow is quite steady within the moving layer after the passage of the front. Vertical profiles of u and w averaged over a 5 s window and 7 repeat trials are shown in Fig. C.4bc. The height of the sediment-water interface averaged over the 5 s window and then over the repeat trials was 9.96 mm $\pm$ 0.03 mm and 7.9 mm $\pm$ 0.9 mm for the MFDop and Vectrino, respectively.

For the erodible bed trials, the maximum MFDop downslope velocity, $\bar{u}_m$, equals 5.2

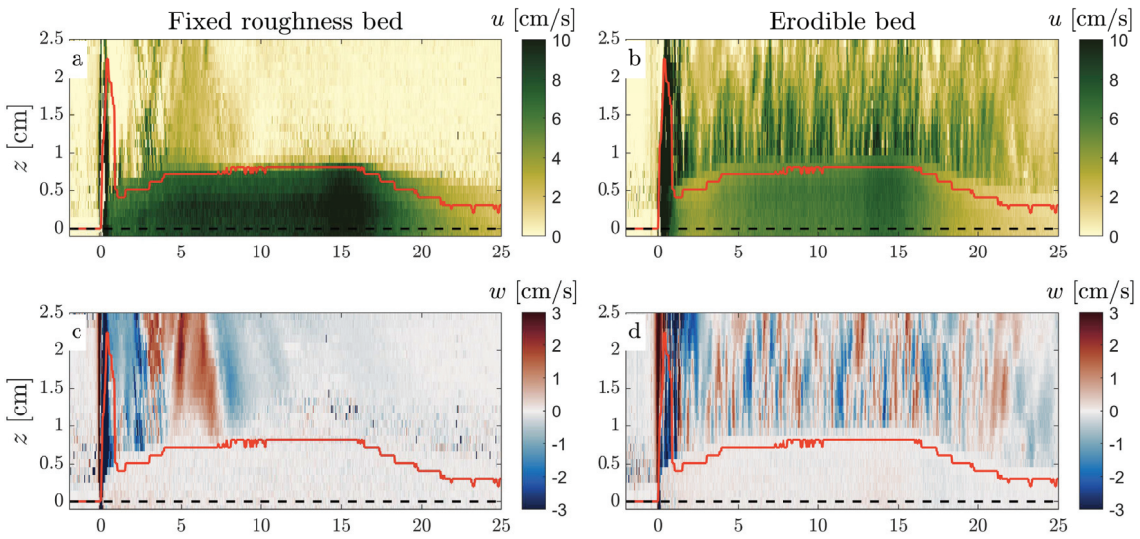

Figure C.2: Velocities measured with the Vectrino for glass beads moving over a fixed roughness (a, c) and erodible (b, d) bed. The sediment-water interface is indicated in red.

Figure C.3: Image taken with the Olympus camera showing the scour pit formed at the upstream end of the well during a $S1$ trial (no seeding in this case). Flow is from right to left. Note the suspended sediment moving in the water column above the bedload layer. For scale, the thickness of the PVC plate is 2.6 cm.

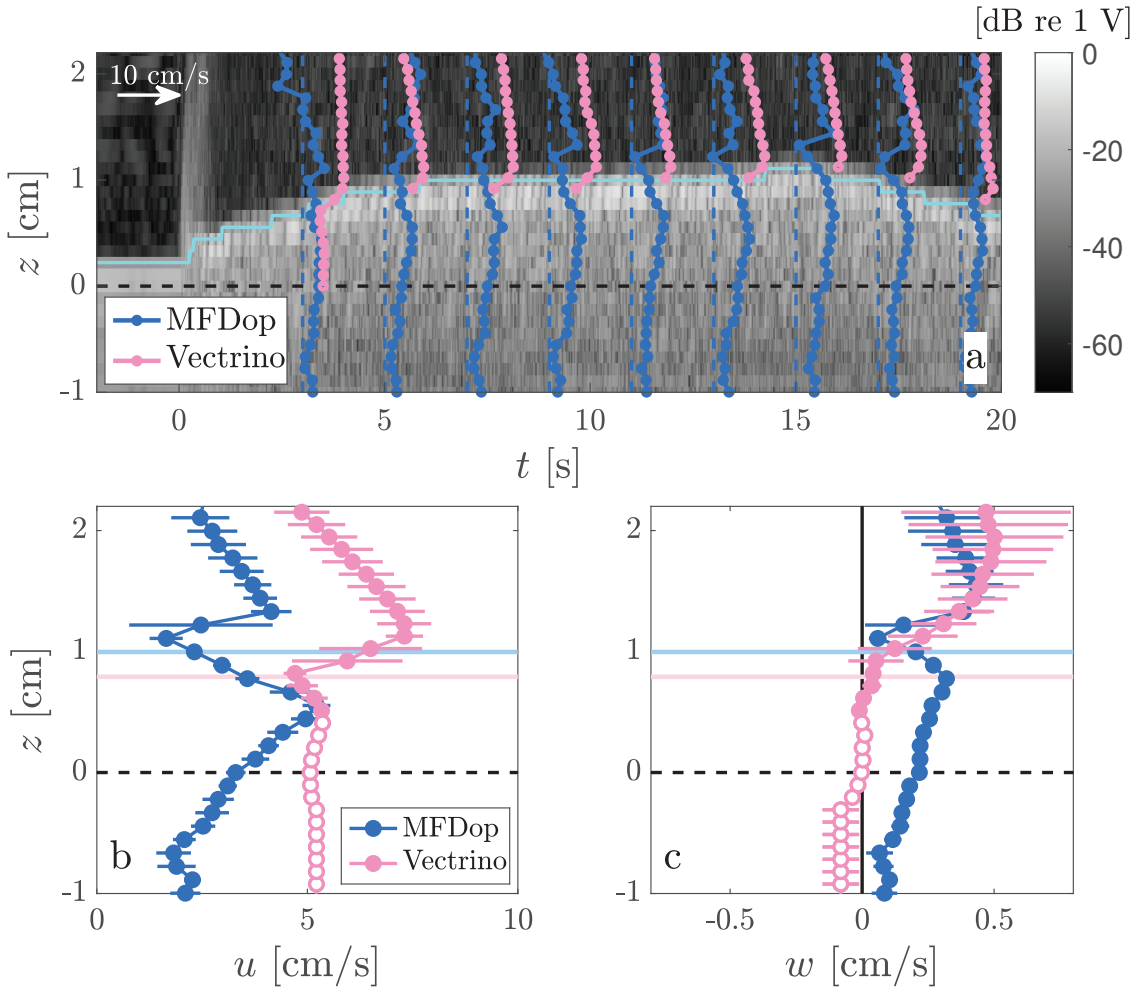

Figure C.4: Same as Fig. 5.7 except for the erodible glass bead bed. The horizontal light blue and pink lines are the mean height of the sediment-water interface estimated from the MFDop and Vectrino measurements, respectively. The horizontal dashed line indicates $z = 0$.

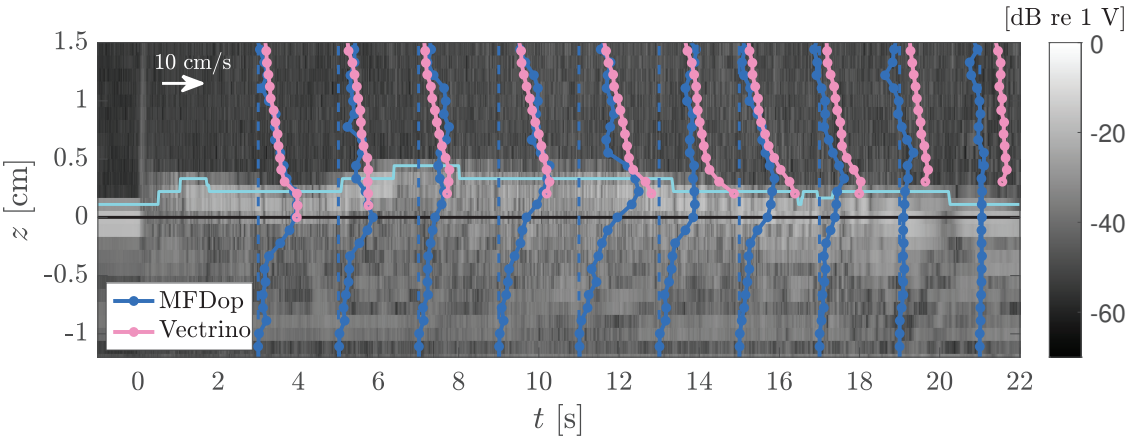

Figure C.5: Backscatter amplitude measured with the MFDop centre transducer for a single $S1$ trial with $S1$ sand in the well. See also caption for Fig. 5.7a.

cm/s and is located a distance of 4.6 mm below the sediment-water interface. These values compare to 8 cm/s and 3.4 mm for the G trials with fixed bed roughness. For the fixed roughness bed trials (Fig. 5.7), u goes to zero at $z = 0$ and w is nearly zero throughout the moving layer. For the erodible bed trials, both the u and w velocities are non-zero below $z = 0$, signifying that the granular material within the well are moving due to the shear stress applied by of particles above. As discussed in Sec. 5.4, the Vectrino velocities measured deeper within the moving layer (i.e. at $z \lesssim z_m$) represent contamination from the sediment-water interface via the sidelobes in the transducer beam pattern. Non-zero water column velocities are registered by both instruments. The larger water u velocities in the water column measured with the Vectrino are likely due to the instrument preferentially picking up returns from smaller, faster moving particles (due to its higher transmit frequency) compared to the MFDop.

C.2.2 Sand

The backscatter amplitude registered by the MFDop center transducer for a single trial of $S1$ flowing over the erodible $S1$ bed is shown in Fig. C.5. For this chute angle, the flow was unsteady. However, for the same chute angle over the fixed roughness bed, the flow was steady and the profiles (not shown) had the similar shapes to those presented in Fig. 5.7a.

APPENDIX D

SUB-AQUEOUS GRANULAR FLOW DOWN A SLOPE: SOUND ATTENUATION

D.1 Previous Reported Measurements

Chap. 2 focused on attenuation measurements as a function of grain size and frequency. However, the porosity n or solid volume fraction $\Phi = 1 - n$ are also important factors to consider (*Urick*, 1948; *Peters and Petit*, 2000). Reported literature data of sound attenuation, α, are plotted in Fig. D.1a and are compared to datasets where α was measured in suspensions of scatterers at different volume concentrations. Note that *Cowan et al*. (1998) suspended glass beads in a 75% glycerol and 25% water mixture, whereas *Busby and Richardson* (1957), *Spelt et al*. (2001) and *Argo IV* (2012) used glass beads in water. Thus, the data reported by *Cowan et al*. (1998) were corrected to remove the glycerol contribution to the attenuation as described below.

The wavenumbers given by *Cowan et al*. (1998) for their fluid mixture, k_{gw}, were transformed to wavenumbers in water, k, using $k = \frac{c_{gw}}{c_w} k_{gw}$ where c_{gw} and c_w are the sound speeds in their fluid and the water, respectively. Next, the attenuation in the water-satured glass beads was calculated by subtracting the contribution of glycerol to the total attenuation α_T and replacing it with the same volume of water: $\alpha = \alpha_T - nm\alpha_g + nm\alpha_w$, where α_w is the attenuation in water (based on equations from *Medwin* (2005)) and m is the fraction of glycerol in the fluid. The attenuation in glycerol is given by (*Hunter*, 1941): $\alpha_g = 8\pi^2\eta_g f^2/(3\rho_g v_g^3)$, where η_g and ρ_g are the dynamic viscosity and density of glycerol. Temperature-dependent expressions for η_g and ρ_g were taken from *Cheng*

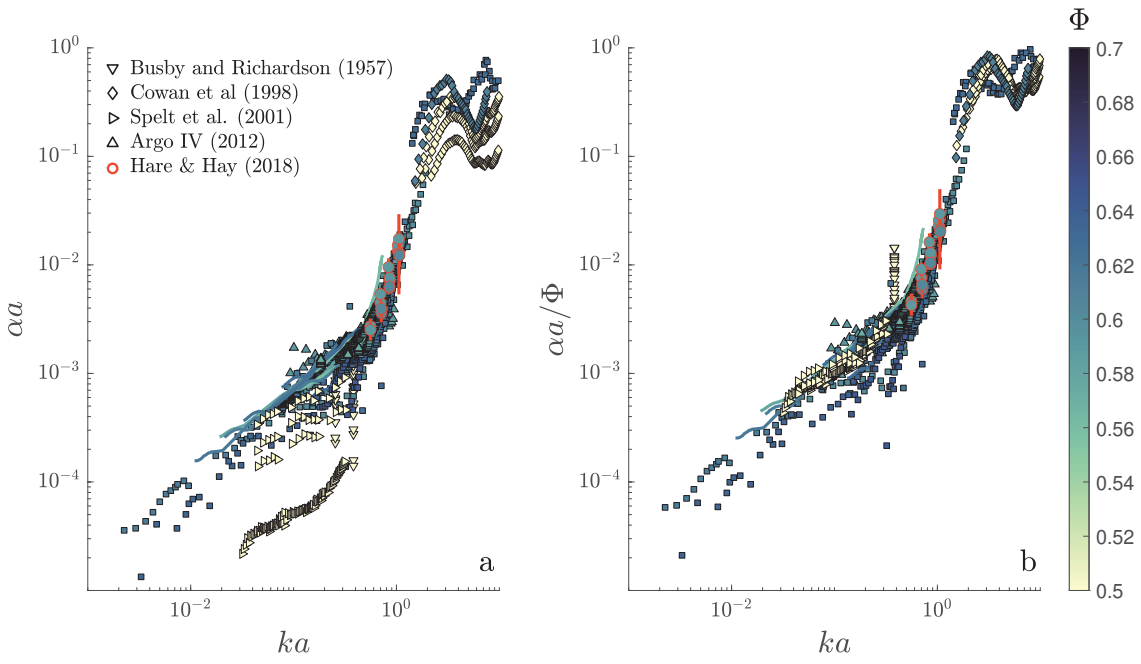

Figure D.1: (a) Attenuation, non-dimensionalized with particle radius a, vs ka and solid particle volume Φ (colour). The squares are the same literature data as Fig. 2.1 with additional data added by *Page et al*. (1996). Reported measurements where the solid fraction was varied are also plotted (*Busby and Richardson*, 1957; *Cowan et al*., 1998; *Argo IV*, 2012; *Spelt et al*., 2001). The circles are the attenuation measurements from *Hare and Hay* (2018). (b) Same data as in (a), but divided by the solid volume fraction.

(2008, Eqs. 22 and 24). The speed of sound in glycerol, v_g, was determined from a linear fit of reported measurements (*Hunter*, 1941; *Fergusson et al*., 1954; *Jeong et al*., 1986) as a function of temperature. The resulting corrections to α are small – less than 3% for the largest volume fraction 0.61 and less than 15% for the smallest volume fraction 0.21 – due to the fact that scattering is the dominant loss mechanism in *Cowan et al*.'s data.

In Fig. D.1b, the attenuation data from Fig. D.1a are divided by the solid volume fraction. It is clear that this scaling leads to a reduction in scatter, indicating that α is, to a first approximation, linearly dependent on solid volume fraction. This result, which suggests that multiple scattering is weak, is rather surprising given the particle volume concentrations in these experiments: i.e. maximum values of 40% for *Spelt et al*. (2001), and 61% for *Cowan et al*. (1998).

D.2 Attenuation within Granular Flow

D.2.1 Methods

To measure the sound attenuation in a granular flow layer, the chute set-up presented in Fig. C.1 was modified by inserting a pinducer (Valpey Fisher, 7 MHz, 1.3 mm diameter) into a hole drilled in the bottom of the well so that its face was parallel to the chute bottom and below the MFDop's center transducer. The height of the pinducer above the chute bottom, δz_p, was equal to 2.2 cm. This height was determined from the backscatter amplitude registered by the MFDop's center transducer for the water-filled well where δz_p is given by the difference between the range to the maximum amplitude (i.e. the chute bottom) and the range to the peak above the chute bottom representing the pinducer.

For these trials, the well was filled with glass beads (G, see Table 2.3) in the same manner as that described in Appendix C, so that the pinducer was covered by a few mm of sediment before the start of a trial. The procedure for producing a granular flowing layer in the chute is the same as that described in Sec. 5.3, except that in this case the chute was secured at a slope angle of 27°, no seeding particles were used and 8 repeat trials were executed. Data were recorded using three instruments: the MFDop, the Vectrino and the pinducer. The MFDop transmitted a tone burst at 1.2 MHz with a duration of 6 μs. The other MFDop and Vectrino settings were the same as those described in Sec. 5.3.

Waveform measurements registered by the pinducer were obtained using a digital oscilloscope sampling at 125 MHz. Three transmit pulses were acquired at 3.7 Hz and

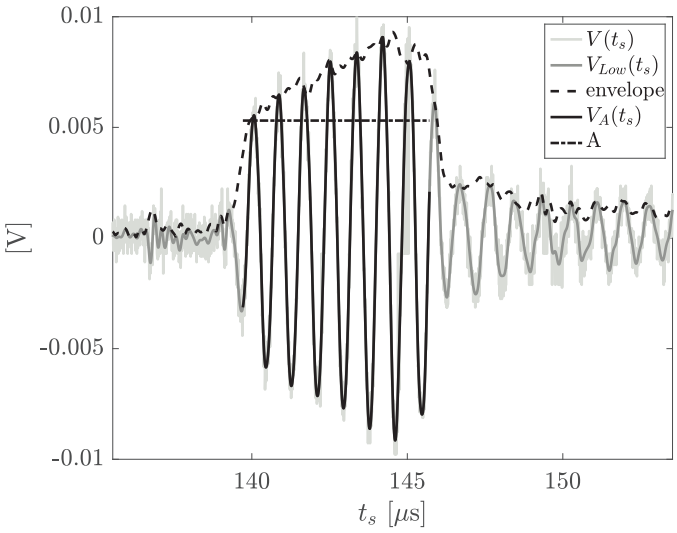

Figure D.2: Ensemble-averaged signal, $V(t_s)$, transmitted through the sediment layer for a single trial. The low-passed filtered signal, $V_{Low}(t_s)$, and envelope are indicated by the dark grey and dashed lines, respectively. The rms amplitude of $V_A(t_s)$ (black line) is given by the black dashed-dotted line.

ensemble-averaged. The ensemble-averaged signals, $V(t_s)$, were then low-passed filtered using a fifth-order Butterworth filter with a 5 MHz cut-off, $V_{Low}(t_s)$, where t_s is the signal travel time. The envelope of $V_{Low}(t_s)$ was obtained via the Hilbert transform. Examples of these signals are shown in Fig. D.2, where the transmitted signal through the sediment layer is highlighted, $V_A(t_s)$. Noise level, N_s, was defined as the rms value of $V(t_s)$ prior to $V_A(t_s)$. $V_A(t_s)$ was defined to start at the first value of the envelope that was larger than $5N_s$ and to end one pulse length later. The rms value of $V_A(t_s)$, designated by A, is used as the measure of the amplitude of the signal transmitted through the sediment. Assuming plane wave propagation, let the amplitude for one-way travel be given by

$$A_1 = A_0 e^{-\alpha h_1} \tag{D.1}$$

where A_1 is the measured amplitude through a sediment layer of thickness h_1, α is the sound attenuation and A_0 is a system-dependent constant, which was given by the rms of the signal recorded when no sediment was in the well.

The range to the sediment-water interface, η_V, was determined from the Vectrino measurements using the procedure described in Sec. 5.4. The thickness of the sediment above the pinducer, $h_p(t)$, was determined from η_V, taking into account δz_p and the range

from the Vectrino's centre transducer to the chute bottom.

The data streams from the Vectrino and pinducer were synchronised by defining $t = 0$ as the arrival of the leading edge of the downslope flow. For the Vectrino data, $t = 0$ was the time when $\eta_V(t)$ exceeded a specified threshold. For the pinducer, this value was given by the time at which the gradient of $A(t)$ reached a maximum.

D.2.2 Results

Let A_s and A_m denote the time-averaged $A(t)$ over times when the sediment was stationary or moving, respectively. For each trial, A_s was given by the average of $A(t)$ for $t \leq -2.7$ s (over 3.5 to 6.2 s depending on the trial), which is well before the arrival of the leading edge of the downslope flow occurring at $t = 0$. For each trial, A_m was given by a 5-s average of $A(t)$ over $3 < t < 8$ s during which the layer thickness was relatively constant. The average u at η_V over the 5 s window and over all repeat trials was 4.8 cm/s $\pm$ 0.3 cm/s.

In Fig. D.3, the time-averaged amplitudes for the stationary and moving sediments, normalised by A_0, are plotted as a function of sediment thickness, h_p. The lower amplitudes associated with the signals transmitted through the moving sediment layer are due to the sound being attenuated in the thicker moving layer. The A_s data points are widely scattered, however a line with slope $-\alpha_s$ (where $\alpha_s = 37$ Np/m is the measured attenuation in stationary glass beads from Chap. 2, see Table 2.6) is representative. The A_m data points are more tightly clustered and the average over 8 repeat trials, $\langle A_m \rangle$, is also plotted in Fig. D.3. For these times, the trial-averaged sediment thickness was $\langle h_{pm} \rangle = 11.4$ mm $\pm$ 0.2 mm. Using Eq. D.1 with $A_1 = \langle A_m \rangle$ and $h_1 = \langle h_{pm} \rangle$, the sound attenuation through the moving layer, α_m, is 31.6 Np/m. This estimate is lower than the measured value of 37 Np/m for stationary glass beads, consistent with the moving layer being more dilute. Given the linear dependence of attenuation on particle concentration (Sec. D.1), the porosity within the moving layer is estimated to be 0.485, which is 5% larger than the estimate from the constant density model listed in Table 5.3.

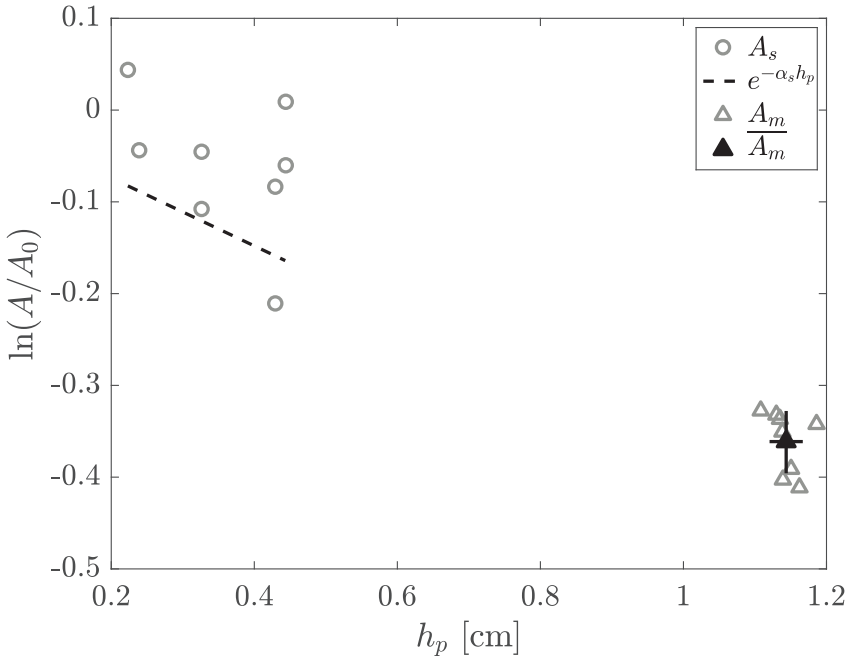

Figure D.3: Transmitted amplitude normalised by A_0 through a layer of glass beads with thickness h_p where circles and triangles denote data for stationary and moving sediment, respectively. The data for each repeat trial are grey markers. The average over all repeat trials for the moving sediment is given by the black triangle with error bars denoting ± 1 standard deviation. The dashed line has a slope of -37 Np/m, the measured attenuation for stationary glass beads (Table 2.6).

APPENDIX E

COPYRIGHT PERMISSIONS

AIP Publishing LLC

Your Window to Possible

Permission to Reuse Content

REUSING AIP PUBLISHING CONTENT

Permission from AIP Publishing is required to:

- republish content (e.g., excerpts, figures, tables) if you are not the author
- modify, adapt, or redraw materials for another publication
- systematically reproduce content
- store or distribute content electronically
- copy content for promotional purposes

To request permission to reuse AIP Publishing content, use RightsLink® for the fastest response or contact AIP Publishing directly at rights@aip.org (mailto:rights@aip.org) and we will respond within one week:

For RightsLink, use Scitation to access the article you wish to license, and click on the Reprints and Permissions link under the TOOLS tab. (For assistance click the "Help" button in the top right corner of the RightsLink page.)

To send a permission request to rights@aip.org (mailto:rights@aip.org), please include the following:

- Citation information for the article containing the material you wish to reuse
- A description of the material you wish to reuse, including figure and/or table numbers
- The title, authors, name of the publisher, and expected publication date of the new work
- The format(s) the new work will appear in (e.g., print, electronic, CD-ROM)
- How the new work will be distributed and whether it will be offered for sale

Authors do **not** need permission from AIP Publishing to:

- quote from a publication (please include the material in quotation marks and provide the customary acknowledgment of the source)
- reuse any materials that are licensed under a Creative Commons CC BY license (please format your credit line: "Author names, Journal Titles, Vol.#, Article ID#, Year of Publication; licensed under a Creative Commons Attribution (CC BY) license.")
- reuse your own AIP Publishing article in your thesis or dissertation (please format your credit line: "Reproduced from [FULL CITATION], with the permission of AIP Publishing")
- reuse content that appears in an AIP Publishing journal for republication in another AIP Publishing journal (please format your credit line: "Reproduced from [FULL CITATION], with the permission of AIP Publishing")
- make multiple copies of articles–although you must contact the Copyright Clearance Center (CCC) at www.copyright.com (http://www.copyright.com/) to do this

BIBLIOGRAPHY

Abbott, J. G., and F. L. Thurstone, Acoustic speckle: Theory and experimental analysis, *Ultrasonic imaging*, *1*, 303–324, 1979.

Ancey, C., Bedload transport: a walk between randomness and determinism. part 1. the state of the art, *J. Hydraul. Res.*, *58*, 1–17, 2020a.

Ancey, C., Bedload transport: a walk between randomness and determinism. part 2. challenges and prospects, *J. Hydraul. Res.*, *58*, 18–33, 2020b.

Argo IV, T. F., Laboratory measurements of sound speed and attenuation of water-saturated granular sediments, Ph.D. thesis, The University of Texas at Austin, 2012.

Argo IV, T. F., M. D. Guild, P. S. Wilson, M. Schröter, C. Radin, and H. L. Swinney, Sound speed in water-saturated glass beads as a function of frequency and porosity, *J. Acoust. Soc. Am.*, *129*, EL101–EL107, 2011.

Aussillous, P., J. Chauchat, M. Pailha, M. Médale, and É. Guazzelli, Investigation of the mobile granular layer in bedload transport by laminar shearing flows, *J. Fluid Mech.*, *736*, 594–615, 2013.

Bagnold, R. A., Experiments on a gravity-free dispersion of large solid spheres in a newtonian fluid under shear, *Proc. R. Soc. Lond. A Math Phys. Sci.*, *225*, 49–63, 1954.

Bagnold, R. A., The flow of cohesionless grains in fluids, *Phil. Trans. Roy. Soc. London A*, *249*, 235–297, 1956.

Bareš, V., Š. Zrostlík, T. Picek, J. Krupička, and V. Matoušek, On local velocity measurement in gravity-driven flows with intense bedload of coarse lightweight particles, *Flow. Meas. Instrum.*, *51*, 68–78, 2016.

Beckmann, P., and A. Spizzichino, *The Scattering of Electromagnetic Waves from Rough Surfaces*, MacMillan, New York, 1963, 503 pp.

Berryman, J. G., Theory of elastic properties of composite materials, *Appl. Phys. Lett.*, *35*, 856–858, 1979.

Berryman, J. G., Long-wavelength propagation in composite elastic media I. Spherical inclusions, *J. Acoust. Soc. Am.*, *68*, 1809–1819, 1980.

Burckhardt, C. B., Speckle in ultrasound B-mode scans, *IEEE T. Son. Ultrason.*, *25*, 1–6, 1978.

Busby, J., and E. G. Richardson, The absorption of sound in sediments, *Geophysics*, *22*, 821–828, 1957.

Cassar, C., M. Nicolas, and O. Pouliquen, Submarine granular flows down inclined planes, *Phys. Fluids*, *17*, 103301, 2005.

Cheng, N.-S., Formula for the viscosity of a glycerol- water mixture, *Ind. Eng. Chem. Res.*, *47*, 3285–3288, 2008.

Chotiros, N. P., Reflection and reverberation in normal incidence echo-sounding, *J. Acoust. Soc. Am.*, *96*, 2921–2929, 1994.

Chotiros, N. P., Biot model of sound propagation in water-saturated sand, *J. Acoust. Soc. Am.*, *97*, 199–214, 1995.

Chotiros, N. P., Acoustic modeling of sandy ocean sediments, in *Proc. Underwater Technol. Conf.*, pp. 231–236, IEEE, 2002.

Chotiros, N. P., and M. J. Isakson, A broadband model of sandy ocean sediments: Biot–stoll with contact squirt flow and shear drag, *J. Acoust. Soc. Am.*, *116*, 2011–2022, 2004.

Chotiros, N. P., A. P. Lyons, J. Osler, and N. G. Pace, Normal incidence reflection loss from a sandy sediment, *J. Acoust. Soc. Am.*, *112*, 1831–1841, 2002.

Clay, C. S., and H. Medwin, *Acoustical Oceanography: Principles and Applications*, New York, NY Wiley-Interscience, 1977.

Courrech du Pont, S., P. Gondret, B. Perrin, and M. Rabaud, Granular avalanches in fluids, *Phys. Rev. Lett.*, *90*, 044301, 2003.

Cowan, M. L., K. Beaty, J. H. Page, Z. Liu, and P. Sheng, Group velocity of acoustic waves in strongly scattering media: Dependence on the volume fraction of scatterers, *Phys. Rev. E*, *58*, 6626, 1998.

Delgado, J. M. P. Q., A simple experimental technique to measure tortuosity in packed beds, *Can. J. Chem. Eng.*, *84*, 651–655, 2006.

Doppler, D., P. Gondret, T. Loiseleux, S. Meyer, and M. Rabaud, Relaxation dynamics of water-immersed granular avalanches, *J. Fluid Mech.*, *577*, 161–181, 2007.

Eckart, C., The scattering of sound from the sea surface, *J. Acoust. Soc. Am.*, *25*, 566–570, 1953.

Fergusson, F. A. A., E. W. Guptill, and A. D. MacDonald, Velocity of sound in glycerol, *J. Acoust. Soc. Am.*, *26*, 67–69, 1954.

Flores, N. Z., and J. F. A. Sleath, Mobile layer in oscillatory sheet flow, *J. Geophys. Res. Oceans*, *103*, 12783–12793, 1998.

Fofonoff, N. P., and R. C. Millard, Algorithms for computation of fundamental properties of seawater, *UNESCO Tech. Pap. Marine Sci.*, *44*, 1–53, 1983.

Forterre, Y., and O. Pouliquen, Flows of dense granular media, *Annu. Rev. Fluid Mech.*, *40*, 1–24, 2008.

Fredsoe, J., and R. Deigaard, *Mechanics of Coastal Sediment Transport*, World Scientific, 1992, 369 pp.

Fromant, G., R. S. Mieras, T. Revil-Baudard, J. A. Puleo, D. Hurther, and J. Chauchat, On bedload and suspended load measurement performances in sheet flows using acoustic and conductivity profilers, *J. Geophys. Res.-Earth*, *123*, 2546–2562, 2018.

Gonzalez, R. C., R. E. Woods, and S. L. Eddins, *Digital Image Processing using MATLAB*, Pearson Education India, 2004.

Goodman, J. W., Some fundamental properties of speckle, *J. Opt. Soc. Am.*, *66*, 1145–1150, 1976.

Graton, L. C., and H. J. Fraser, Systematic packing of spheres: With particular relation to porosity and permeability, *J. Geol.*, *43*, 785–909, 1935.

Hamilton, E. L., G. Shumway, H. W. Menard, and C. J. Shipek, Acoustic and other physical properties of shallow-water sediments off San Diego, *J. Acoust. Soc. Am.*, *28*, 1–15, 1956.

Hanes, D. M., and D. L. Inman, Observations of rapidly flowing granular-fluid materials, *J. Fluid Mech.*, *150*, 357–380, 1985.

Hare, J., and A. E. Hay, Attenuation and group speed in water-saturated granular materials at MHz frequencies, *J. Acoust. Soc. Am.*, *143*, 2744–2755, 2018.

Hare, J., and A. E. Hay, Phase speed in water-saturated sand and glass beads at MHz frequencies, *J. Acoust. Soc. Am.*, *148*, 2301–2310, 2020a.

Hare, J., and A. E. Hay, On acoustic reflection from sand-sized water-saturated granular media at MHz frequencies: Measurements, models and the role of speckle, *J. Acoust. Soc. Am.*, *148*, 3291–3304, 2020b.

Hare, J., A. E. Hay, L. Zedel, and R. Cheel, Observations of the space-time structure of flow and stress over orbital-scale ripples, *J. Geophys. Res.*, *119.3*, 1876–1898, 2014.

Hay, A. E., L. Zedel, R. Cheel, and J. Dillon, Observations of the vertical structure of turbulent oscillatory boundary layers above fixed roughness beds using a prototype wideband coherent Doppler profiler: 1. The oscillatory component of the flow, *J. Geophys. Res.*, *117*, 2012.

Hay, A. E., L. Zedel, and N. Stark, Sediment dynamics on a steep, megatidal, mixed sand-gravel-cobble beach, *Earth Surf. Dyn.*, *2*, 443, 2014.

Hefner, B. T., D. R. Jackson, K. L. Williams, and E. I. Thorsos, Mid-to high-frequency acoustic penetration and propagation measurements in a sandy sediment, *IEEE J. Ocean. Eng*, *34*, 372–387, 2009.

Hipp, A. K., G. Storti, and M. Morbidelli, On multiple-particle effects in the acoustic characterization of colloidal dispersions, *J. Phys. D: Appl. Phys.*, *32*, 568–576, 1999.

Houssais, M., C. P. Ortiz, D. J. Durian, and D. J. Jerolmack, Onset of sediment transport is a continuous transition driven by fluid shear and granular creep, *Nat. Commun.*, *6*, 2015.

Hunt, M. L., R. Zenit, C. S. Campbell, and C. E. Brennen, Revisiting the 1954 suspension experiments of R. A. Bagnold, *J. Fluid Mech.*, *452*, 1–24, 2002.

Hunter, J. L., The absorption of ultrasonic waves in highly viscous liquids, *J. Acoust. Soc. Am.*, *13*, 36–40, 1941.

Hurther, D., and U. Lemmin, Improved turbulence profiling with field-adapted acoustic doppler velocimeters using a bifrequency doppler noise suppression method, *J. Atmos. Oceanic Tech.*, *25*, 452–463, 2008.

Hurther, D., and P. D. Thorne, Suspension and nearbed load sediment transport processes above a migrating sand rippled bed under shoaling waves, *J. Geophys. Res.*, *116*, 2011.

Hurther, D., P. D. Thorne, M. B. U. Lemmin, and J.-M. Barnoud, A multi-frequency acoustic concentration and velocity profiler (ACVP) for boundary layer measurements of fine-scale flow and sediment transport processes, *Coast. Eng.*, *58*, 594–605, 2011.

IOC, SCOR, and IAPSO, *The international thermodynamic equation of seawater - 2010: Calculation and use of thermodynamic properties*, Intergovernmental Oceanographic Commission, Manuals and Guides No. 56, UNESCO (English), 2010.

Isakson, M. J., N. P. Chotiros, R. Abraham Yarbrough, and J. N. Piper, Quantifying the effects of roughness scattering on reflection loss measurements, *J. Acoust. Soc. Am.*, *132*, 3687–3697, 2012.

Jackson, D., and M. Richardson, *High-Frequency Seafloor Acoustics*, Springer Science & Business Media, New York, NY, 2007.

Jaeger, H. M., S. R. Nagel, and R. P. Behringer, The physics of granular materials, *Phys. Today*, *49*, 32–39, 1996.

Jain, N., J. M. Ottino, and R. M. Lueptow, Effect of interstitial fluid on a granular flowing layer, *J. Fluid Mech.*, *508*, 23–44, 2004.

Jeong, Y. H., S. R. Nagel, and S. Bhattacharya, Ultrasonic investigation of the glass transition in glycerol, *Phys. Rev. A*, *34*, 602, 1986.

Kimura, M., Velocity dispersion and attenuation in granular marine sediments: Comparison of measurements with predictions using acoustic models, *J. Acoust. Soc. Am.*, *129*, 3544–3561, 2011.

Kimura, M., Erratum: Velocity dispersion and attenuation in granular marine sediments: Comparison of measurements with predictions using acoustic models [J. Acoust. Soc. Am. 129, 3544–3561 (2011)], *J. Acoust. Soc. Am.*, *135*, 2126–2127, 2014.

Kreith, F., and D. Y. Goswami, *The CRC handbook of mechanical engineering*, CRC press, 2004.

Kundu, P. K., *Fluid Mechanics*, Academic Press, San Diego, 1990, 638 pp.

Lanckriet, T., J. A. Puleo, and N. Waite, A conductivity concentration profiler for sheet flow sediment transport, *IEEE J. Ocean. Eng*, *38*, 55–70, 2013.

Le Gonidec, Y., and D. Gibert, Multiscale analysis of waves reflected by granular media: Acoustic experiments on glass beads and effective medium theories, *J. Geophys. Res.-Sol. Ea.*, *112*, 1–12, 2007.

Lee, K., V. Humphrey, B.-N. Kim, and S. Yoon, Frequency dependencies of phase velocity and attenuation coefficient in a water-saturated sandy sediment from 0.3 to 1.0 MHz, *J. Acoust. Soc. Am.*, *121*, 2553–2558, 2007.

Lee, K., E. Park, and W. Seong, High frequency measurements of sound speed and attenuation in water-saturated glass-beads of varying size, *J. Acoust. Soc. Am.*, *126*, EL28–EL33, 2009.

Lloyd, P., and M. V. Berry, Wave propagation through an assembly of spheres: IV. relations between different multiple scattering theories, *Proc. Phys. Soc.*, *91*, 678–688, 1967.

Medwin, H., *Sounds in the sea: From ocean acoustics to acoustical oceanography*, Cambridge University Press, 2005.

Mehta, A., G. C. Barker, and J.-M. Luck, Heterogeneities in granular materials, *Phys. Today*, *62*, 40–45, 2009.

MiDi, G. D. R., On dense granular flows, *Eur. Phys. J. E*, *14*, 2004.

Mifsud, J. F., Experimental study of the acoustic properties of water-filled sands, *Univ. of Texas, Defense Res. Lab. Rep.*, *DRL-A-72*, 1953.

Millero, F. J., and A. Poisson, International one-atmosphere equation of state of seawater, *Deep-Sea Res*, *28*, 625–629, 1981.

Montgomery, D. C., and G. C. Runger, *Applied Statistics and Probability for Engineers*, John Wiley & Sons, 2010.

Morgan, P. P., *SEAWATER: A library of MATLAB Computational Routines for the Properties of Sea Water: Version 1.2*, CSIRO Marine Laboratories, 1994.

Moussatov, A., L. Guillon, C. Ayrault, and B. Castagnède, Experimental study of the dispersion of ultrasonic waves sandy sediments, *C. R. Acad. Sci. II B*, *326*, 433–439, 1998.

Naqshband, S., J. Ribberink, D. Hurther, and S. Hulscher, Bed load and suspended load contributions to migrating sand dunes in equilibrium, *J. Geophys. Res.*, *119*, 1043–1063, 2014.

Nielsen, P., *Coastal Bottom Boundary Layers and Sediment Transport*, World Scientific, River Edge, New Jersey, 1992, 324 p.

Nolle, A. W., W. A. Hoyer, J. F. Mifsud, W. R. Runyan, and M. B. Ward, Acoustical properties of water-filled sands, *J. Acoust. Soc. Am.*, *35*, 1394–1408, 1963.

Ogilvy, J. A., *Theory of Wave Scattering from Random Rough Surfaces*, CRC Press, 1991.

Pace, N. G., Z. K. S. Al-Hamdani, and P. D. Thorne, The range dependence of normal incidence acoustic backscatter from a rough surface, *J. Acoust. Soc. Am.*, *77*, 101–112, 1985.

Page, J. H., P. Sheng, H. P. Schriemer, I. Jones, X. Jing, and D. A. Weitz, Group velocity in strongly scattering media, *Science*, *271*, 634–637, 1996.

Park, E., K. Lee, W. Seong, and J. Park, Sound speed and attenuation measurements in saturated glass beads, in *The Nineteenth International Offshore and Polar Engineering Conference*, International Society of Offshore and Polar Engineers, 2009.

Peters, F., and L. Petit, Propagation of ultrasound waves in concentrated suspensions, *Acta Acust united Acust.*, *86*, 838–846, 2000.

Pignatel, F., C. Asselin, L. Krieger, I. C. Christov, J. M. Ottino, and R. M. Lueptow, Parameters and scalings for dry and immersed granular flowing layers in rotating tumblers, *Phys. Rev. E*, *86*, 011304, 2012.

Reed, A. H., K. B. Briggs, and D. L. Lavoie, Porometric properties of siliciclastic marine sand: A comparison of traditional laboratory measurements with image analysis and effective medium modeling, *IEEE J. Ocean. Eng.*, *27*, 581–592, 2002.

Reed, A. H., K. E. Thompson, K. B. Briggs, and C. S. Willson, Physical pore properties and grain interactions of SAX04 sands, *IEEE J. Ocean. Eng.*, *35*, 488–501, 2010.

Revil-Baudard, T., J. Chauchat, D. Hurther, and P.-A. Barraud, Investigation of sheet-flow processes based on novel acoustic high-resolution velocity and concentration measurements, *J. Fluid Mech.*, *767*, 1–30, 2015.

Ribberink, J. S., and A. A. Al-Salem, Sheet flow and suspension of sand in oscillatory boundary layers, *Coast. Eng.*, *25*, 205–225, 1995.

Richardson, M. D., K. L. Williams, K. B. Briggs, and E. I. Thorsos, Dynamic measurement of sediment grain compressibility at atmospheric pressure: acoustic applications, *IEEE J. Ocean. Eng.*, *27*, 593–601, 2002.

Rohatgi, A., Webplotdigitizer 4.3, https://automeris.io/WebPlotDigitizer/, 2015, last viewed October 26, 2020.

Rossing, T., *Springer Handbook of Acoustics*, Springer Handbook of Acoustics, Springer New York, 2007.

Schwartz, L., and T. J. Plona, Ultrasonic propagation in close-packed disordered suspensions, *J. Appl. Phys.*, *55*, 3971–3977, 1984.

Sen, P. N., and D. L. Johnson, Topological limitations of effective-medium approximations in fluid-solid systems having two longitudinal-acoustic modes, *Phys. Rev. B*, *27*, 3133–3137, 1983.

Sen, P. N., C. Scala, and M. H. Cohen, A self-similar model for sedimentary rocks with application to the dielectric constant of fused glass beads, *Geophys.*, *46*, 781–795, 1981.

Sessarego, J.-P., and R. Guillermin, High-frequency sound-speed, attenuation, and reflection measurements using water-saturated glass beads of different sizes, *IEEE J. Ocean. Eng.*, *37*, 507–515, 2012.

Sessarego, J.-P., R. Guillermin, and A. N. Ivakin, High-frequency sound reflection by water-saturated sediment interfaces, *IEEE J. Ocean. Eng.*, *33*, 375–385, 2008a.

Sessarego, J.-P., A. N. Ivakin, and D. Ferrand, Frequency dependence of phase speed, group speed, and attenuation in water-saturated sand: Laboratory experiments, *IEEE J. Ocean. Eng.*, *33*, 359–366, 2008b.

Shinbrot, T., and F. J. Muzzio, Nonequilibrium patterns in granular mixing and segregation, *Phys. Today*, *53*, 25–30, 2000.

Spelt, P. D. M., M. A. Norato, A. S. Sangani, M. S. Greenwood, and L. L. Tavlarides, Attenuation of sound in concentrated suspensions: theory and experiments, *J. Fluid Mech.*, *430*, 51–86, 2001.

Stoll, R. D., Comments on "Biot model of sound propagation in water-saturated sand" [J. Acoust. Soc. Am. 97, 199–214 (1995)], *J. Acoust. Soc. Am.*, *103*, 2723–2725, 1998.

Thomas, P. R., Transmission of broadband acoustic signals through saturated granular media, Ph.D. thesis, University of Bath, 1978.

Thomas, P. R., and N. G. Pace, Broadband measurements of acoustic attenuation in water-saturated sands, *Ultrasonics*, *18*, 13–17, 1980.

Thorne, P. D., and N. G. Pace, Acoustic studies of broadband scattering from a model rough surface, *J. Acoust. Soc. Am.*, *75*, 133–144, 1984.

Thorne, P. D., N. G. Pace, and Z. K. S. Al-Hamdani, Laboratory measurements of backscattering from marine sediments, *J. Acoust. Soc. Am.*, *84*, 303–309, 1988.

Thorne, P. D., D. Hurther, and B. D. Moate, Acoustic inversions for measuring boundary layer suspended sediment processes, *J. Acoust. Soc. Am.*, *130*, 1188–1200, 2011.

Thorsos, E. I., The validity of the Kirchhoff approximation for rough surface scattering using a gaussian roughness spectrum, *J. Acoust. Soc. Am.*, *83*, 78–92, 1988.

Trahey, G. E., S. W. Smith, and O. T. Von Ramm, Speckle pattern correlation with lateral aperture translation: Experimental results and implications for spatial compounding, *IEEE Trans. Ultrason. Ferroelectr. Freq. Control*, *33*, 257–264, 1986.

Turner, J. S., *Buoyancy Effects in Fluids*, Cambridge university press, 1979.

Urick, R. J., The absorption of sound in suspensions of irregular particles, *J. Acoust. Soc. Am.*, *20*, 283–289, 1948.

van Rijn, L. C., J. S. Ribberink, J. V. D. Werf, and D. J. R. Walstra, Coastal sediment dynamics: recent advances and future research needs, *J. Hydr. Res*, *51*, 475–493, 2013.

Venegas, G. R., and P. S. Wilson, An illustration of the effect of neglecting poroelastic physics of water-saturated glass beads in a laboratory phase speed inference process, *J. Acoust. Soc. Am.*, *146*, 1326–1334, 2019.

Waterman, P. C., and R. Truell, Multiple scattering of waves, *J. Math. Phys.*, *2*, 512–537, 1961.

Weissberg, H. L., Effective diffusion coefficient in porous media, *J. Appl. Phys.*, *34*, 2636–2639, 1963.

White, T. E., Status of measurement techniques for coastal sediment transport, *Coast. Eng.*, *35*, 17–45, 1998.

Williams, K. L., An effective density fluid model for acoustic propagation in sediments derived from Biot theory, *J. Acoust. Soc. Am.*, *110*, 2276–2281, 2001.

Williams, K. L., D. R. Jackson, E. I. Thorsos, D. Tang, and S. G. Schock, Comparison of sound speed and attenuation measured in a sandy sediment to predictions based on the Biot theory of porous media, *IEEE J. Ocean. Eng.*, *27*, 413–428, 2002.

Wilson, G. W., and A. E. Hay, Acoustic backscatter inversion for suspended sediment concentration and size: a new approach using statistical inverse theory, *Cont. Shelf Res.*, *106*, 130–139, 2015.

Wilson, G. W., and A. E. Hay, Acoustic observations of near-bed sediment concentration and flux statistics above migrating sand dunes, *Geophys. Res. Lett.*, *43*, 6304–6312, 2016.

Wilson, G. W., and A. E. Hay, Short-pulse method for acoustic backscatter amplitude calibration at MHz frequencies, *J. Acoust. Soc. Am.*, *142*, 1655–1662, 2017.

Wood, A. B., *A Textbook of Sound*, The MacMillan Company, New York, 1930.

Yang, H., and W. Seong, High frequency compressional wave speed and attenuation measurements in water-saturated granular media with unimodal and bimodal grain size distributions, *J. Acoust. Soc. Am.*, *143*, 659–665, 2018.

Yang, H., W. Seong, and K. Lee, Model-data comparison of high frequency compressional wave attenuation in water-saturated granular medium with bimodal grain size distribution, *Ultrasonics*, *82*, 161–170, 2018.

Zemanek, J., Beam behavior within the nearfield of a vibrating piston, *J. Acoust. Soc. Am.*, *49*, 181–191, 1971.